Imperial College London

Strong Light-Matter Coupling in Plasmonic Nanocavities

Nuttawut Kongsuwan

Condensed Matter Theory Group

Department of Physics

Imperial College London

Thesis submitted for the degree of

Doctor of Philosophy of Imperial College London

DECLARATION OF ORIGINALITY

I hereby declare that all material presented in this thesis is my own work, except where otherwise noted.

— Nuttawut Kongsuwan

COPYRIGHT DECLARATION

The copyright of this thesis rests with the author. Unless otherwise indicated, its contents are licensed under a Creative Commons Attribution-Non Commercial 4.0 International Licence (CC BY-NC). Under this licence, you may copy and redistribute the material in any medium or format. You may also create and distribute modified versions of the work. This is on the condition that: you credit the author and do not use it, or any derivative works, for a commercial purpose. When reusing or sharing this work, ensure you make the licence terms clear to others by naming the licence and linking to the licence text. Where a work has been adapted, you should indicate that the work has been changed and describe those changes. Please seek permission from the copyright holder for uses of this work that are not included in this licence or permitted under UK Copyright Law.

ABSTRACT

Optical properties of a quantum emitter are drastically modified inside a nanometer-sized gap between two plasmonic nanostructures. At such a nanoscale gap, plasmonic resonances confine light far beyond the diffraction limit and form a nanoscopic optical cavity, called a plasmonic nanocavity. This thesis investigates the optical properties of plasmonic nanocavities and highlights their ability to facilitate strong light-matter interaction.

We first study plasmonic nanocavities by treating their resonances as leaky modes with complex eigenfrequencies. By varying their gap morphology, several bright and dark gap plasmonic resonances are discovered, which are essential for understanding how a nanocavity optically influences a quantum emitter. Near-field and far-field investigations also reveal intricate multiple-mode interaction with a quantum emitter.

Next, this thesis tackles the misconception that fluorescence emission from a quantum emitter is always quenched through non-radiative decay channels when the emitter is placed closer than 10 nm to a plasmonic nanostructure. We demonstrate the suppression of fluorescence quenching in plasmonic nanocavities due to plasmon hybridization, which enhances the excitation and radiation from the emitter. This enhancement is shown to be strong enough to facilitate single-molecule strong coupling, as evident in its dynamic Rabi oscillations.

Finally, an innovative sensing scheme is proposed, which combines immunoassay sensing with strong coupling in plasmonic nanocavities. By chemically linking the antibody-antigen-antibody complex with a quantum emitter label, we show that the proposed scheme provides 1500% sensitivity enhancement compared to plasmonic sensors with conventional labels. This scheme could lead to the development of plasmonic bio-sensing for single molecules and new pathways towards room-temperature quantum sensing.

ACKNOWLEDGEMENTS

I would like to thank the following people who have influenced me for the entirety of my Ph.D. Firstly and most importantly, I would like to thank my supervisor Prof. Ortwin Hess for giving me the opportunity to study in his group at Imperial College London. Second, I would like to express my sincere gratitude to my mentor Dr. Angela Demetriadou for her continuous support. These two individuals have help me grow into a mature scientist and taught me essential skills to work in the academic world.

My work would never have reached its full potential without the help of my collaborators. I would like to thank everyone I worked with at Imperial College London: Alaxandra Crai, Peter Fox, Dr. Matthias Saba, Dr. Adam Freddie Page, Dr. Andreas Pusch, Dr. Tommaso Tufarelli, Dr. Frank Bello and Dr. Xiaona Liu; Aalto University: Päivi Törmä and Aaro Väkeväinen; Agency for Science, Technology and Research: Xiao Xiong, Ping Bai, Jia-Bin You, Ching Eng Png and Lin Wu; and University of Cambridge: Matthew Horton, Marlous Kamp, Bart de Nijs, Rohit Chikkaraddy, Felix Benz, Vladimir A. Turek, Ulrich F. Keyser, Jeremy J. Baumberg.

I would like to also thank all my friends, not mentioned above, at Condensed Matter Theory group: Dr. Stefano Guazzotti, Dr. Peter Davies, Emanuele Galiffi, Syed Hussain, Simon Lieu, Yiming Lai, Simon Pocock, Lara Roman-Castellanos, Iacopo Rovelli, Ilya Tarasenko, Marise Westbroek and Fan Yang; Theory and simulation of materials CDT: Dr. Andrew Horsfield and everyone from cohort 7; and all my friends from Imperial College Speakers club.

I would like to give special thanks to the love of my life Sirion Suchaovanich for being with me from the beginning to the end of my Ph.D. Last but not least, I would like to acknowledge with gratitude the support and love of my family: Soravit, Jessada and Varisara Kongsuwan.

CONTENTS

LIST OF FIGURES

LIST OF TABLES

LIST OF ACRONYMS

AuNP	gold nanoparticle
BDP	bonding dipole plasmon
BQP	bonding quadrupole plasmon
cQED	cavity quantum electrodynamics
FDTD	finite-difference time-domain
FEM	finite-element method
LDOS	local density of states
LSP	localized surface plasmon
MB	Maxwell-Bloch
MIM	metal-insulator-metal
NFFT	near-to-far field transformation
NPoM	nanoparticle on mirror
PL	photoluminescence
PMLs	perfectly matched layers
SERS	surface-enhanced Raman scattering
SPs	surface plasmons
SPP	surface plasmon polariton
TFSF	total-field scattered-field
QNM	quasinormal mode

LIST OF SYMBOLS

A	Amplitude
a	Lattice constant
$\hat{a}$	Photon lowering operator
$\mathbf{B}$	Magnetic flux density
$B_{i,j}$	QNM dipole coupling operator
C	Constant variable
$\mathbf{D}$	Electric displacement field
D	Debye unit
d	Gap thickness
$\mathbf{E}$	Electric field
$\mathbf{E}^{\text{div}}$	Divergent electric field
$\mathbf{E}^{\text{ff}}$	Far-field electric field
$\mathbf{E}_0$	Incident electric field
$\mathbf{E}_{\text{em}}$	Emitter's electric field
$\mathbf{E}_s$	Scattered electric field
$\widetilde{\mathbf{E}}_i$	QNM electric field
E_z^{cav}	Cavity E_z field (no emitter)
E_z^{em}	Cavity E_z field with an emitter
$E_{\text{em}}^{\text{ind}}$	Induced E_z field by an emitter
$\hat{\mathbf{e}}_i$	Unit vector
F	Purcell factor
F_i	QNM Purcell factor
F_{tot}	Total Purcell factor
f	Driving force
$\mathbf{G}$	Dyadic Green's function
g	Coupling strength
$\mathbf{H}$	Magnetic field
$\mathbf{H}^{\text{ff}}$	Far-field magnetic field
$\widetilde{\mathbf{H}}_i$	QNM magnetic field
$\widehat{H}$	Hamiltonian
$\widehat{\mathcal{H}}$	QNM auxiliary-field operator
$\mathcal{I}$	Identity superoperator
$\mathbf{J}$	Internal current density
$\mathbf{J}_{\text{em}}$	Emitter's current density
$\mathbf{J}_{\text{ext}}$	External current density
$\mathbf{J}_{\text{tot}}$	Total current density
$\widetilde{\mathbf{J}}_{i,k}$	QNM auxiliary current
k	Spring constant
$\mathcal{L}$	Lindblad superoperator
m	Mass
$\mathbf{m}$	Magnetic dipole moment
$\mathbf{M}$	Magnetization field
N	Analyte number
N_d	Electron density
n_B	Background refractive index
$\mathbf{p}$	Electric dipole moment
$\mathbf{P}$	Polarization field
$\widetilde{\mathbf{P}}_{i,k}$	QNM auxiliary polarization
P_0	Vacuum power dissipation
P_{tot}	Total power dissipation

Q	Quality factor
R	Radius
$\mathbf{r}$	Position vector
r	Polar radial coordinate
$\mathbf{r}_{em}$	Emitter's position vector
S	Poynting flux
S_i	QNM Poynting flux
S_N^{shift}	Shifting-type sensitivity
S_N^{split}	Splitting-type sensitivity
t	Time
$\hat{U}$	Unitary operator
V_E	Electric potential
V	Volume
V_{eff}	Effective mode volume
V_i	QNM mode volume
w	Facet width
x	Cartesian x-coordinate
Δx	Mesh size
y	Cartesian y-coordinate
Y_ℓ^m	Spherical harmonics
z	Cartesian z-coordinate
α_i	QNM coupling coefficient
Γ	Dephasing rate
Γ_S	Sensitivity enhancement
γ	Relaxation decay rate
γ_0	Vacuum decay rate
γ_{em}	Fluorescence rate
γ_{em}^0	Vacuum fluorescence rate
$\widetilde{\gamma}_{em}$	Normalized fluorescence rate
γ_{exc}	Excitation rate
γ_{exc}^0	Vacuum excitation rate
$\widetilde{\gamma}_{exc}$	Normalized excitation rate
γ_{int}	Internal decay rate
γ_{nr}	Non-radiative decay rate
$\widetilde{\gamma}_{nr}$	Normalized non-radiative decay rate
γ_p	Pure dephasing rate
γ_{rad}	Radiative decay rate
$\widetilde{\gamma}_{rad}$	Normalized radiative decay rate
γ_{tot}	Total decay rate
$\widetilde{\gamma}_{tot}$	Normalized total decay rate
Δ_d	Detuning
ε	Permittivity
ε_0	Vacuum permittivity
ε_B	Background permittivity
ε_∞	Permittivity at infinite frequency
η	Quantum yield
η^0	Vacuum quantum yield
κ	Cavity loss rate
κ_i	QNM imaginary frequency
Λ	Incoherent pumping rate
λ	Wavelength
λ_{em}	Emitter's transition wavelength
λ_{pm}	Pseudo-mode wavelength
$\boldsymbol{\mu}$	Emitter's dipole moment vector
μ	Emitter's dipole moment
μ_0	Vacuum permeability
ρ	Internal Charge density
ρ_d	Optical local density of states
$\hat{\varrho}$	Density matrix
$\hat{\varrho}_0$	Steady state density matrix

ρ_d	Optical local density of states
ϱ_{ij}	Density matrix element
ρ_{ext}	External charge density
ρ_{ext}	Total charge density
Σ	System domain boundary
$\hat{\sigma}$	Spin 1/2 lowering operator
σ_{ext}	Extinction cross-section
σ^0_{ext}	Extinction cross-section (no emitter)
σ_{PL}	Photoluminescence spectrum
σ_{scat}	Scattering cross-section
ϕ	Polar angular coordinate
ψ	Wavefunction
$\widetilde{\psi}_i$	QNM Auxiliary-field eigenvector
Ω	System domain
ω	Angular frequency
ω_0	Resonant frequency
ω_a	Photon frequency
ω_{em}	Emitter's frequency
ω^L_{em}	Emitter's Lamb shifted frequency
ω_i	QNM real frequency
$\widetilde{\omega}_i$	QNM complex frequency
ω_p	Plasma frequency
ω_+	Upper polariton frequency
ω_-	Lower polariton frequency
$\delta\omega$	Frequency shift
$\Delta\omega$	Frequency splitting

PUBLICATIONS

This thesis contains work drawn from the following publications:

- **N. Kongsuwan**, A. Demetriadou, R. Chikkaraddy, F. Benz, V. A. Turek, U. F. Keyser, J. J. Baumberg and O. Hess, "Suppressed quenching and strong-coupling of Purcell-enhanced single-molecule emission in plasmonic nanocavities", *ACS Photonics*, 5, 186–191 (2018) — Adapted with permission. Copyright (2017) American Chemical Society.

- **N. Kongsuwan**, A. Demetriadou, R. Chikkaraddy, J. J. Baumberg and O. Hess, "Fluorescence enhancement and strong-coupling in faceted plasmonic nanocavities", *EPJ Appl. Metamat.* 5, 6 (2018) — Adapted with permission. Copyright (2018) EDP Sciences.

- **N. Kongsuwan**, X. Xiong, P. Bai, J. B. You, C. E. Png, L. Wu and O. Hess, "Quantum Plasmonic Immunoassay Sensing", *Nano Lett.*, 19, 9, 5853-5861 (2019) — Adapted with permission. Copyright (2019) American Chemical Society.

- **N. Kongsuwan**, A. Demetriadou, M. Horton, R. Chikkaraddy, J. J. Baumberg and O. Hess, "Quasinormal-Mode Analyses of Nanoparticle-on-Mirror Plasmonics", *ArXiv preprint arXiv:1910.02273* (2019).

Other published works during my Ph.D. at Imperial College include:

- R. Chikkaraddy, V. A. Turek, **N. Kongsuwan**, F. Benz, C. Carnegie, T. van de Goor, B. de Nijs, A. Demetriadou, O. Hess, U. F. Keyser, and J. J. Baumberg, "Mapping Nanoscale Hotspots with Single-Molecule Emitters Assembled into Plasmonic Nanocavities Using DNA Origami", *Nano Lett.*, 18, 405-411 (2018).

- X. Liu, **N. Kongsuwan**, X. Li, D. Zhao, Z.-M. Wu, O. Hess and X.-H. Zhang, "Tailoring the Third-Order Nonlinear Optical Property of a Hybrid Semiconductor

Quantum Dot-Metal Nanoparticle: From Saturable to Fano-Enhanced Absorption", Manuscript submitted to *J. Phys. Chem. Lett.*

- M. J Horton, O. S. Ojambati, R. Chikkaraddy, W. M. Deacon, **N. Kongsuwan**, A. Demetriadou, O. Hess and J. J. Baumberg, "Nanoscopy through a plasmonic nanolens", Manuscript submitted to *Proc. Natl. Acad. Sci. U.S.A.*

- M. Kamp, B. de Nijs, **N. Kongsuwan**, M. Saba, R. Chikkaraddy, O. Hess, O. A. Scherman and J. J. Baumberg, "Cascaded Nano-Optics to Probe Microsecond Molecular Dynamics", Manuscript submitted to *Sci. Adv.*

The works in this thesis were orally presented in the following international conferences:

- **N. Kongsuwan**, A. Demetriadou, R. Chikkaraddy, F. Benz, V. A. Turek, U. F. Keyser, J. J. Baumberg and O. Hess, "Suppression of fluorescence quenching and strong-coupling in plasmonic nanocavities", *11th International Congress on Engineered Material Platforms for Novel Wave Phenomena - Metamaterials 2017*, Marseille, France.

- **N. Kongsuwan**, A. Demetriadou, R. Chikkaraddy, F. Benz, V. A. Turek, U. F. Keyser, J. J. Baumberg and O. Hess, "Suppression of fluorescence quenching in plasmonic nanocavities", *Nanophotonics and Micro/Nano Optics International Conference (NANOP) 2017*, Barcelona, Spain.

- **N. Kongsuwan**, X. Xiong, P. Bai, J. B. You, C. E. Png, L. Wu and O. Hess, "Plasmonic Quantum Immunoassay Sensing", *10th International Conference on Materials for Advanced Technologies (ICMAT) 2019*, Singapore.

1 INTRODUCTION

Emission properties of a quantum emitter, i.e. a single-photon light source, can be modified by placing the emitter in a structured optical environment, such as in front of a dielectric mirror [1, 2]. When the interaction is sufficiently strong, the emitter becomes intricately linked with its optical environment, forming hybrid states which differ from those of the emitter or the optical system individually. This is known as *strong-coupling*. In the optical regime, light-matter strong-coupling was realized first with many atoms in 1989 [3] and later with a single atom in 1992 using a high-finesse optical cavity [4]. However, these experiments were possible only at cryogenic temperature. Light-matter strong-coupling at room temperature had not been achieved until the recent development of plasmonic nanocavities [5].

Plasmonics is the study of surface plasmons (SPs), coherent delocalized oscillations of conduction electrons on a metal surface. Since its prediction in 1957 [6] and first observation in 1960 [7], plasmonics has become a rapidly evolving field of study with various applications including solar cells [8, 9], spectroscopy [10] and cancer treatment [11, 12]. SPs can be excited by electromagnetic fields and have the ability to confine the fields far beyond their diffraction limit. Such extreme field confinement enhances light-matter interaction and gives rise to phenomena such as surface-enhanced Raman scattering (SERS) and surface-enhanced fluorescence [13]. Through recent advances in nanofabrication, nanoscale control over the size and shape of metal structures has been achieved [14, 15]. SPs excited on these metal nanostructures form optical nanocavities with unprecedented light enhancement [16, 17]. The plasmonic nanocavities indeed provide an ideal platform for realizing light-matter strong-coupling at room temperature [18–21].

Optical fields can be further confined and enhanced at a nanoscale spacing between two metal nanostructures where SPs from each nanostructure hybridize [22, 23] and

form an intense electromagnetic hot spot. Such unparalleled light confinement has been shown to facilitate even single-emitter strong-coupling at room temperature, first demonstrated by Chikkaraddy et. al. [24] using a single dye molecule placed inside a nanoparticle on mirror (NPoM) construct. Similar demonstrations have also been made using single semiconductor quantum dots placed inside a bow tie nanostructure [25] and a slot nanoresonator probe [26].

Indeed, the field of nanoplasmonic strong-coupling is rapidly evolving from emitter-ensemble toward single-emitter strong-coupling. This thesis provides a comprehensive theoretical and numerical studies on plasmonic nanocavities and their coupling to single quantum emitters. Several approaches, including classical, semi-classical and quantum mechanical methods, are used to shed light on the complex interaction between light and matter at the nanoscale.

The following sections give the overviews of plasmonic nanocavities and their ability to accommodate strong light-matter coupling. Section 1.1 first discusses plasmonics in metal nanoparticles and how it leads to nanoscale optical cavities. Section 1.2 introduces light-matter interaction in an optical cavity and examines the weak- and strong-coupling regimes. Finally, this chapter reviews important numerical methods in the field of plasmonic light-matter coupling in Section 1.3, followed by the thesis content summary in Section 1.4.

1.1 PLASMONIC NANOCAVITIES

1.1.1 Localized Surface Plasmons

There are in general two types of SPs: localized charge oscillation on a closed surface of a small metal particle called a localized surface plasmon (LSP) and a propagating charge oscillation on a planar metal surface called a surface plasmon polariton (SPP). This thesis mainly focuses on LSPs and does not discuss SPPs any further.

To demonstrate the LSP, this section considers a gold nanoparticle (AuNP) with radius R in background permittivity ε_B illuminated by electric field $\mathbf{E} = \mathbf{E}_0 e^{-i\omega t}$. If the AuNP

is much smaller than the wavelength of the incident field, the quasi-static approximation can be assumed where the AuNP experiences the same phase and amplitude over its entire volume. In this approximation, every part of the AuNP responds instantaneously to the change in the incident field. Consequently, its electric and magnetic responses of the AuNP can be separated, and the electric potential V_E satisfies the Laplace equation [13, 27]

$$\nabla^2 V_E = 0. \tag{1.1}$$

For simplicity, azimuthal symmetry is assumed where $\partial V_E/\partial\phi = 0$ in the spherical coordinates (r, θ, ϕ). The general solution to the Laplace equation is then given by

$$V_E(r,\theta) = (C_1 r^{\ell} + C_2 r^{-(\ell+1)})\mathcal{P}_{\ell}(\cos\theta) \tag{1.2}$$

where $\mathcal{P}_{\ell}$ is the Legendre polynomial whereas C_1 and C_2 are constants. By applying the boundary conditions that V_E is continuous over the optical discontinuity at the AuNP surface ($r = R$) and is finite at $r = 0$ and $r \to \infty$, the solution for the ℓ-th mode is given by [28]

$$V_E^{\ell}(r,\theta) = \begin{cases} C\left(\frac{r}{R}\right)^{\ell}\mathcal{P}_{\ell}(\cos\theta), & r < R \\ C\left(\frac{R}{r}\right)^{\ell+1}\mathcal{P}_{\ell}(\cos\theta), & r \geqslant R \end{cases} \tag{1.3}$$

where C is a normalization constant. Note that spherical symmetry also allows additional solutions to the Laplace equation with ϕ-dependence given by associated Legendre polynomials $\mathcal{P}_{\ell}^{m}(\cos\theta)$ with $-\ell \leqslant m \leqslant \ell$. The azimuthal symmetric solution in Eq (1.3) corresponds to the $m = 0$ solution, disregarding its $2\ell + 1$ degeneracy.

By imposing the continuity condition for the normal component of the electric displacement field $\hat{\mathbf{e}}_r \cdot \mathbf{D} = -\varepsilon\partial V_E^{\ell}/\partial r$ at $r = R$, the resonance condition is obtained for the ℓ-th mode

$$\ell \mathrm{Re}[\varepsilon_{Au}(\omega_{\ell})] + (\ell + 1)\varepsilon_B = 0 \tag{1.4}$$

where ω_{ℓ} is the resonant frequency of the ℓ-th mode. Figure 1.1 shows the LSP resonant frequencies of a AuNP, and the inset shows the schematics for the $\ell = 1, 2, 3$ LSP charge distributions. For $\ell = 1$, we obtain $\mathrm{Re}[\varepsilon_{Au}(\omega_1)] = -2\varepsilon_b$ which is known as the Fröhlich condition for the dipole LSP resonance. At large mode index ℓ, the resonant frequencies

approach ω_∞, where $\mathrm{Re}[\varepsilon_{\mathrm{Au}}(\omega_\infty)] = -\varepsilon_{\mathrm{B}}$. These higher-order modes at ω_∞ respond collectively to an incident field and are often referred to as a pseudo-mode [29].

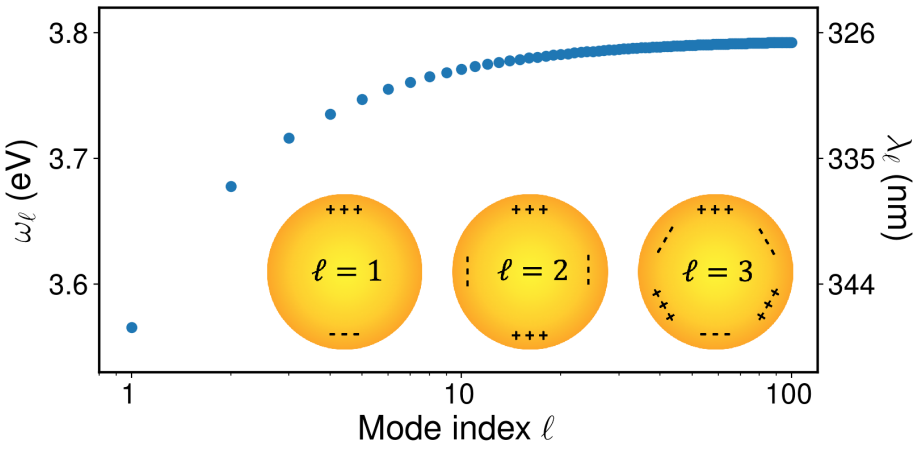

Figure 1.1: Frequency ω_ℓ and wavelength λ_ℓ of the LSPs with mode indices ℓ. Inset shows the surface charge distributions for the LSPs with $\ell = 1$, 2 and 3.

For nanoparticles smaller than 100 nm, the quasi-static approximation is generally adequate for even imperfect spherical shapes. For larger nanoparticles, however, retardation becomes significant, and a more accurate description, beyond the quasi-static approximation, is required. Analytic treatments of simple nanoparticles are available, for example, a spherical nanoparticle given by the Mie theory [30]. For arbitrarily shaped nanoparticles, we resort to full-wave numerical techniques such as finite-element or finite-difference methods.

1.1.2 Gap Plasmonic Nanocavities

When two metal nanoresonators are brought close together, forming a gap of just a few nanometers, the LSPs of each nanoresonator hybridize and provide unprecedented light confinement. For instance, a gap size as small as 0.2 nm in a plasmonic dimer, shown in Fig. 1.2(a), was achieved [31], massively enhancing SERS signals [32] and revealing quantum phenomena such as electron tunneling [33]. Gap plasmonic nanocavities have also been investigated using various geometries, including a bowtie nanoantenna [25, 34], slot nanoresonator probe [26], hemisphere dimer [35] and NPoM [36, 37].

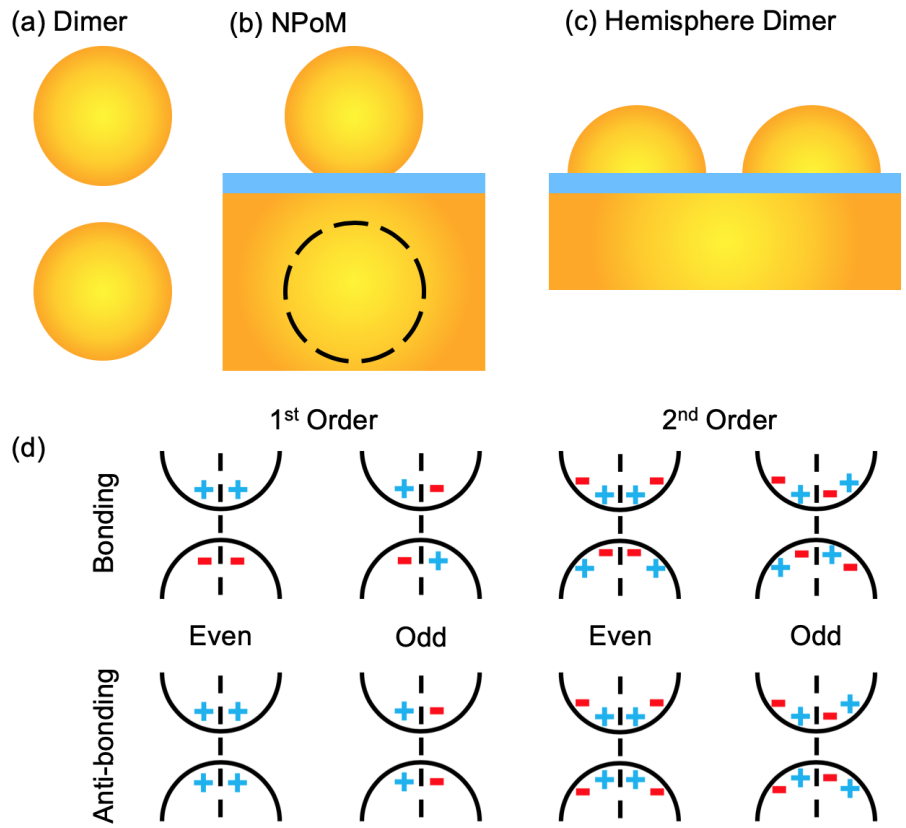

Figure 1.2: (a-c) Schematics of some gap plasmonic nanocavities: (a) a dimer, (b) an NPoM and (c) a hemisphere dimer structures. (d) Schematics of first and second-order gap resonances of a plasmonic nanocavity. Each resonance order has four types: bonding/antibonding and symmetric/antisymmetric (even/odd) resonances.

A notable example is the NPoM structure where a metal nanoparticle is separated from an underlying metal film by single molecular layers, such as graphene [38], Cucurbituril [24] and DNA-origami [39], see Fig. 1.2(b). This nanostructure offers reliable and repeatable nanoscale gap size, determined by its molecular spacer, and leads to the first demonstration of single-emitter strong-coupling at room temperature [24]. Hence, the NPoM nanocavity is the main nanostructure of choice discussed in Chapters 2 and 3. Another nanostructure that this thesis investigates is a hemisphere dimer, shown in 1.2(c). Although fabricating this nanostructure with a nanometer-size gap could present a huge technological challenge, the hemisphere dimer offers the possibility of a sensor-on-chip application of single-emitter strong-coupling which is the main focus in Chapter 4.

Although different plasmonic nanocavities differ on physical geometries, they possess qualitatively the same gap plasmonic resonances. The first and second-order gap

resonances are illustrated in Figure 1.2(d) where each order consists of four types: bonding/antibonding and even/odd (symmetric/antisymmetric) resonances. The bonding resonances have opposite charges on either side of the gap, which confine and enhance electromagnetic fields. On the other hand, the antibonding resonances have the same charges on either side of the gap, which suppress electromagnetic fields in the gap and cannot be excited from the far-field. Hence, the antibonding resonances are irrelevant to the discussion in this thesis.

Due to opposite charges on either side of the gap, the enhanced electric fields of the bonding resonances dominantly align perpendicularly to the substrate. In most experiments, the even bonding resonances are bright modes and can be efficiently excited by light incident at an oblique angle [24, 39]. Hence, the first and second-order even bonding modes are given special names of the bonding dipole plasmon (BDP) and bonding quadrupole plasmon (BQP), respectively [31]. On the other hand, the odd bonding resonances are often considered dark modes as they couple much weaker to an external field. However, the odd modes are not completely dark and can be excited in isolation, for example, by a plane wave polarized parallel to the substrate or by two out-of-phase plane waves polarized perpendicular to the substrate [40].

1.1.3 Plasmonic Nanocavities as Leaky Optical Cavities

A resonant mode of a plasmonic nanocavity can be considered as a leaky optical cavity mode and is determined by three parameters: its resonance frequency ω_a, quality factor Q and effective mode volume V_{eff}. The quality factor determines the ability of a cavity mode to retain its energy and is defined as $Q = \omega_a/2\kappa$ where κ is the dissipation rate (half-width-at-half-maximum linewidth). On the other hand, the effective mode volume V_{eff} quantifies the electromagnetic field confinement in a cavity mode. For a perfect optical cavity with $Q \to \infty$, the effective mode volume is defined by the cavity electric field $\mathbf{E}(r)$ as follows

$$V_{eff} = \frac{\int \varepsilon(\mathbf{r})|\mathbf{E}(\mathbf{r})|^2 d^3\mathbf{r}}{\max[\varepsilon(\mathbf{r})|\mathbf{E}(\mathbf{r})|^2]} \tag{1.5}$$

where $\varepsilon(\mathbf{r})$ is the cavity dielectric constant. This expression is invalid for a leaky cavity but provides good approximations to the mode volumes of high-finesse (high-Q) cavities such as Bragg mirrors and whispering-gallery microcavities. For low-Q cavities such as plasmonic nanocavities, however, the generalized form of the mode volume is required [41]. This is discussed in Chapter 2.

1.2 LIGHT–MATTER INTERACTION IN PLASMONIC NANOCAVITIES

1.2.1 Cavity Quantum Electrodynamics

When a single quantum emitter, such as a semiconductor quantum dot or a dye molecule, is placed in close proximity to a plasmonic nanostructure, the emitter can coherently exchange energy with plasmonic resonances. This interaction can be treated within the cavity quantum electrodynamics (cQED) framework where the plasmonic resonances, approximated as cavity modes, are described by bosonic operators $\hat{a}_i$ and frequency ω_i. Similarly, the optical transition of the emitter with transition frequency ω_{em} and dipole moment μ is treated as a two-level system with a Pauli-1/2 operator $\hat{\sigma}$. Assuming that there is only one dominant plasmonic mode, their interaction is described by Jaynes-Cummings Hamiltonian [42]

$$\widehat{H} = \hbar\omega_{em}\hat{\sigma}^{\dagger}\hat{\sigma} + \hbar\omega_a\hat{a}^{\dagger}\hat{a} + \hbar g(\hat{a}\hat{\sigma}^{\dagger} + \hat{a}^{\dagger}\hat{\sigma}) \tag{1.6}$$

where the coupling strength g is determined by the cavity mode's optical properties

$$\hbar g = \mu\sqrt{\frac{\hbar\omega_a}{2\varepsilon_0\varepsilon_B V_{eff}}} \tag{1.7}$$

with the background permittivity ε_B. The coupling regime of the coupled system can then be determined by the difference between the coupling strength g and dissipation rate κ.

When $g < \kappa$, the total energy in the system dissipates to the environment faster than coherent energy interchange between the cavity mode and the emitter, and the system is in the *weak coupling* regime. On the other hand, When the interaction becomes sufficiently strong that the energy exchange rate exceeds the dissipation rate, i.e. $g > \kappa$, the system reaches the *strong-coupling* regime and forms hybrid states which are different from those of its individual components. In this regime, the energy separation between the hybrid states can be observed as splittings in the optical spectra of the system, known as the characteristic Rabi splittings. This also appears in the time domain as a field oscillation, called the Rabi oscillation.

If the energy exchange rate is so rapid that it becomes comparable or exceeds the resonance frequencies of the emitter and the optical field, $g \approx \omega_a, \omega_{em} \gg \kappa$, the system reaches the *ultrastrong-coupling*. In this regime, perturbation theory breaks down, and a complete re-evaluation of the theoretical framework is required [43]. Ultrastrong-coupling is beyond the scope of this thesis, and it will not be discussed further.

1.2.2 Light-Matter Interaction in Weak Coupling Regime

When a quantum emitter coupled weakly to its optical environment, the emitter can be treated as a classical point-like dipole source with frequency ω_{em} at position $\mathbf{r}_{em}$

$$\begin{aligned}\mathbf{J}_{em}(\mathbf{r}, t) &= \frac{d\boldsymbol{\mu}}{dt}\delta(\mathbf{r} - \mathbf{r}_{em}) \\ &= -i\omega_{em}\boldsymbol{\mu}\delta(\mathbf{r} - \mathbf{r}_{em}).\end{aligned} \tag{1.8}$$

In a homogeneous environment with refractive index $n_B = \sqrt{\varepsilon_B}$, the radiation power generated by the dipole and its corresponding decay rate are given by [44]

$$P_0(\omega_{em}) = \frac{n_B \omega_{em}^4 |\boldsymbol{\mu}|^2}{12\pi\varepsilon_0 c^3} \tag{1.9}$$

$$\gamma_0(\omega_{em}) = \frac{n_B \omega_{em}^3 |\boldsymbol{\mu}|^2}{3\pi\varepsilon_0 \hbar c^3}. \tag{1.10}$$

In an optical environment, such as in proximity to plasmonic nanoparticles or cavity resonators, the emission from the emitter could reflect from the surrounding structures and

re-excite itself, weakly perturbing its own optical properties. The re-excitation affects the emitter by changing both its emission rate and emission frequency.

Purcell Effect

The re-excitation from the optical inhomogeneity accelerates, or in some cases decelerates, the emitter's emission rate. This enhancement in the emission rate is called the Purcell effect [1]. To study this effect, we consider the total power dissipated and the total decay rate of the dipole that is excited by the total field $\mathbf{E}$

$$\begin{aligned} P_{tot}(\mathbf{r}_{em};\omega_{em}) &= -\frac{1}{2}\int_{\Omega} \mathrm{Re}\left[\mathbf{J}^*_{em}\cdot\mathbf{E}(\mathbf{r}_{em})\right] d^3\mathbf{r} \\ &= \frac{\omega_{em}}{2}\mathrm{Im}\left[\boldsymbol{\mu}^*\cdot\mathbf{E}(\mathbf{r}_{em})\right] \end{aligned} \tag{1.11}$$

$$\gamma_{tot}(\mathbf{r}_{em};\omega_{em}) = \frac{2}{\hbar}\mathrm{Im}\left[\boldsymbol{\mu}^*\cdot\mathbf{E}(\mathbf{r}_{em})\right]. \tag{1.12}$$

The total field $\mathbf{E}$ is the superposition of the incident field $\mathbf{E}_0$ and the scattered field $\mathbf{E}_s$ from the environment, $\mathbf{E} = \mathbf{E}_0 + \mathbf{E}_s$. The Purcell enhancement factor can then be derived as [44]

$$\begin{aligned} F(\mathbf{r}_{em};\omega_{em}) &= \frac{P_{tot}(\mathbf{r}_{em};\omega_{em})}{P_0(\omega_{em})} = \frac{\gamma_{tot}(\mathbf{r}_{em};\omega_{em})}{\gamma_0(\omega_{em})} \\ &= \frac{6\pi\varepsilon c^3}{n_B\,\omega_{em}^3|\boldsymbol{\mu}|^2}\mathrm{Im}\left[\boldsymbol{\mu}^*\cdot\mathbf{E}(\mathbf{r}_{em})\right] \\ &= 1 + \frac{6\pi\varepsilon c^3}{n_B\,\omega_{em}^3|\boldsymbol{\mu}|^2}\mathrm{Im}\left[\boldsymbol{\mu}^*\cdot\mathbf{E}_s(\mathbf{r}_{em})\right] \end{aligned} \tag{1.13}$$

where the unity emphasizes that $F = 1$ in a homogeneous environment with $\mathbf{E}_s = \mathbf{0}$.

In the special case that the optical environment is an optical cavity with resonant wavelength λ_a, quality factor Q and mode volume V_{eff}, the Purcell factor is reduced to its original expression derived by Purcell in 1946 [1, 45]

$$F = 1 + \frac{2g^2}{\kappa\gamma_0} = 1 + \frac{3}{4\pi^2}\left(\frac{\lambda_a}{n_B}\right)^3\frac{Q}{V_{eff}} \tag{1.14}$$

This expression is explicitly derived in Section 2.8.1.

Optical Lamb Shift

The re-excitation does not only enhance the emitter's emission rate but also shift its emission frequency. This shift is called an optical Lamb shift and has the following expression [44]

$$\frac{\omega_{em}^{L} - \omega_{em}}{\gamma_0} = \frac{3\pi\varepsilon_0 c^3}{n_B \omega_{em}^3 |\boldsymbol{\mu}|^2} \mathrm{Re}\left[\boldsymbol{\mu}^* \cdot \mathbf{E}_s(\mathbf{r}_{em})\right] \tag{1.15}$$

where ω_{em}^{L} is the Lamb shifted transition frequency of the emitter.

Optical Local Density of States

This section has so far only discussed the classical description of a quantum emitter. This can be linked to the quantum mechanical description by defining the optical local density of states (LDOS)

$$\rho_d(\mathbf{r}_{em}; \omega_{em}) = \frac{6\omega_{em}}{\pi c^2} \mathrm{Im}\left[\hat{\mathbf{e}}_\mu \cdot \mathbf{G}(\mathbf{r}_{em}, \mathbf{r}_{em}; \omega_{em}) \cdot \hat{\mathbf{e}}_\mu\right] \tag{1.16}$$

where $\hat{\mathbf{e}}_\mu = \boldsymbol{\mu}/|\boldsymbol{\mu}|$ is the dipole moment unit vector and $\mathbf{G}$ is the dyadic Green's function which is defined by the electric field generated by the dipole source

$$\mathbf{E}(\mathbf{r}) = \mu_0 \omega_{em}^2 \mathbf{G}(\mathbf{r}, \mathbf{r}_{em}; \omega_{em}) \cdot \boldsymbol{\mu}. \tag{1.17}$$

On the basis of Fermi's golden rule, the total decay rate γ_{tot} of the emitter in Eq. (1.12) can then be expressed in terms of the LDOS as [44]

$$\gamma_{tot} = \frac{\omega_{em}}{3\hbar\varepsilon_0} |\boldsymbol{\mu}|^2 \rho_d(\mathbf{r}_{em}; \omega_{em}). \tag{1.18}$$

1.2.3 From Weak- to Strong-Coupling: Coupled Oscillator Model

To demonstrate the transition between the weak- and strong-coupling regimes, this section considers a simple physical model of two coupled oscillators with masses m_1 and m_2. Each oscillator is attached to two springs connecting it to a fixed position and the other oscillator, as shown in Fig. 1.3(a). These three spring with spring

constants k_1, k_2 and k_g can be can be represented by the resonant frequencies $\omega_1 = \sqrt{(k_1 + k_g)/m_1}$ and $\omega_2 = \sqrt{(k_2 + k_g)/m_2}$ and the coupling frequencies $g_{12} = \sqrt{k_g/m_1}$ and $g_{21} = \sqrt{k_g/m_2}$. We can study how the system respond to an external force by considering the case where only the first oscillator is driven by a force $f = f_0 \exp(-i\omega t)$ which then drives the second oscillator through their coupling. Assuming that the oscillators are subject to damping rate Γ_1 and Γ_2, the resulting equations of motion are []

$$\frac{d^2x_1}{dt^2} + 2\Gamma_1 \frac{dx_1}{dt} + \omega_1^2 x_1 - g_{12}^2 x_2 = \frac{f}{m_1} \tag{1.19}$$

$$\frac{d^2x_2}{dt^2} + 2\Gamma_2 \frac{dx_2}{dt} + \omega_2^2 x_2 - g_{21}^2 x_1 = 0 \tag{1.20}$$

where x_1 and x_2 are the oscillators' displacements from their equilibriums. To find the steady state solutions, we assume $x_1(t) = A_1 \exp(-i\omega t)$ and $x_2(t) = A_2 \exp(-i\omega t)$ and obtain

$$A_1 = \frac{\omega_2^2 - \omega^2 - 2i\Gamma_2\omega}{(\omega_1^2 - \omega^2 - 2i\Gamma_1\omega)(\omega_2^2 - \omega^2 - 2i\Gamma_2\omega) - g_{12}^2 g_{21}^2} \cdot \frac{f_0}{m_1} \tag{1.21}$$

$$A_2 = \frac{g_{21}^2}{(\omega_1^2 - \omega^2 - 2i\Gamma_1\omega)(\omega_2^2 - \omega^2 - 2i\Gamma_2\omega) - g_{12}^2 g_{21}^2} \cdot \frac{f_0}{m_1}. \tag{1.22}$$

The average power dissipated in the system is equal to

$$\begin{aligned} \langle P(\omega) \rangle &= \frac{1}{2} \mathrm{Re}\left[f^* \cdot \frac{dx_1}{dt} \right] \\ &= \frac{1}{2} \mathrm{Re}\left[\frac{-i\omega(\omega_2^2 - \omega^2 - 2i\Gamma_2\omega)}{(\omega_1^2 - \omega^2 - 2i\Gamma_1\omega)(\omega_2^2 - \omega^2 - 2i\Gamma_2\omega) - g_{12}^2 g_{21}^2} \right] \cdot \frac{|f_0|^2}{m_1}. \end{aligned} \tag{1.23}$$

The resonances of the system can be obtained from the denominator of Eq. (1.23)

$$(\omega_1^2 - \omega^2 - 2i\Gamma_1\omega)(\omega_2^2 - \omega^2 - 2i\Gamma_2\omega) - g_{12}^2 g_{21}^2 = 0. \tag{1.24}$$

In the simple case where $\omega_1 = \omega_2 = \omega_0$, $\Gamma_1 = \Gamma_2 = \Gamma$ and $m_1 = m_2 = m$, the system has two solutions with positive frequencies

$$\omega_\pm = -i\Gamma + \sqrt{\omega_0^2 - \Gamma^2 \pm g^2}. \tag{1.25}$$

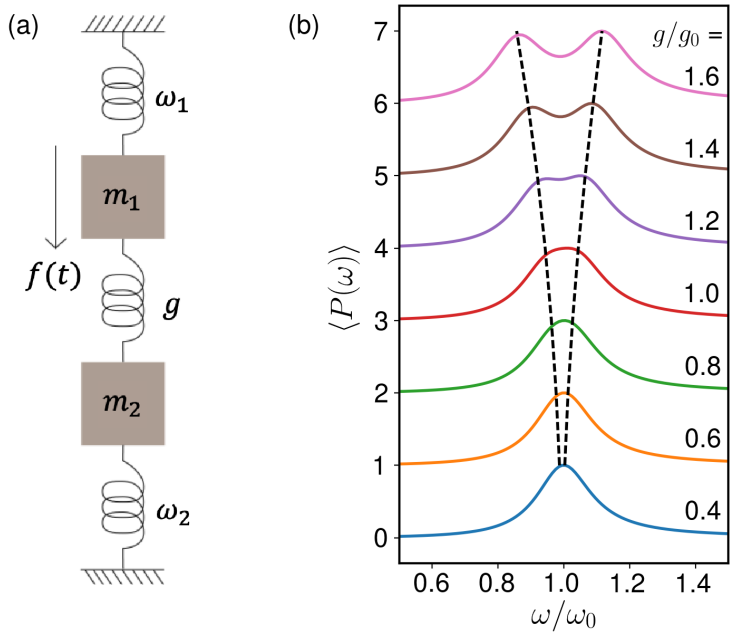

Figure 1.3: (a) A schematic for harmonic oscillators with masses $m_1 = m_2 = m$, damping $\Gamma_1 = \Gamma_2 = \Gamma$ and resonant frequencies $\omega_1 = \omega_2 = \omega_0$. The oscillators are coupled with coupling strength g, and the first oscillator is driven by a force $f(t)$. (b) Average power spectra $\langle P(\omega) \rangle$ of the oscillators with coupled strength $g/g0$ from 0.4 to 1.6, where $g_0 = \sqrt{\Gamma \omega_0}$. Each result is normalized by its maximum and is offset for clarity. When $g/g0 > 1$., the system is in the strong-coupling regime, and energy splitting is observed. The dashed lines indicate the resonant frequencies $\mathrm{Re}[\omega_\pm]$.

Assuming $\omega_0 \gg \Gamma, g$, a simple expression for the energy splitting can be derived

$$\begin{aligned} \Delta\omega &= \omega_+ - \omega_- \\ &\approx g^2/\omega_0. \end{aligned} \tag{1.26}$$

The criterion for the strong-coupling regime is obtained when the oscillators exchange energy at a faster rate than their energy dissipation. This is identical to the condition in which the energy splitting is spectrally resolved $\Delta\omega > \Gamma$, i.e. $g > \sqrt{\Gamma\omega_0}$. This behaviour is demonstrated in Fig. 1.3(b). For $g < g_0$, the energy splitting is too small to be resolved, and $\langle P(\omega) \rangle$ shows only single broaden peaks. For $g > g_0$, two peaks in $\langle P(\omega) \rangle$ become visible. This energy splitting in the system's spectrum is called the Rabi splitting.

For general coupled systems, such as the coupling between a quantum emitter and a plasmonic resonance, the damping Γ_1 and Γ_2 can be drastically different, and general solutions can be obtained from solving Eq. (1.24). Although this section presents a simple harmonic oscillator model, the qualitative behaviors of the weak- and strong-

coupling regimes are a general physical phenomenon of coupled systems, including the coupling between a quantum emitter and a plasmonic resonance.

1.3 SUMMARY OF METHODS

Many attempts have been made to model the coupling between quantum emitters and plasmonic nanocavities. The most simple model is the classical model where light is modeled with Maxwell's equations and the emitters as simple classical Lorentz oscillators (i.e. a classical dipole) [46, 47]. The Lorentz oscillator model, however, fails in the nonlinear regime and can be superseded by a semiclassical model where the emitters are treated as two-level quantum systems [48]. The system can also be modeled quantum mechanically by quantizing the field of the plasmonic modes in the master equation approach with Jaynes-Cummings Hamiltonian [49, 50]. However, the quantum model is limited by the fact that the plasmonic resonances have to be predefined and its inability to model plasmonic nanostructures in a full-wave form. Alternatively, the system could also be simulated with ab initio methods where the most notable is time-dependent density functional theory (TDDFT) [51]. However, this method is limited to very small nanostructures due to its high computational expense. All the aforementioned models predict qualitatively similar results in the weak-excitation regime and for gap sizes larger than 1 nm [15, 52].

This thesis studies different aspects of plasmonic nanocavities and their interaction with quantum emitters by using a collection of numerical and analytical methods, including classical, semi-classical and quantum mechanical methods. These methods are summarized below.

1.3.1 Classical Methods

In this thesis, the optical properties of plasmonic nanocavities are well described by classical Maxwell's equations, and their plasmonic resonances are mainly solved by ei-

ther the finite-element method (FEM) [53] in Comsol Multiphysics version 5.4 or the finite-difference time-domain (FDTD) method [54] in Lumerical FDTD version 8.18.1298. These methods have different advantages and disadvantages. The FEM in Comsol provides a more efficient meshing scheme and, in general, more efficient computations. It is also capable of solving both frequency-domain and time-domain problems. On the other hand, the FDTD method in Lumerical can only solve time-domain problems but provide more robust computations.

Both types of numerical simulations for plasmonic nanocavities require identical boundary conditions and similar spatial discretization. To truncate an infinite space into finite simulation space, plasmonic nanocavities are surrounded by perfectly matched layers (PMLs) which absorb incident fields with minimal reflection. Since this thesis deals with a few nanometer gap size between two much larger plasmonic structures (nanoparticles with diameters of 40-100 nm), a uniform meshing scheme is impractical and requires unrealistically expensive computation time. Hence, an adaptive meshing scheme is utilized for all simulations in this thesis. For example, a NPoM with a diameter of 40 nm and a gap of 1 nm requires mesh refinements of 0.25 nm at the gap and 2 nm at the nanoparticle.

In the following, several techniques based on the FEM and FDTD methods are outlined.

FEM: QNMEig

For general dispersive materials, their resonances (quasinormal modes) can be obtained by solving non-linear eigenproblems. These problems can be converted into linear forms by introducing auxiliary fields, as shown in Section 2.3. An open-source program based on Comsol Multiphysics called QNMEig [55] implements such conversions. This method is used in Chapter 2 to calculate for resonances (gap plasmons) of NPoM nanocavities, including Figs. 2.2(b-e), 2.3 and 2.4.

FEM: RETOP

Once near-field profiles of a nanocavity's resonances are found, far-field radiation from the nanocavity can then be calculated by projecting the near-field electric and

magnetic fields to the far-field by using an open-source program RETOP [56]. This method uses the results from QNMEig to obtain the results in Figs. 2.5 and 2.9.

FEM: Direct Dipole Radiation

Instead of solving for resonances, the optical properties of a plasmonic nanocavity can also be studied by directly placing an electric dipole inside the nanogap. The dipole generates radiation which, in principle, excites all available resonances of the nanocavity. Together with RETOP, this method is used to obtain far-field results in Fig. 2.10.

FDTD: Resonant States

Similar to QNMEig, resonances (quasinormal modes) of an optical structure could also be found by the FDTD method. This thesis follows the technique described in Ref. [57] to calculate resonant fields and Purcell enhancement of a NPoM nanocavity as shown in Fig. 4.6.

FDTD: Fluorescence Emission

Fluorescence emission from a quantum emitter [14, 58] is a two-step process, namely excitation and emission; hence, calculating fluorescence requires two separate electromagnetic simulations. Using the FDTD method, the excitation simulation could be carried out by injecting incident waves from a total-field scattered-field (TFSF) source [54] into the nanocavity and the emitter. The excitation rate on the emitter is then proportional to electric field enhancement at the emitter's position. For the emission simulation, a dipole source could be placed at the emitter's position, and the emission rate of the emitter is then proportional to enhanced radiated power from the dipole. This technique is used to obtain the results in Figs. 3.1(a-c), 3.2, 3.3, 3.5(b-e) and 3.6(b).

FDTD: Cross-Section

Similar to the excitation simulation for fluorescence emission, optical cross-sections of a plasmonic nanocavity can be calculated by using a TFSF source in a FDTD simulation. Absorption and scattering cross-sections can then be calculated from the scattered fields

inside and outside the TFSF source, respectively [30]. This technique is used to calculate cross-sections in Figs. 3.4(b,c), 3.9 and 4.1.

1.3.2 Semi-classical Method: Maxwell-Bloch Equations

To study energy exchange dynamics between a quantum emitter and plasmonic resonances, this thesis mainly employs a semi-classical description for the emitter. In the regime, electromagnetic fields are treated classically by using Maxwell's equations whereas the emitter is treated quantum mechanically by using Maxwell-Bloch equations [59]. This approach provides computational efficiency and flexibility for simulating plasmonic nanocavities while retaining quantum mechanical information about the emitter, such as its population inversion and coherence properties. Two variants of the Maxwell-Bloch model, based on the FDTD framework, are used in Chapters 3 and 4.

FDTD: $1\times1\times1$ nm^3 Emitter

In Chapters 3, a quantum emitter is modeled as a $1\times1\times1$ nm^3 cube with a linewidth of 28 meV and a dipole moment of 3.79 Debyes which is aligned perpendicularly to the substrate of a NPoM. The emitter's optical properties are described the standard Maxwell-Bloch equation [59]. This method is used to obtain the results in Figs. 3.7, 3.8 and 3.9.

FDTD: Single-Yee-Cell Emitter

Chapter 4 considers a quantum emitter with a much larger dipole moment than that in Chapter 3. If a $1\times1\times1$ nm^3 emitter model is used for an emitter with such a large dipole moment, then the emitter experiences a significant numerical self-interaction [60]. Here, the emitter is instead modeled as a single-Yee-cell emitter placed inside the gap of a hemisphere dimer structure. The polarization of the emitter is modified with field corrections, as described in Ref. [60]. The emitter has a dipole moment of 20 Debyes aligned parallel to the substrate along the gap and linewidth of 26 meV. This method is used to obtain the results in Figs. 4.3, 4.4, 4.7, 4.8 and 4.9.

1.3.3 Quantum Mechanical Method: Lindblad Master Equation

As described above, plasmonic resonances of plasmonic nanocavities are well described in the classical regime. However, some phenomena such as spontaneous emission are inherently quantum mechanical. Hence, a proper calculation on emitter photoluminescence requires quantizing electromagnetic fields. This thesis employs Jaynes-Cummings Hamiltonian to describe optical interaction between the emitter and plasmons and then calculates their photoluminescence by solving Lindblad master equation [42]. This method is used to obtain the results in Figs. 4.6 and 4.7.

1.4 SUMMARY OF CONTENTS

This thesis investigates the optical properties of plasmonic nanocavities and their interaction with single quantum emitters in the weak- and strong-coupling regimes. The thesis is organized into five chapters, including Introduction presented here. Chapter 2 explores the morphology-dependent near-field and far-field behaviours of NPoM nanocavities, of which optical resonances are treated classically as leaky modes with complex eigenfrequencies. Their complex coupling coefficients to single quantum emitters, modeled as classical dipole sources, are then derived and used to reveal intricate multi-modal interaction. Chapter 3 challenges the previously held assumption that fluorescence emission from an emitter is always quenched when the emitter is placed a few nanometers away from a metal surface. This chapter demonstrates that fluorescence quenching is, in fact, suppressed inside a plasmonic nanocavity and also show that this phenomenon enables the system to facilitate strong-coupling with a single emitter. Based on the concept of single-emitter strong-coupling, Chapter 4 uses a combination of semi-classical and quantum mechanical methods to propose an innovative scheme of quantum plasmonic immunoassay sensing. In this scheme, an antibody-antigen-antibody complex is chemically linked with a quantum emitter label which is strongly coupled with plasmons in a hemisphere-dimer nanocavity, resulting in massively en-

hanced sensitivity. Finally, summary and outlooks of this thesis are given in Chapter 5.

2 QUASINORMAL-MODE ANALYSIS OF PLASMONIC NANOCAVITIES

The results presented in this chapter have been published as a preprint in Ref. [61], co-authored by A. Demetriadou, M. Horton, R. Chikkaraddy, J. J. Baumberg and O. Hess. Some parts of this chapter are quoted verbatim from the published manuscript.

I contributed to all analytic calculations, ran the numerical simulations, performed the data analysis and prepared all figure. All authors contributed to the discussion of the content in this chapter.

2.1 INTRODUCTION

A wide range of theoretical and experimental studies have been conducted to investigate the optical properties of NPoM nanocavities [36, 62, 63]. Several studies examine resonances of NPoMs [40, 64–67] and their influence on optical emission of single molecules in the nanogaps [39, 68, 69]. However, most studies on the nanocavities have so far described their optical response via a scattering method and infer their resonances from resulting far-field spectral peaks. Although significant information can be obtained from the far-field spectra, they do not reveal complete optical descriptions of the nanocavities and commonly hide information about their dark modes. For example, an incident field from the far-field does not couple to all available photonic modes of the system. Resonances which are spectrally close also interfere with each other and often merge into single broadened peaks in far-field spectra. As a result, analyses of the far-field scattered spectra can yield inconsistency between near-field and far-field plasmonic responses [70].

The precise morphological details of the NPoM nanogaps also dramatically modify their optical responses [64, 71]. Once the nanoparticles are placed on substrates, they lie

on their facets which can have varying widths. Previous studies of the gap morphology of NPoMs described their gap plasmonic resonances with two sets of modes: longitudinal antenna modes, excited for all facet widths, and transverse waveguide modes, excited at large facet widths [65, 66]. Although this description sheds light upon the asymptotic behavior of the NPoM plasmons, it provides an incomplete picture of NPoM resonances at intermediate facet widths.

Here, the inherent resonant states of the NPoM geometry are identified and mapped by employing the quasinormal mode (quasinormal mode (QNM)) method [72]. We propose a simple yet comprehensive nomenclature based on spherical harmonics to describe the resonances of NPoMs with varying morphology. A collection of spectrally overlapping bright and dark nanogap QNMs are reported, including some photonic modes that have not been reported elsewhere. These results imply that a quantum emitter placed inside a NPoM nanogap couples to a collection of QNMs and experiences a complex multi-modal interaction. By calculating the far-field emission of each QNM using a near-to-far field transformation (NFFT) method, we predict the total emission profile of a dipole emitter placed inside a NPoM nanogap from the QNM collective responses. The resulting emission profiles display rich and intricate behaviors, governed by the NPoM morphology.

2.2 QNMS IN NANOPHOTONICS

A general open system is non-conservative as its energy leaks to its external environment, and its time-evolution is non-Hermitian. Consequently, its resonance can no longer be described by a normal mode but, instead, is characterized by a QNM with a complex eigenfrequency [73]. The QNM analysis has been a standard method to study open and dissipative systems, of which the approximate descriptions are often provided by a few QNMs. This approach has spanned a wide range of applications, including gravitational waves from black holes [74] and electromagnetic waves from nanoresonators [72].

In nanophotonics, significant progress has been made in the past decades towards solving QNMs for general dispersive materials. Efficient QNM solvers have been developed using a variety of techniques, including the time-domain approach [57, 75], the pole-search approach [76–78] and auxiliary-field eigenvalue approach [55]. For resonators with arbitrary shapes and materials, analytic solutions are not generally available, and several numerical methods have been developed which surround the resonators by PMLs to approximately simulate infinite domains [55, 79].

Despite these recent developments, the widespread use of the QNM formalism in plasmonics has yet to be achieved, and most studies in plasmonic systems still resort to analyzing their scattering properties and assigning resonances to the corresponding spectral peaks, see Fig. 2.1(a). The scattering approach is not at all optimal. Firstly, some resonances may not couple with the incident field and remain undetected. Secondly, resonances which are spectrally close interfere with each other and often merge into single broadened peaks. As a result, scattering analyses often yield inconsistent results, depending on how the systems are excited and where their spectra are collected. To demonstrate these problems, Fig. 2.1(d) shows the spectrum of three dummy real-frequency resonances[1] with Lorentzian lineshapes, $A/(\omega-(\omega_i-i\kappa_i))$

$$f(\omega)=\left|\frac{1.4\exp(2\pi i)}{\omega-(0.5-0.4i)}+\frac{0.12\exp(0.2\pi i)}{\omega-(1.0-0.1i)}+\frac{0.08\exp(0.8\pi i)}{\omega-(1.5-0.02i)}\right|^2. \tag{2.1}$$

The interference between these resonances distorts their amplitudes, shapes and peak positions. For a plasmonic structure, its resonances often spectrally overlap and interfere with each other, hiding individual resonances from the optical spectrum and rendering real-frequency analysis ineffective.

Fig. 2.1(e) shows a more effective analysis by representing the resonances as QNMs with complex frequencies

$$\widetilde{\omega}_i=\omega_i-i\kappa_i \tag{2.2}$$

where the real part ω_i is the spectral position and the imaginary part κ_i is the linewidth, i.e., dissipation rate. The minus sign ensures that the resonances decay with time, for example the field amplitude $A(t)\propto\exp(-i\widetilde{\omega}_i t)=\exp(-\kappa_i t)\exp(-i\omega_i t)$.

1 The dummy resonances are for the demonstration purpose and do not belong to any optical system.

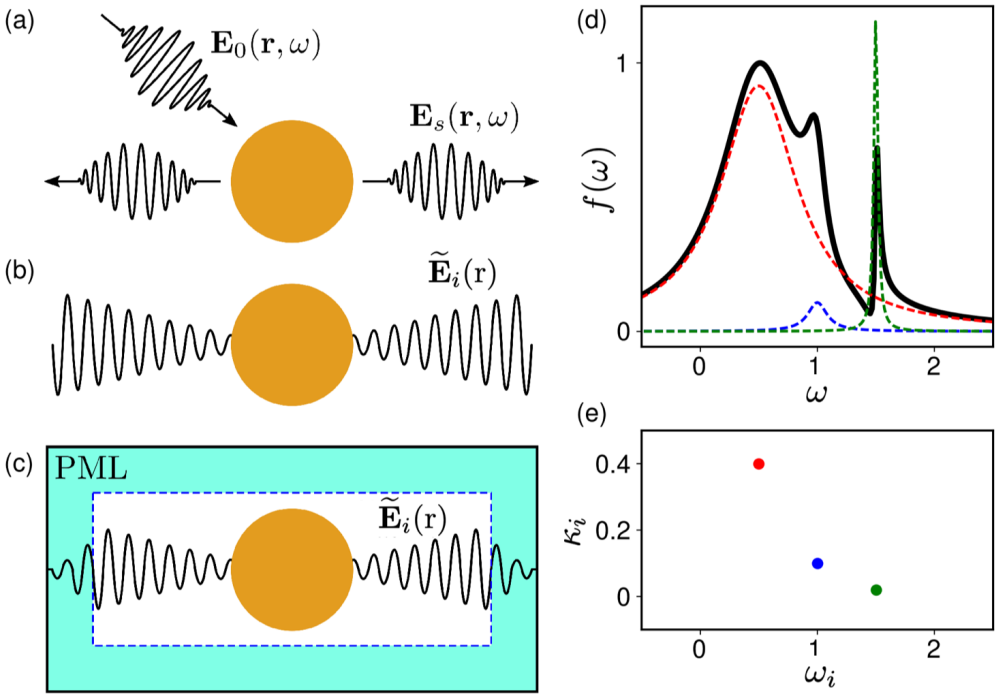

Figure 2.1: (a) A schematic for a real frequency, ω, method. An electromagnetic resonator is excited by an incident field $\mathbf{E}_0$ and produces a scattering field $\mathbf{E}_s$. (b) A schematic for the complex frequency, $\tilde{\omega}_i = \omega_i - i\kappa_i$, QNM method. A leaky resonant mode of the resonator is described by a field $\widetilde{\mathbf{E}}_i$. (c) The QNM method calculated in a finite space with PMLs. (d) Scattering spectrum $f(\omega)$ of three dummy resonant modes obtained by the real frequency method. (e) A complex frequency representation of the dummy resonant modes.

For a general optical system with non-magnetic materials, its QNMs can be found by solving the time-harmonic, $\partial/\partial t \to -i\omega$, and source-free, $\mathbf{J}_{ext} = \rho_{ext} = 0$, Maxwell's equations (A.3,A.4) [72]

$$\begin{pmatrix} 0 & -i\mu_0^{-1}\nabla\times \\ i\varepsilon(\mathbf{r};\tilde{\omega}_i)^{-1}\nabla\times & 0 \end{pmatrix} \begin{pmatrix} \widetilde{\mathbf{H}}_i(\mathbf{r}) \\ \widetilde{\mathbf{E}}_i(\mathbf{r}) \end{pmatrix} = \tilde{\omega}_i \begin{pmatrix} \widetilde{\mathbf{H}}_i(\mathbf{r}) \\ \widetilde{\mathbf{E}}_i(\mathbf{r}) \end{pmatrix}, \tag{2.3}$$

where $\widetilde{\mathbf{H}}_i$ and $\widetilde{\mathbf{E}}_i$ are QNM magnetic and electric fields, respectively. These QNM fields satisfy the Sommerfeld radiation condition for outgoing waves at $|\mathbf{r}| = r \to \infty$. Unlike real-frequency normal modes, the QNMs have unique properties such that their fields diverge in space as $r \to \infty$. For example, a spherical outgoing wave of the form $A(\mathbf{r},t) \propto \exp[-i\tilde{\omega}_i(t - r/c)]/r$ grows as $\exp[\kappa_i r/c)]/r$, as shown in Fig. 2.1(b). In numerical studies, this behavior can be addressed by introducing absorbing PMLs which suppress the diverging QNM fields in a finite computational space, as shown in Fig. 2.1(c).

There are two main difficulties associated with solving for QNMs in dispersive systems. Firstly, Eq. (2.3) is generally a nonlinear eigenvalue problem because ε is a function of the complex eigenvalue $\widetilde{\omega}_i$. Secondly, diverging behavior also causes difficulties in normalizing QNMs and finding their orthogonality relation. This chapter discusses both problems and their solutions below.

2.3 AUXILIARY-FIELD EIGENVALUE APPROACH

For dispersive materials like metals, Eq. (2.3) is, in general, a nonlinear eigenvalue equation. However, Eq. (2.3) can be converted into a linear equation if the material permittivities are described by the N-pole Lorentz-Drude permittivity (see Section A.2)

$$\varepsilon(\omega) = \varepsilon_\infty \left(1 - \sum_{k=1}^{N} \frac{\omega_{p,k}^2}{\omega^2 - \omega_{0,k}^2 + i\gamma_k \omega} \right) \tag{2.4}$$

where ε_∞ is the asymptotic permittivity at infinite frequency while $\omega_{p,k}$, $\omega_{0,k}$ and γ_k are the plasma frequency, resonant frequency and decay rate, respectively, of the k^{th} Lorentz-Drude pole. For each Lorentz-Drude pole in the summation, two auxiliary fields can be introduced [55]

$$\widetilde{\mathbf{P}}_{i,k}(\mathbf{r}) = -\frac{\varepsilon_\infty \omega_{p,k}^2}{\widetilde{\omega}_i^2 - \omega_{0,k}^2 + i\gamma_k \widetilde{\omega}_i} \widetilde{\mathbf{E}}_i(\mathbf{r}), \tag{2.5}$$

$$\widetilde{\mathbf{J}}_{i,k}(\mathbf{r}) = -i\widetilde{\omega}_i \widetilde{\mathbf{P}}_{i,k}(\mathbf{r}), \tag{2.6}$$

where $\widetilde{\mathbf{P}}_{i,k}$ and $\widetilde{\mathbf{J}}_{i,k}$ are auxiliary polarization and current, respectively, of the i^{th} QNM and the k^{th} Lorentz-Drude pole. In the case of gold with two-pole Lorentz-Drude permittivity (see Section A.2.3), Eq. (2.3) can be transformed into

$$\widehat{\mathcal{H}} \widetilde{\psi}_i = \widetilde{\omega}_i \widetilde{\psi}_i, \tag{2.7}$$

$$\widetilde{\psi}_i = \begin{pmatrix} \widetilde{\mathbf{H}}_i(\mathbf{r}) & \widetilde{\mathbf{E}}_i(\mathbf{r}) & \widetilde{\mathbf{P}}_{i,1}(\mathbf{r}) & \widetilde{\mathbf{J}}_{i,1}(\mathbf{r}) & \widetilde{\mathbf{P}}_{i,2}(\mathbf{r}) & \widetilde{\mathbf{J}}_{i,2}(\mathbf{r}) \end{pmatrix}^T \tag{2.8}$$

$$\widehat{\mathcal{H}} = \begin{pmatrix} 0 & -i\mu_0^{-1}\nabla\times & 0 & 0 & 0 & 0 \\ i\varepsilon_\infty^{-1}\nabla\times & 0 & 0 & -i\varepsilon_\infty^{-1} & 0 & -i\varepsilon_\infty^{-1} \\ 0 & 0 & 0 & i & 0 & 0 \\ 0 & i\omega_{p,1}^2\varepsilon_\infty & -i\omega_{0,2}^2 & -i\gamma_1 & 0 & 0 \\ 0 & 0 & 0 & 0 & 0 & i \\ 0 & i\omega_{p,2}^2\varepsilon_\infty & 0 & 0 & -i\omega_{0,2}^2 & -i\gamma_2, \end{pmatrix}. \tag{2.9}$$

This approach, in effect, converts a nonlinear problem into a linear problem in a larger vector space.

2.4 UNCONJUGATED FORM OF LORENTZ RECIPROCITY THEOREM

The previous section addresses the problem of the nonlinear eigenvalue equation. Before addressing the problems of normalizing QNMs and finding their orthogonality relations, this section derives a prerequisite theorem which is the Lorentz reciprocity theorem [80].

First, the time harmonic Maxwell's equations are considered, $\partial/\partial t \to -i\omega t$, where Eqs. (A.3) and (A.4) can be rewritten as

$$\nabla \times \mathbf{E} = i\omega\mu_0\mathbf{H} \tag{2.10}$$

$$\nabla \times \mathbf{H} = -i\omega\varepsilon(\mathbf{r};\omega)\mathbf{E} + \mathbf{J}_{ext}. \tag{2.11}$$

Assuming that there are two different solutions to Maxwell's equations $(\mathbf{H}_1, \mathbf{E}_1, \omega_1, \mathbf{J}_1)$ and $(\mathbf{H}_2, \mathbf{E}_2, \omega_2, \mathbf{J}_2)$, the divergence theorem can be applied to the vector $\mathbf{E}_2 \times \mathbf{H}_1 - \mathbf{E}_1 \times \mathbf{H}_2$ in order to derive [2] [79, 80]

$$\begin{aligned} \iint_\Sigma (\mathbf{E}_2 \times \mathbf{H}_1 - \mathbf{E}_1 \times \mathbf{H}_2)\, d^2\mathbf{r} = {} & i\iiint_\Omega \mathbf{E}_1 \cdot [\omega_1\varepsilon(\mathbf{r};\omega_1) - \omega_2\varepsilon(\mathbf{r};\omega_2)]\,\mathbf{E}_2\, d^3\mathbf{r} \\ & - i\iiint_\Omega \mu_0\mathbf{H}_1 \cdot (\omega_1 - \omega_2)\mathbf{H}_2\, d^3\mathbf{r} \\ & - \iiint_\Omega (\mathbf{J}_1 \cdot \mathbf{E}_2 - \mathbf{J}_2 \cdot \mathbf{E}_1)\, d^3\mathbf{r} \end{aligned} \tag{2.12}$$

2 This derivation requires the identity $\nabla \cdot (\mathbf{A} \times \mathbf{B}) = (\nabla \times \mathbf{A}) \cdot \mathbf{B} - \mathbf{A} \cdot (\nabla \times \mathbf{B})$.

where Σ is a closed surface surrounding a domain Ω. In the special case where $\omega_1 = \omega_2$ and Σ is infinitely large, the surface-integral terms cancel, and Eq. (2.12) reduces to

$$\iiint_{\Omega} (\mathbf{J}_1 \cdot \mathbf{E}_2 - \mathbf{J}_2 \cdot \mathbf{E}_1)\, d^3\mathbf{r} = 0. \tag{2.13}$$

This expression is called the Rayleigh-Carson reciprocity theorem [80]. It implies that the relationship between a current source and its resulting electromagnetic fields remains unchanged if the source's position is interchanged with the position where the fields are measured. This concept shows the reversible roles of transmitting and receiving antennas and is essential for developing antenna theory.

2.5 QNM ORTHOGONALITY RELATION AND NORMALIZATION

This section uses Eq. (2.12) to derive the orthogonality relation and normalization. Considering the i^{th} QNM solution ($\mathbf{H}_1 = \widetilde{\mathbf{H}}_i, \mathbf{E}_1 = \widetilde{\mathbf{E}}_i, \omega_1 = \widetilde{\omega}_i, \mathbf{J}_1 = 0$) and j^{th} QNM solution ($\mathbf{H}_2 = \widetilde{\mathbf{H}}_j, \mathbf{E}_2 = \widetilde{\mathbf{E}}_j, \omega_2 = \widetilde{\omega}_j, \mathbf{J}_2 = 0$), the orthogonality relation can be obtained by dividing Eq. (2.12) by $\widetilde{\omega}_j - \widetilde{\omega}_i$ [72, 79]

$$\iiint_{\Omega} \left[\widetilde{\mathbf{E}}_j \cdot \frac{\widetilde{\omega}_j \varepsilon(\mathbf{r}; \widetilde{\omega}_j) - \widetilde{\omega}_i \varepsilon(\mathbf{r}; \widetilde{\omega}_i)}{\widetilde{\omega}_j - \widetilde{\omega}_i} \widetilde{\mathbf{E}}_i - \mu_0 \widetilde{\mathbf{H}}_j \cdot \widetilde{\mathbf{H}}_i \right] d^3\mathbf{r} = 0. \tag{2.14}$$

The QNM normalization can then be defined from the orthogonality relation by performing Taylor expansion on the first term in the limit $\widetilde{\omega}_j \to \widetilde{\omega}_i$

$$\iiint_{\Omega} \left[\widetilde{\mathbf{E}}_i \cdot \left(\frac{\partial [\omega \varepsilon(\mathbf{r}; \omega)]}{\partial \omega} \right)_i \widetilde{\mathbf{E}}_i - \mu_0 \widetilde{\mathbf{H}}_i \cdot \widetilde{\mathbf{H}}_i \right] d^3\mathbf{r} = 1 \tag{2.15}$$

where the derivative is evaluated at $\omega = \widetilde{\omega}_i$. For non-dispersive materials, where $\varepsilon(\mathbf{r}; \omega) = \varepsilon(\mathbf{r})$, Eqs. (2.14) and (2.15) become

$$\iiint_{\Omega} \left[\varepsilon(\mathbf{r}) \widetilde{\mathbf{E}}_j \cdot \widetilde{\mathbf{E}}_i - \mu_0 \widetilde{\mathbf{H}}_j \cdot \widetilde{\mathbf{H}}_i \right] d^3\mathbf{r} = \delta_{i,j}. \tag{2.16}$$

In a numerical simulation, an infinite system domain Ω can be represented as a finite computational domain with PMLs surrounding a nanostructure. In such a simulation, the integrations over Ω in Eqs. (2.14), (2.15) and (2.16) must include the field contributions inside the PMLs.

2.6 QNMS OF NPOMS

This chapter studies a gold NPoM structure with commonly used geometrical and optical parameters in recent experiments [24, 64], i.e., nanoparticle diameter of $2R = 80$ nm, gap thickness of $d = 1$ nm, refractive index $n_{gap} = 1.45$ and background refractive index $n_b = 1.0$, as shown in Fig. 2.2(a). The permittivity of gold is modeled by a two-pole Lorentz-Drude permittivity, given in Eq. (A.16). Real metal nanoparticles are always faceted and lie on their facets with varying widths on a substrate [64, 71]. Since the gap plasmonic resonances are highly sensitive to the gap morphology, the gold nanoparticles are modeled as truncated spheres with facet widths w from 0 to 40 nm. The remaining nanoparticle facets outside the gap region do not play any significant role.

2.6.1 QNMs of Spherical and Faceted NPoMs

To calculate the QNMs of a gold NPoM structure, we employ the above methodology by using QNMEig, an open-source program based on COMSOL Multiphysics, which implements an efficient finite-element solver by accounting for material dispersion with auxiliary fields [55]. The following parameters are chosen based on recent experiments [24, 64], with nanoparticle diameter of $2R = 80$ nm, gap thickness $d = 1$ nm, refractive index $n_{gap} = 1.45$ and background refractive index $n_b = 1.0$, as shown in Fig. 2.2(a).

This chapter chooses a simpler yet highly effective nomenclature based on spherical harmonics Y_ℓ^m. Each QNM is labelled with $i = (\ell m)$ where $\ell = 0, 1, 2, \ldots$ and $-\ell \leqslant m \leqslant \ell$. Inside a spherical metal nanoparticle in a homogeneous environment, spherical harmonics form a complete set of orthogonal basis functions for its plasmonic modes

[72, 81]. For an NPoM, the surface charges on the nanoparticle are attracted by their image charges in the mirror and become densely distributed near the gap, forming gap plasmons. Surprisingly, this chapter discovers that the formation of gap plasmons preserves the labels (ℓm) for all facet widths even though the surface charges can no longer be described by Y_ℓ^m.

Figure 2.2(b-c) show the real z-component of QNM fields $E_{z,\ell m} = \mathrm{Re}[\tilde{\mathbf{E}}_{\ell m} \cdot \hat{\mathbf{e}}_z]$ for the two lowest-eigenfrequency QNMs, denoted as (10) and (11), of a spherical NPoM ($w =$ 0 nm). At the nanogap, these QNMs exhibit large field confinement far beyond the diffraction limit, which is the main characteristic of gap plasmons. The (10) QNM, also known as the BDP, is symmetric (even) across the $x = 0$ plane whereas the (11) QNM is antisymmetric (odd). Note that, unlike spherical harmonics with $Y_0^0 = 1/\sqrt{4\pi}$, the (00) QNM is not present in the calculations since it corresponds to a nanoparticle with a non-neutral net charge.

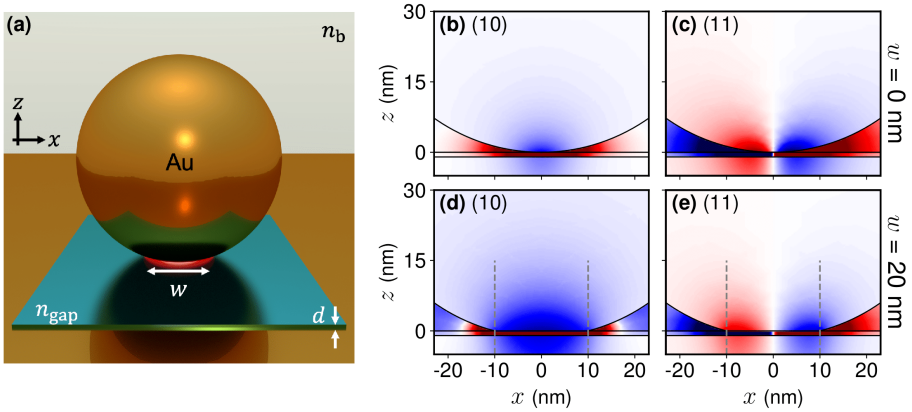

Figure 2.2: FEM simulations using QNMEig for QNM fields. (a) Schematic diagram for a gold nanoparticle-on-mirror (NPoM) structure with diameter $2R = 80$ nm, nanogap $d =$ 1 nm, nanogap index $n_{gap} = 1.45$, background index $n_b = 1$. The nanoparticle is modeled as a truncated sphere with facet width w. (b,c,d,e) QNM electric fields $E_{z,\ell m}$ (normalized between -1 and 1) are shown on a vertical xz-plane of an NPoM with (b,c) $w = 0$ and (d,e) 20 nm for (b,d) (10) and (c,e) (11) QNMs. The gray dashed lines indicate the facet edges.

Fig. 2.3(a-e) further explores the field profiles of the first five QNMs in the spherical NPoM nanogap where the label (ℓm) is assigned to each QNM according to its symmetries. The label ℓ determines the number of nodes and antinodes along the radial coordinates $r = \sqrt{x^2 + y^2}$ whereas the label m directly corresponds to the number of antinode pairs along the angular coordinate $\phi = \arctan(y/x)$ with $\tilde{\mathbf{E}}_{\ell m}(r, \phi, z) \propto \exp(im\phi)$. The

QNMs with $m = 0$ have a circular symmetry and antinodes at the center $r = 0$. On the other hand, the QNMs with $m \neq 0$ have nodes at the center which extend radially at angles $(2n + 1)\pi/2m$ for $n \in \mathbb{Z}^+$. For a given $m \neq 0$, each QNM with $\ell = m$ has only one node at the center, and each successive increment in ℓ gives one more node along r, as shown in Fig. 2.3(b,d,e). On the other hand, the $(\ell 0)$ QNMs display $\ell - 1$ nodes along r. Here, the QNMs with negative $m = -|m|$ are omitted since they are degenerate with those of the same ℓ but with positive $m = +|m|$. The field profile of the degenerate pair of each QNM can be easily obtained by rotating its fields by angle $\pi/2m$ over the z-axis.

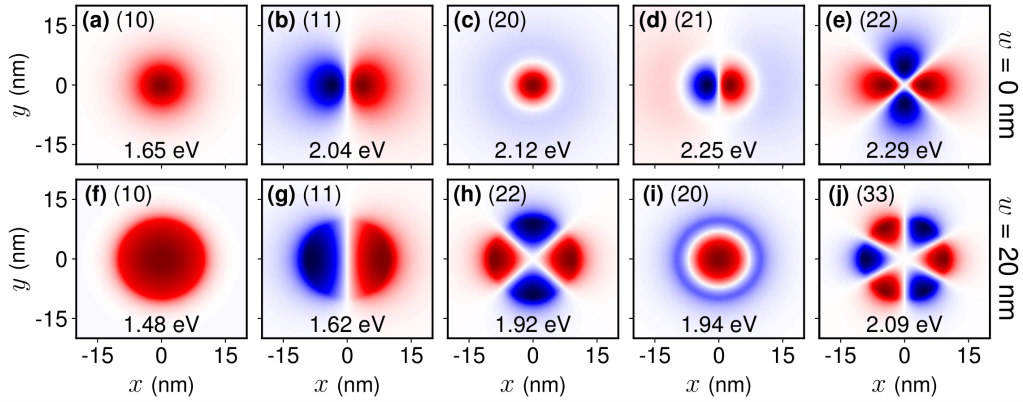

Figure 2.3: FEM simulations using QNMEig for the QNM electric fields $E_{z,\ell m}$ (normalized between -1 and 1). The fields are shown on the horizontal (xy) plane at the nanogap center for the first five QNMs of NPoMs with (a-e) $w = 0$ nm and (f-j) $w = 20$ nm. The real eigenfrequencies $\omega_{\ell m}$ in eV are shown at the bottom of all figures.

Following this nomenclature, our calculations show that the first 20 QNMs of the spherical NPoM ($w = 0$ nm), arranged in the order of ascending real eigenfrequencies, are $(lm) = (10), (11), (20), (21), (22), (30), (31), (32), (33), (40), (41), (42), (43), (50), (44), (51), (52), (53), (60), (54)$, respectively. The results demonstrate two key features. Firstly, QNMs of the same ℓ have higher eigenfrequencies with increasing m. Secondly, the QNMs with different ℓ do not spectrally overlap for the first 13 QNMs.

However, the above features are not followed by faceted NPoMs with $w > 0$. As the facet width increases, the order of QNMs with different ℓ become mixed, and those with larger m tend to lie at lower eigenfrequencies. For example, the first 20 QNMs of a faceted NPoM with $w = 20$ nm are $(lm) = (10), (11), (22), (20), (33), (21), (30), (44), (32), (31), (55), (40), (43), (66), (41), (42), (54), (77), (50), (51)$, respectively, see Table 2.1 for the full list of the QNMs of NPoMs with $w = 0$ - 40 nm. As facet width increases

from 0 to 20 nm, the field confinement also becomes dispersed throughout the facet as shown in Figs. 2.2(d,e) and 2.3(f-j) for $w = 20$ nm NPoM. Nonetheless, the symmetries of these QNMs are preserved for all facet widths, validating the nomenclature used in this chapter.

w (nm)	(ℓm)
0	10, 11, 20, 21, 22, 30, 31, 32, 33, 40, 41, 42, 43, 50, 44, 51, 52, 53, 60, 54
5	10, 11, 20, 21, 22, 30, 31, 32, 33, 40, 41, 42, 43, 44, 51, 50, 54, 61, 52, 55
10	10, 11, 20, 22, 21, 30, 33, 31, 32, 40, 44, 41, 43, 42, 50, 55, 51, 54, 66, 52
15	10, 11, 20, 22, 21, 33, 30, 31, 44, 32, 40, 55, 41, 43, 42, 50, 66, 51, 54, 53
20	10, 11, 22, 20, 33, 21, 30, 44, 32, 31, 55, 40, 43, 66, 41, 42, 54, 77, 50, 51
25	10, 11, 22, 20, 33, 21, 44, 30, 32, 55, 31, 66, 43, 40, 54, 41, 42, 77, 50, 88
30	11, 10, 22, 20, 33, 21, 44, 32, 30, 55, 66, 43, 31, 54, 40, 42, 77, 41, 88, 65
35	11, 10, 22, 20, 33, 21, 44, 32, 30, 55, 66, 43, 31, 54, 77, 42, 40, 88, 65, 41
40	11, 10, 22, 20, 33, 21, 44, 32, 30, 55, 66, 43, 31, 54, 77, 42, 40, 88, 65, 53

Table 2.1: The list of QNMs shown in ascending order of real eigenfrequencies $\omega_{\ell m} = \mathrm{Re}[\widetilde{\omega}_{\ell m}]$ for NPoMs with facet widths w from 0 to 40 nm. Here, the QNMs with negative m are neglected since QNMs with $m = \pm n$ are degenerate for $n \in \mathbb{Z}^+$.

The previous studies on NPoMs which were based on the scattering approach [64–67] identified the $(\ell 0)$ and $(\ell 1)$ QNMs. The $(\ell 0)$ QNMs are bright and can be efficiently excited by the vertical component of an exciting plane wave. The $(\ell 1)$ QNMs, though much darker than the $(\ell 0)$, can be efficiently isolated by exciting an NPoM with either a horizontally polarized plane wave or two vertically polarized out-of-phase plane waves propagating along opposite directions [40]. On the other hand, higher QNMs with $|m| > 1$, such as (22) and (33), have not been reported in the literature. These higher-order QNMs can not be easily isolated since they are very weakly coupled to external fields and are spectrally overlapping with each other. Hence, they have so far hidden in combination with each other, distorting and complicating previous analyses.

2.6.2 QNM Eigenfrequencies

In order to understand the optical behaviours of gap plasmonic resonances created by faceted NPoM cavities, it is useful to consider the high-order gap plasmonic resonances in the infinite frequency limit $\omega_{\ell m} \to \infty$, i.e. $\lambda_{\ell m} \to 0$. In this limit, the resonances no longer see the nanoparticle, and the system can simply be treated as a metal-insulator-

metal (MIM) plasmonic waveguide [65, 82]. The complex eigenfrequencies of the waveguide $\widetilde{\omega}_{MIM} = \omega_{MIM} - i\kappa_{MIM}$ can be calculated by solving the semi-analytical parametric equation [13].

$$\tanh\left(d\sqrt{\beta^2 - (\widetilde{\omega}_{MIM}/c)^2\ \epsilon_{gap}}\right) = -\frac{\epsilon_{gap}\sqrt{\beta^2 - (\widetilde{\omega}_{MIM}/c)^2\ \epsilon_{Au}(\widetilde{\omega}_{MIM})}}{\epsilon_{Au}(\widetilde{\omega}_{MIM})\sqrt{\beta^2 - (\widetilde{\omega}_{MIM}/c)^2\ \epsilon_{gap}}} \tag{2.17}$$

subject to the wavevector parameter β whereas $d = 1$ nm is the gap thickness, $\epsilon_{gap} = n_{gap}^2$ is the gap permittivity and $\epsilon_{Au}(\widetilde{\omega})$ is the gold permittivity. We note that the MIM plasmonic waveguide also has another set of solutions with the opposite parity to Eq. (2.17). However, these solutions have zero E_z field components at the gap center and do not correspond gap plasmons.

Fig. 2.4(a-c) investigates the spectral correlations between the QNMs on complex eigenfrequency planes. We plot with a dashed line the solution of Eq. (2.17), which corresponds to the waveguide eigenfrequencies $\widetilde{\omega}_{MIM}$, as well as the resonant frequencies $\widetilde{\omega}_{\ell m}$ of the NPoMs. For all facet widths, all QNMs with $m > 0$ lie close to the dashed line of $\widetilde{\omega}_{\ell m}$. As w increases, the QNMs with $m > 0$ simply migrate along $\widetilde{\omega}_{MIM}$ to lower real-eigenfrequencies. Since the imaginary eigenfrequencies $\kappa_{\ell m}$ represent the energy dissipation of the QNMs, these results demonstrate that those with $\widetilde{\omega}_{\ell m}$ lying along $\widetilde{\omega}_{MIM}$ are dark modes, and their energies are dissipated almost exclusively through heat at the rate κ_{MIM}. Only the (ℓ0) QNMs are efficiently radiative and lie significantly above $\widetilde{\omega}_{MIM}$ because their charge distributions have non-zero electric dipole moments and are therefore unlike the modes predicted by the MIM model. This implies that the difference between $\kappa_{\ell o}$ and κ_{MIM} correspond to energy dissipation through far-field radiation (shown as blue arrows in Fig. 2.4(a-c)).

To visualize how the QNMs evolve with varying facet width w, Fig. 2.4(d) plots real eigenfrequencies $\omega_{\ell m}$ of all QNMs of NPoMs with facet width w between 0 and 40 nm. Most QNMs red-shift with increasing w. There are a few exceptions such as the (10) QNMs which start at $w = 0$ nm as the lowest eigenfrequency QNM and then level off beyond $w > 25$ nm. The QNMs with larger m generally red-shift at more rapid rates. For example, the (11) QNM appears at lower frequency than the (10) QNM for facet sizes around $w = 25$ nm, and the (22) QNM becomes more energetically favorable

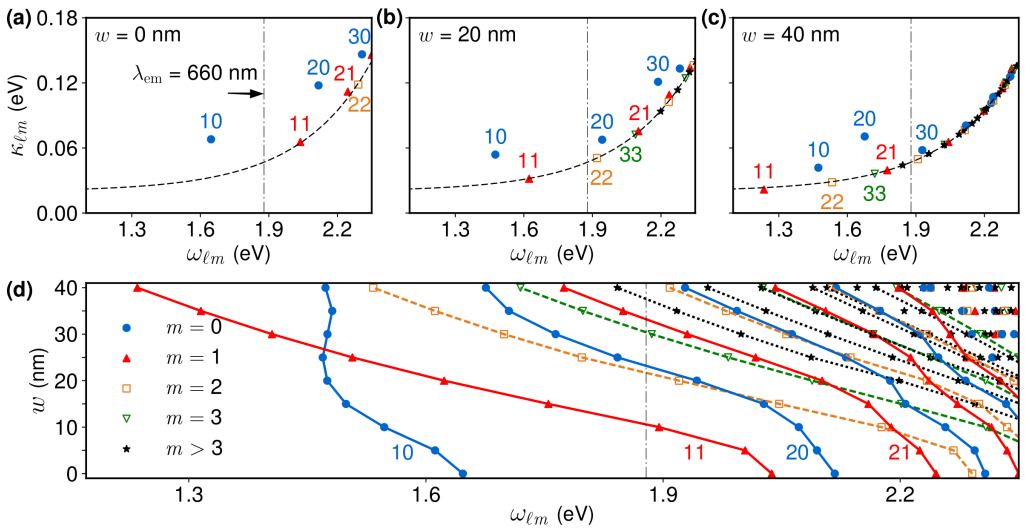

Figure 2.4: FEM simulations using QNMEig for the QNM complex eigenfrequencies $\tilde{\omega}_{\ell m} = \omega_{\ell m} - i\kappa_{\ell m}$ of NPoMs with facet widths (a) $w = 0$ nm, (b) $w = 20$ nm and (c) $w = 40$ nm. The QNMs with $m = 0$, 1, 2 and 3 are shown as blue circles, red triangles, orange squares and green inverted triangles, respectively, whereas $m > 3$ QNMs are shown as black stars. The dashed lines correspond to the complex eigenfrequencies $\tilde{\omega}_{MIM}$ of the MIM plasmonic waveguide whereas the dash-dotted vertical lines indicate the emitter wavelength $\lambda_{em} = 660$ nm (1.88 eV) which is considered in Figs. 2.8 and 2.9. The blue arrows indicate the radiative ($\ell 0$) QNMs. (d) The real eigenfrequencies ω_i for $w = 0 - 40$ nm. The fitted lines connect the QNMs with the same labels.

than the (21) and (20) QNMs for facet sizes $w = 10$ and 15 nm, respectively. These results demonstrate complicated spectral relations between bright and dark resonances of NPoMs with different facet widths, leading to vastly different near- and far-field optical behaviors.

To further explore the radiative nature of each QNM, we estimate the radiation efficiency of the (ℓm) QNM as

$$\eta_{\ell m} = \frac{\kappa_{\ell m} - \kappa_{MIM}}{\kappa_{\ell m}} = 1 - \frac{\kappa_{MIM}}{\kappa_{\ell m}}. \tag{2.18}$$

Figure 2.5 shows the radiation efficiencies of (10), (20), (30), (40), (11), (21), (31), (41), (22) and (33) QNMs. Overall, the ($\ell 0$) QNMs are the dominant radiative channels of NPoMs, as one would expect. The (10) QNM has the highest efficiency for a wide range w and is only overtaken by the (20) QNM for $w > 35$ nm. As ℓ increases, the ($\ell 0$) QNMs becomes less radiative at $w = 0$ nm but show complex behaviors near $w = 20$ nm. The ($\ell 1$) QNMs also have non-negligible but small radiation efficiencies below 0.1. In fact, these ($\ell 1$) QNMs take an essential part in determining the far-field emission, as later shown in

Figs. 2.8 and 2.9. On the other hand, the modes with $m > 1$ are virtually dark, and their radiation efficiencies are close to zero. We note that the efficiencies of some QNMs, such as the (11) and (22) QNMs, fall below zero at large facet width. This is because the MIM plasmonic waveguide represents the NPoM system phenomenologically and, hence, only provides an approximate description.

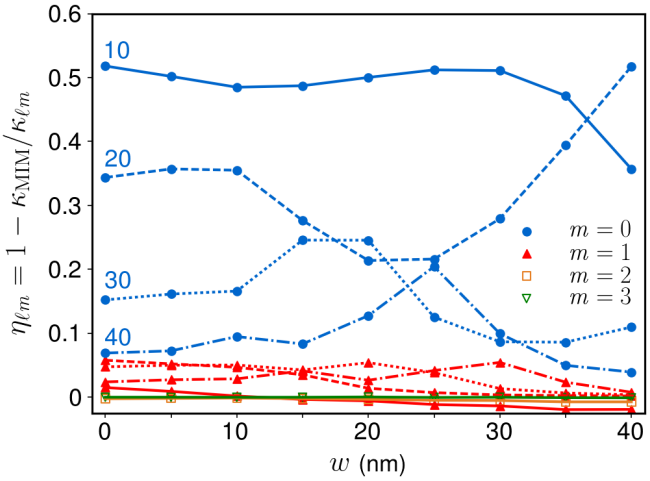

Figure 2.5: Radiation efficiencies $\eta_{\ell m}$ of (10), (20), (30), (40), (11), (21), (31), (41), (22) and (33) QNMs of NPoMs with facet width from 0 to 40 nm. The (ℓ0), (ℓ1), (22) and (33) QNMs are shown as blue, red, orange and green lines, respectively. The (ℓ0) and (ℓ1) QNMs are also further distinguished by solid lines for $\ell = 1$, dashed lines for $\ell = 2$, dotted lines for $\ell = 3$ and dashed-dotted lines for $\ell = 4$.

2.7 FAR-FIELD EMISSION OF QNMS

The previous section investigates the near-field profiles and eigenfrequencies of the QNMs of NPoMs. We are now well positioned to examine their far-field properties. Another open-source program RETOP [56] is used to project the electromagnetic fields of each QNM in the near-field zone, $(\widetilde{\mathbf{E}}_{\ell m}, \widetilde{\mathbf{H}}_{\ell m})$, to the far-field, $(\widetilde{\mathbf{E}}^{\mathrm{ff}}_{\ell m}, \widetilde{\mathbf{H}}^{\mathrm{ff}}_{\ell m}) \exp(\mathrm{i} k_{\mathrm{i}} R_{\mathrm{u}})$ where $k_{\mathrm{i}} = \omega_{\ell m}/c$, on the upper hemisphere of radius R_{u} above the NPoMs. The time-average Poynting flux of each QNM, $\langle S_{\ell m} \rangle = \mathrm{Re}[(\widetilde{\mathbf{E}}^{\mathrm{ff}}_{\ell m})^* \times \widetilde{\mathbf{H}}^{\mathrm{ff}}_{\ell m}]/2$, is then evaluated and shown in Fig. 2.6. The bright (ℓ0) QNMs show ring-shaped emission patterns with emission peaks near angle $\theta = 60^\circ$ while the darker (ℓ1) QNMs show spot-shaped emission, peaked at $\theta = 0^\circ$. These results are consistent with the far-field results reported

in Ref. [83] for a cuboid NPoM structure, see Fig. 2.7. The (22) QNMs in Fig. 2.6(e,h) shows far-field emission with four emission peaks, having the same symmetry as their near-field profiles in Fig. 2.3(e,h). On the other hand, the (33) QNM in Fig. 2.6(j) shows spot-shaped emission, similar to those of the (ℓ1) QNMs.

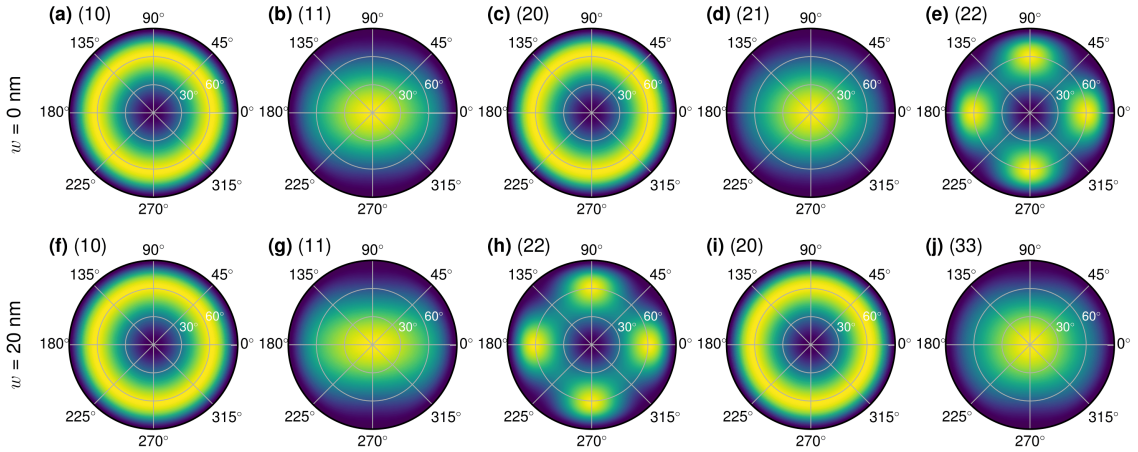

Figure 2.6: FEM simulations using QNMEig and RETOP for the Poynting fluxes $\langle S_{\ell m} \rangle$ (normalized between 0 and 1). The results for the first five QNMs are shown on the top hemisphere above NPoMs with (a-e) $w = 0$ nm and (f-j) $w = 20$ nm.

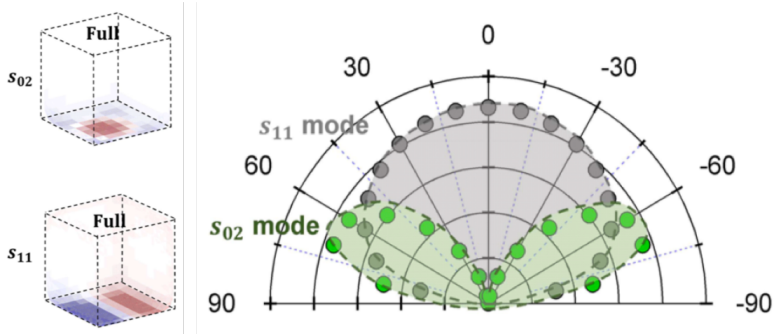

Figure 2.7: Surface charge distributions (left) and far-field emission profiles (right) from the even (s_{02}) and odd (s_{11}) resonances of a cuboid NPoM, adapted with permission from Ref. [83]. Copyright (2017) American Chemical Society.

2.8 QNM COUPLING TO AN EMITTER

Although it is indeed essential to understand how each QNM radiates to the far-field, individual QNMs are rarely excited in isolation. Hence, accurate far-field analysis of an NPoM must involve recombining QNM far-field emission. In this section, the

coupling coefficients of an electric dipole emitter placed inside an NPoM to the QNMs are evaluated and used to calculate the total far-field emission of the dipole emitter.

For a single emitter with a transition frequency ω placed at position $\mathbf{r}_{em}$ in close proximity to a plasmonic structure, the electromagnetic fields $(\mathbf{E},\mathbf{H})$ radiated by the emitter can be expanded to a small set of QNMs [79]

$$\mathbf{E}(\mathbf{r}) = \sum_i \alpha_i(\mathbf{r}_{em};\omega)\widetilde{\mathbf{E}}_i(\mathbf{r}). \tag{2.19}$$

where $\alpha_i(\mathbf{r}_{em};\omega)$ is the modal excitation coefficient. Inserting the fields from the dipole $(\mathbf{H}_1 = \mathbf{H}, \mathbf{E}_1 = \mathbf{E}, \omega_1 = \omega, \mathbf{J}_1 = -i\omega\mu\delta(\mathbf{r}-\mathbf{r}_{em}))$ and the m^{th} QNM solution $(\mathbf{H}_2 = \widetilde{\mathbf{H}}_i, \mathbf{E}_2 = \widetilde{\mathbf{E}}_i, \omega_2 = \widetilde{\omega}_i, \mathbf{J}_2 = 0)$ into Eq. (2.12), we obtain

$$\sum_j B_{i,j}(\omega)\alpha_j(\mathbf{r}_{em};\omega) = -\omega\boldsymbol{\mu}\cdot\widetilde{\mathbf{E}}_i(\mathbf{r}_{em}) \tag{2.20}$$

$$B_{i,j}(\omega) = \iiint \left\{\widetilde{\mathbf{E}}_j\cdot[\omega\varepsilon(\mathbf{r};\omega) - \widetilde{\omega}_i\varepsilon(\mathbf{r};\widetilde{\omega}_i)]\widetilde{\mathbf{E}}_i - \mu_0\widetilde{\mathbf{H}}_j\cdot(\omega-\widetilde{\omega}_i)\widetilde{\mathbf{H}}_i\right\} d\mathbf{r}^3 \tag{2.21}$$

where $\boldsymbol{\mu}$ is the dipole moment. The QNM excitation coefficients α_i can be found by finding the inverse of the QNM dipole coupling operator $B_{i,j}$

$$\alpha_i(\mathbf{r}_{em};\omega) = -\omega\sum_j B^{-1}_{i,j}(\omega)\boldsymbol{\mu}\cdot\widetilde{\mathbf{E}}_j(\mathbf{r}_{em}). \tag{2.22}$$

In the special case where the i-th QNM is spectrally isolated from other QNMs and $\omega \approx \omega_i$, Eqs. (2.21), (2.22) and (2.19) can be simplified as

$$B_{ii}(\omega) \approx \omega - \widetilde{\omega}_i \tag{2.23}$$

$$\alpha_i(\mathbf{r}_{em};\omega) \approx -\frac{\omega\boldsymbol{\mu}\cdot\widetilde{\mathbf{E}}_i(\mathbf{r}_{em})}{\omega-\widetilde{\omega}_i} \tag{2.24}$$

$$\mathbf{E}(\mathbf{r}) \approx -\frac{\omega\boldsymbol{\mu}\cdot\widetilde{\mathbf{E}}_i(\mathbf{r}_{em})}{\omega-\widetilde{\omega}_i}\widetilde{\mathbf{E}}_i(\mathbf{r}). \tag{2.25}$$

For a plasmonic structure, this result shows how a plasmonic QNM is excited by a dipole. However, the QNM excited by the dipole can in turn re-excite the dipole which

then further excites the QNM. This interaction between light and matter is discussed in the next section.

2.8.1 Purcell Enhancement

The Purcell factor can also be evaluated using the QNM method presented in the previous section. By expressing the total field $\mathbf{E}$ as a linear combination of normalized QNM fields $\widetilde{\mathbf{E}}_i(\mathbf{r})$ as in Eq. (2.19) and inserting it into Eq. (1.12), the enhanced decay rate is given as

$$\gamma_{tot}(\mathbf{r}_{em},\omega) = \frac{2}{\hbar}\mathrm{Im}\left[\boldsymbol{\mu}^* \cdot \sum_i \alpha_i(\mathbf{r}_{em};\omega)\widetilde{\mathbf{E}}_i(\mathbf{r})\right]. \tag{2.26}$$

In the case where the emitter's frequency is close to the i-th QNM's frequency $\omega \approx \omega_i$, Eq. (2.25) can be used to derive Purcell factor of the i-th QNM [79]

$$V_i(\mathbf{r}_{em}) = \frac{1}{2\varepsilon_0\varepsilon_B[\widetilde{\mathbf{E}}_i(\mathbf{r}_{em})\cdot\hat{\mathbf{e}}_\mu]^2} \tag{2.27}$$

$$F_i(\mathbf{r}_{em};\omega) = \frac{3}{4\pi^2}\left(\frac{\lambda_i}{n_B}\right)^3 \mathrm{Im}\left[\frac{Q}{V_i(\mathbf{r}_{em})}\frac{\omega_i^2\kappa_i}{\omega^2(\widetilde{\omega}_i-\omega)}\right] \tag{2.28}$$

where $\hat{\mathbf{e}}_\mu = \boldsymbol{\mu}/|\boldsymbol{\mu}|$ is the dipole moment unit vector and $Q = \omega_i/2\kappa_i$ is the quality factor. V_i is the local mode volume which defines the field confinement locally experienced by the emitter. At $\omega = \omega_i$, $\omega_i^2\kappa_i/\omega^2(\widetilde{\omega}_i-\omega) = i$, and the expression reduces to

$$F_i(\mathbf{r}_{em};\omega_i) = \frac{3}{4\pi^2}\left(\frac{\lambda_i}{n_B}\right)^3 \mathrm{Re}\left[\frac{Q}{V_i(\mathbf{r}_{em})}\right]. \tag{2.29}$$

For a closed cavity with $-\mathrm{Im}[\widetilde{\omega}_i] = \kappa_i \to 0$, the mode volume becomes a real number $V_i = \mathrm{Re}[V_i]$. The Purcell factor can then be simplified into its original expression derived by Purcell in Eq. (1.14)

$$F_i(\mathbf{r}_{em};\omega_i) = \frac{3}{4\pi^2}\left(\frac{\lambda_i}{n_B}\right)^3 \frac{Q}{V_i(\mathbf{r}_{em})} \tag{2.30}$$

where the total Purcell factor is $F = 1 + F_i$.

2.9 OPTICAL EMISSION FROM AN NPOM NANOGAP

Here, a methylene blue with transition wavelength of $\lambda_{em} = 660$ nm is chosen as a quantum emitter of choice since it is a typical dye molecule experimentally used inside an NPoM [24]. By placing the emitter with $\boldsymbol{\mu} = |\boldsymbol{\mu}|\hat{\mathbf{e}}_z$ at position x_{em} in the gap of an NPoM, its coupling to the NPoM's QNMs in Eq. (2.22) can be simplified to

$$\alpha_{\ell m}(x_{em};\omega_{em})/|\boldsymbol{\mu}| = -\omega_{em}\sum_{\ell' m'} B^{-1}_{\ell m,\ell' m'}(\omega_{em})\widetilde{E}_{z,\ell' m'}(x_{em}) \tag{2.31}$$

where $\widetilde{E}_{z,i} = \hat{\mathbf{e}}_z \cdot \widetilde{\mathbf{E}}_i$, $\omega_{em} = 2\pi c/\lambda_{em}$, and only the first 20 QNMs are included in the calculations, see Table 2.1. The coupling coefficient magnitude $|\alpha_{\ell m}|$ to different (ℓm) QNMs are shown in Fig. 2.8. Four QNMs with even m, Fig. 2.8(a,c), are separated from those with odd m, Fig. 2.8(b,d), as they have symmetric and antisymmetric field profiles across the $x = 0$ nm plane, respectively. For $w = 0$ nm, the emitter's resonance lies spectrally close to the (10), (11) and (20), see Fig. 2.4(a). In 2.8(a,b), the coupling magnitudes of these three QNMs indeed dominate the coupling with the emitter. The coupling magnitudes of different QNMs change drastically when the facet width increases to $w =$ 20 nm. The emitter instead lies spectrally close to (11), (22), (20), (33) and (21) see Fig. 2.4(b), which become dominant QNMs coupling to the emitter, as shown in Fig. 2.8(c,d). The relative magnitudes of $|\alpha_{\ell m}|$ are crucial in understanding the total far-field emission.

The total far-field emission $(\widetilde{\mathbf{E}}^{ff}, \widetilde{\mathbf{H}}^{ff})$ from the emitter placed inside an NPoM can then be evaluated by recombining the far-field QNM fields $(\widetilde{\mathbf{E}}^{ff}_{\ell m}, \widetilde{\mathbf{H}}^{ff}_{\ell m})$ with complex coupling coefficient $\alpha_{\ell m}$

$$(\widetilde{\mathbf{E}}^{ff}(x_{em};\omega_{em}), \widetilde{\mathbf{H}}^{ff}(x_{em};\omega_{em})) = \sum_{\ell m} \alpha_{\ell m}(x_{em};\omega_{em})(\widetilde{\mathbf{E}}^{ff}_{\ell m}, \widetilde{\mathbf{H}}^{ff}_{\ell m}). \tag{2.32}$$

Fig. 2.9 shows the total time-average Poynting flux $\langle S\rangle = \mathrm{Re}[(\widetilde{\mathbf{E}}^{ff})^* \times \widetilde{\mathbf{H}}^{ff}]/2$ from the emitter placed at lateral position $x_{em} = 0$, 5, 10 and 15 nm inside NPoMs with facet width $w = 0$ and 20 nm. For $w = 0$ nm, Fig. 2.9(a-d), the emission has a ring-shaped pattern at $x_{em} = 0$ nm as the emitter is dominantly coupled to the (10) and (20) QNMs. As x_{em} increases, the emitter couples less efficiently to the (10) and (20) QNMs while

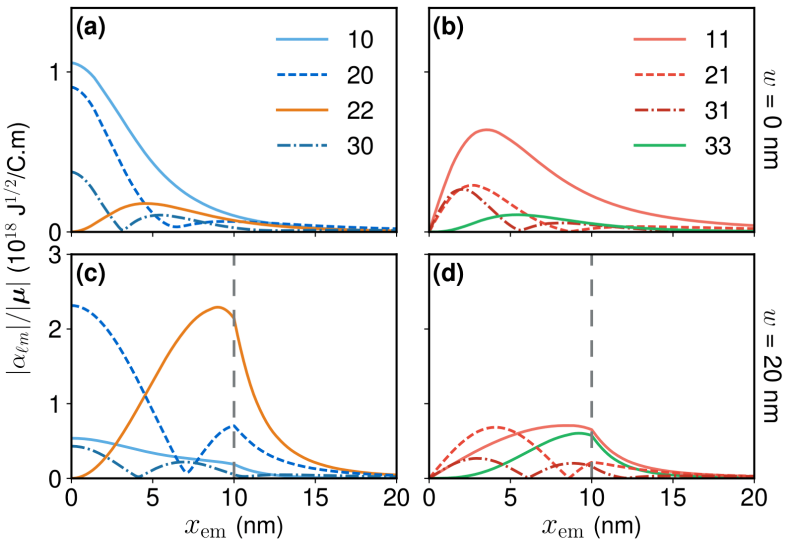

Figure 2.8: Coupling coefficient $\alpha_{\ell m}$ of an emitter with dipole moment $\boldsymbol{\mu}$ and transition wavelength $\lambda_{em} = 660$ nm to (a,c) the first four symmetric and (b,d) first four antisymmetric QNMs of NPoMs with facet widths (a,b) $w = 0$ nm and (c,d) $w = 20$ nm. The vertical dashed lines indicate the facet edges.

becoming more efficiently coupled to the (11). The spot-shaped emission from the (11) QNM also has a phase variation over the angular coordinate ϕ. At $x_{em} = 5$ nm, the distorted ring-shaped emission in Fig. 2.9(b) is the result of this phase variation, giving destructive interference for $-\pi/2 < \phi < \pi/2$ and constructive interference for $\pi/2 < \phi < 3\pi/2$ with the ring-shaped emission from the (10) and (20). For large $x_{em} \geqslant 10$ nm, the antisymmetric (11) QNM dominates the coupling with the emitter, and the emission becomes offset spot-shaped patterns.

For $w = 20$ nm, the emission also starts as a ring-shaped pattern at $x_{em} = 0$ nm as the emitter couples mainly to the (20) QNM, as shown in Fig. 2.9(e). In a similar manner to Fig. 2.9(b), the emission at $x_{em} = 5$ nm in Fig. 2.9(f) then becomes a distorted ring-shaped pattern as the emitter couples more efficiently to the (11) and (21) QNMs. However, the emission from the emitter changes drastically for $x_{em} = 10$ nm as the emission flips 180°, as shown in Fig. 2.9(g). This flip results from the changes in the complex coefficients $\alpha_{\ell m}$ of different QNMs which, instead, interferes constructively for $-\pi/2 < \phi < \pi/2$ and destructively for $\pi/2 < \phi < 3\pi/2$. Unlike Fig. 2.9(d), the emission at $x_{em} > 15$ in 2.9(h) resumes the ring-shaped patterns as the emitter, instead, dominantly couples the symmetric (20) and (22) QNMs.

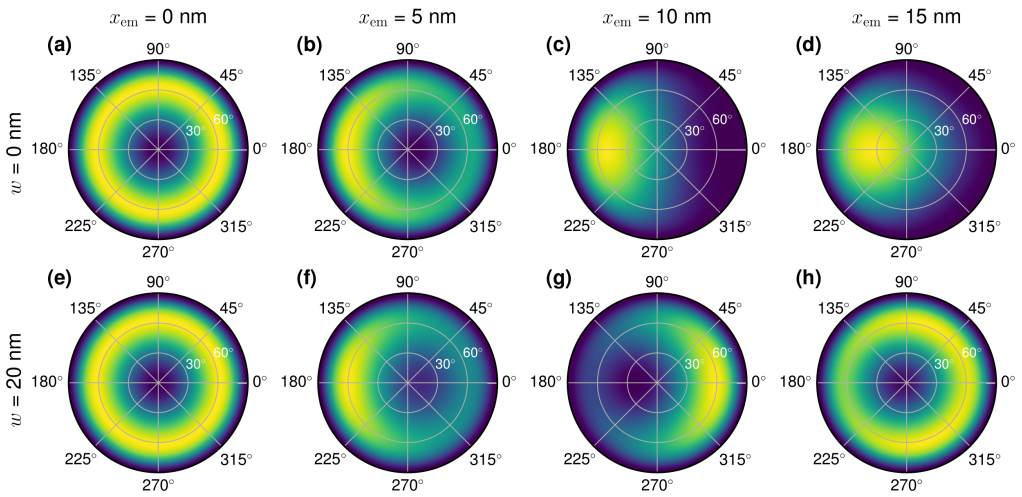

Figure 2.9: FEM simulations using QNMEig and RETOP for the Poynting fluxes $\langle S \rangle$ (normalized between 0 and 1). The results of the dipole emission are shown on the top hemispheres above NPoMs. Single emitters with transition wavelength $\lambda_{em} = 660$ nm are placed in the nanogap with facet width (a-d) 0 nm and (e-h) 20 nm at position (a, e) $x_{em} = 0$ nm, (b, f) $x_{em} = 5$ nm, (c, g) $x_{em} = 10$ nm and (d, h) $x_{em} = 15$ nm.

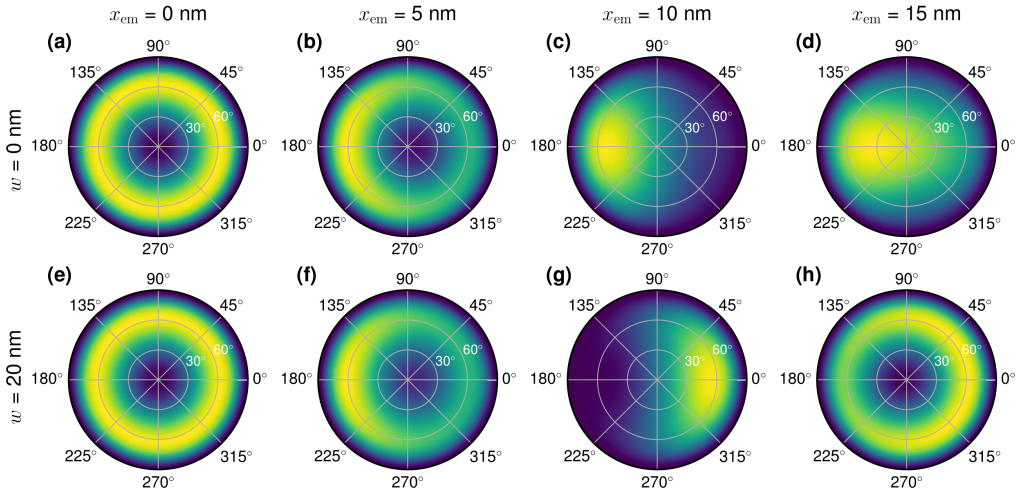

Figure 2.10: FEM simulations using the direct dipole method and RETOP for the Poynting fluxes $\langle S \rangle$ (normalized between 0 and 1). The results of the dipole emission are shown on the top hemispheres above NPoMs. All parameters are the same as those in Fig. 2.9.

The results in Fig. 2.9 are confirmed by almost identical results in Fig. 2.10. Instead of decomposing and recombining the QNMs, an electric dipole emitter is placed at the same lateral positions inside NPoMs with the same facet widths as in Fig. 2.9, and its near-field $(\mathbf{E}, \mathbf{H})$ is then projected to the far-field $(\mathbf{E}^{ff}, \mathbf{H}^{ff})$ by RETOP. It can be seen that $\langle S \rangle$ in Fig. 2.10(a,b,c,e,f,h) are virtually indistinguishable from those in Fig. 2.9(a,b,c,e,f,h). On the other hand, small differences can be observed between Figs.

2.9(d,g) and 2.10(d,g) which can be attributed to the termination at the first 20 QNMs in the calculations. Although the results obtained from the direct electric dipole method are indeed more accurate, those obtained from the QNM decomposition and recombination provide valuable information about the optical nature of an NPoM and aid our understanding on its complicated multi-modal interaction with a quantum emitter.

2.10 CONCLUSIONS

In recent years, the NPoM geometry has become a prominent nanostructure in nanoplasmonics due to its extreme light confinement properties. However, a comprehensive modal analysis of the structure had not been available, and most studies to date infer its resonances from its optical scattering. This chapter uses the QNM approach to analyze the morphology-dependent plasmonic resonances of an NPoM structure. A collection of bright and dark resonances are revealed, of which some had not been previously reported in the literature. The near-field and far-field optical behaviors of NPoMs with varying facet widths are reported, which clarifies the inconsistency in the previous near-field and far-field analyses. This study also unveils rich and intricate multi-modal interaction with a single quantum emitter and has the potential to aid forthcoming designs in quantum plasmonic experiments.

3 SUPPRESSED FLUORESCENCE QUENCHING AND STRONG-COUPLING

The results presented in this chapter have been published in Ref. [68] and Ref. [69], co-authored by A. Demetriadou, R. Chikkaraddy, F. Benz, V. A. Turek, U. F. Keyser, J. J. Baumberg and O. Hess. Some parts of this chapter are quoted verbatim from the published manuscripts.

I ran all of the numerical simulations and contributed to all of the figures. A. Demetriadou performed the analytic calculations in Fig. 3.1(d). R. Chikkaraddy conducted the measurements in Fig. 3.6 whereas V. A. Turek prepared the samples for the measurements. All authors contributed to the discussion of the content in this chapter.

3.1 INTRODUCTION

The lifetime of an excited atomic state is determined by the properties of the atom and its environment, first theoretically suggested by Purcell [1] and followed by experimental demonstration by Goy, Haimond, Gross, and Haroche [84]. Subsequent experiments further verified this by placing atomic emitters within various optical-field-enhancing geometries [2, 85–87]. Plasmonic structures have the ability to massively enhance electromagnetic fields, and therefore dramatically alter the excitation rate of an emitter [14]. However, it is well known that, placing an emitter close to an isolated plasmonic nanostructure (< 10 nm), quenches its fluorescence [88–95]. Analysis by Anger, Bharadwaj, and Novotny [14] showed this is due to the coupling of the emitter to non-radiative higher-order plasmonic modes that dissipate its energy. This 'zone of fluorescence inactivity' was previously believed to quench all quantum emitters.

However, recent advancements have shown that an emitter's emission rate can be enhanced with plasmonic nano-antennas [96–103], which efficiently convert far-field ra-

diation into a localized field and vice versa. As first theoretically explained by Jun, Kekatpure, White, and Brongersma [104], a single emitter placed into near-contact with a plasmonic nano-antenna can efficiently couple with the antenna's plasmonic modes and overcomes quenching [105, 106]. This was experimentally demonstrated by Hoang, Akselrod, and Mikkelsen [103] who showed that a quantum dot in a 12 nm nano-gap exhibits ultra-fast spontaneous emission. What however remains unclear is if this enhanced emission is strong enough to allow for single emitter strong-coupling with plasmons.

This chapter demonstrates and explains why fluorescence quenching is substantially suppressed in plasmonic nanocavities, to such a degree that can indeed facilitate light-matter strong-coupling of a single-molecule at room temperature as it was recently demonstrated experimentally [24, 25]. This is due to: (i) the dramatic increase in the emitter excitation (similar to plasmonic antennas), and (ii) the changed nature of higher-order modes that acquire a radiative component, and therefore increase the quantum yield of the system. Modes in plasmonic nanocavities are not simple superpositions of modes from isolated structuresi9, but instead are hybrid-plasmonic states [107–111]. Hence, higher-order modes that are dark for an isolated spherical nanoparticle, radiate efficiently for tightly-coupled plasmonic structures [82, 83], significantly enhancing the radiative decay and suppressing fluorescence quenching. By comparing an isolated nanoparticle with an NPoM nanocavity with and without facets, this chapter quantifies their different radiative and non-radiative channels, explaining the mechanism that leads to suppression of quenching in plasmonic nanocavities. Our theoretical predictions are then experimentally verified by our collaborators from University of Cambridge using DNA-origami to control the position of a single emitter in the nanogap [68]. A full time-domain Maxwell-Bloch approach finally allows us to directly contrast through 3D Finite-Difference Time-Domain (FDTD) simulations the (spatiotemporal) dynamics of single quantum emitters in both the nanoparticle and NPoM cases and in weak- and strong-coupling.

3.2 FLUORESCENCE ENHANCEMENT AND QUENCHING

3.2.1 Fluorescence Enhancement

Fluorescence emission of a quantum emitter is a two-step process involving its excitation and relaxation decay. This chapter assumes that the excitation rate γ_{exc} of the emitter is much slower than its total decay rate γ_{tot}. In this weak excitation regime, the excited emitter decays to its ground state before the next excitation event, and the fluorescence emission is limited by the excitation rate. However, not all of the excitation events are converted into the far-field fluorescence emission due to the emitter's internal and external dissipative processes. The conversion efficiency from excitation to fluorescence emission is defined by the quantum yield η, and, therefore, the fluorescence emission rate is given by [14]

$$\gamma_{em} = \gamma_{exc}\,\eta. \tag{3.1}$$

For an emitter located at position $\mathbf{r}_{em}$ with transition dipole moment $\boldsymbol{\mu}$ and transition frequency ω_{em}, its excitation rate γ_{exc} is determined by the local electric field $\mathbf{E}(\mathbf{r}_{em})$ in the direction of $\boldsymbol{\mu}$, $\gamma_{exc} \propto |\boldsymbol{\mu} \cdot \mathbf{E}(\mathbf{r}_{em})|^2$. In a vacuum, the emitter can only experience the incident field $\mathbf{E}_0(\mathbf{r}_{em})$ whereas, in non-vacuum, the emitter experiences the local field $\mathbf{E}(\mathbf{r}_{em})$ which is the combination of $\mathbf{E}_0(\mathbf{r}_{em})$ and its secondary field reflected from the environment. Let us represent the excitation enhancement through the normalized rate

$$\widetilde{\gamma}_{exc} = \frac{\gamma_{exc}}{\gamma^0_{exc}} = \left| \frac{\boldsymbol{\mu} \cdot \mathbf{E}(\mathbf{r}_{em})}{\boldsymbol{\mu} \cdot \mathbf{E}_0(\mathbf{r}_{em})} \right|^2 \tag{3.2}$$

where γ^0_{exc} is the excitation rate of the emitter in vacuum.

Each decay event either channels energy into far-field radiation or is dissipated in the environment. The quantum yield $\eta = \gamma_{rad}/\gamma_{tot}$ provides a measure of this behavior and is defined as the ratio between the far-field radiative decay rate γ_{rad} and the total decay rate γ_{tot} of the emitter. For a quantum emitter in vacuum, the radiative decay rate corresponds to the vacuum spontaneous decay rate $\gamma_{rad} = \gamma_0$, and the only dissipative

channel is the emitter's own internal loss γ_{int}. Hence, the vacuum quantum yield is defined as

$$\eta^0 = \frac{\gamma_0}{\gamma_0 + \gamma_{int}}. \tag{3.3}$$

When the emitter is placed in an optical environment, a decay event could also be absorbed by the surrounding environment. In the case of a plasmonic environment, the non-radiative decay rate γ_{nr} is predominantly determined by Ohmic losses [44]

$$\gamma_{nr} \propto \int_\Omega \mathrm{Re}\{\mathbf{J}_{em}(\mathbf{r}) \cdot \mathbf{E}^*_{em}(\mathbf{r})\}\, d\mathbf{r}^3 \tag{3.4}$$

where $\mathbf{J}_{em}$ is the induced current density within the volume Ω and $\mathbf{E}_{em}$ is the field emitted by the emitter. The quantum yield can then be defined by the total decay rate $\gamma_{tot} = \gamma_{rad} + \gamma_{nr} + \gamma_{int}$ as follows

$$\eta = \frac{\gamma_{rad}}{\gamma_{tot}} = \frac{\gamma_{rad}}{\gamma_{rad} + \gamma_{nr} + \gamma_{int}}. \tag{3.5}$$

We define the radiative and non-radiative decay enhancements as the emitter's decay rates normalized to its decay rate in vacuum γ_0 as $\widetilde{\gamma}_{rad} = \gamma_{rad}/\gamma_0$ and $\widetilde{\gamma}_{nr} = \gamma_{nr}/\gamma_0$ respectively. The fluorescence enhancement is similarly defined as

$$\widetilde{\gamma}_{em} = \frac{\gamma_{em}}{\gamma^0_{em}} = \widetilde{\gamma}_{exc} \frac{\eta}{\eta^0}, \tag{3.6}$$

where $\gamma^0_{em} = \gamma^0_{exc}\eta^0$ is the fluorescence rate of the emitter in vacuum.

3.2.2 Fluorescence Quenching

Eq. (3.6) implies that fluorescence emission of an emitter could either be enhanced or quenched by its environment depending on $\widetilde{\gamma}_{exc}$, η and η^0. In a plasmonic environment, for example, excitation $\widetilde{\gamma}_{exc}$ on an emitter could be drastically enhanced by intense plasmonic fields, but fluorescence emission could still be quenched through non-radiative decay channels.

Before we could continue with the discussion about fluorescence quenching, it is important to first define precisely what 'quenching' means. The term 'quenching' has several definitions in the literature. For example, Refs. [112, 113] define quenching as a reduction in the quantum yield (η) whereas Refs. [58, 114, 115] define quenching as non-radiative decay processes. However, this chapter defines 'fluorescence quenching' as 'a reduction in the fluorescence rate, with respect to the unperturbed emitter'. We also define that 'fluorescence is quenched' when the fluorescence enhancement $\widetilde{\gamma}_{em}$ approaches zero, and 'suppressing quenching' refers to any process that prevents $\widetilde{\gamma}_{em}$ from approaching zero.

There are also several fluorescence quenching processes, including chemical and electromagnetic quenching. Chemical quenching arise from molecular interaction such as molecular collision (dynamic quenching) [116, 117], ground-state complex formation (static quenching) [118], heating [119], electron transfer [120] and resonant energy transfer [91, 121]. These processes could be approximately described by the phenomenological internal loss γ_{int}. On the other hand, electromagnetic quenching arises from processes that could be described by Maxwell's equations, such as quenching through dark modes of a plasmonic structure.

This chapter mainly focuses electromagnetic quenching and neglects chemical quenching. In the following, unless otherwise stated, this chapter assumes that the emitter has no internal loss, $\gamma_{int} = 0$, $\gamma_{tot} = \gamma_{rad} + \gamma_{nr}$ and $\eta^0 = 1$. The rates γ_{exc}, γ_{rad} and γ_{tot} are calculated directly from FDTD simulations whereas γ_{nr} is evaluated indirectly from $\gamma_{nr} = \gamma_{tot} - \gamma_{rad}$.

3.3 FLUORESCENCE QUENCHING IN PLASMONICS

A plasmonic nanostructure provides an ideal environment for fluorescence enhancement as it substantially amplifies both γ_{exc} and γ_{tot} of an emitter by confining light to a sub-wavelength volume and therefore substantially amplifying the electromagnetic LDOS. However, the emitter in a plasmonic environment also experiences a large γ_{nr}

due to Ohmic losses, which reduces η. Because of these competing factors, a specific plasmonic nanostructure can either potentially enhance or quench fluorescence.

In the case of an isolated spherical nanoparticle, only its first-order dipolar mode is radiative (i.e. bright) and couples to the far-field whereas all higher-order modes are non-radiative (i.e. dark) and dissipate their energy through Ohmic losses [28]. When a quantum emitter is placed at a large distance ($z > 100$ nm) from the nanoparticle, it couples dominantly to the first-order plasmonic mode. As it approaches the nanoparticle, it couples more strongly to the first-order mode and fluorescence rate becomes drastically enhanced, as shown in Fig. 3.1(a). However as the emitter approaches closer than 10 nm from the nanoparticle, it couples increasingly to the dark higher-order modes, and its fluorescence is instead quenched via Ohmic losses. The results in Fig. 3.1(a) agree with previously reported results in Ref. [14] which suggests a zone of fluorescence inactivity at distance below 10 nm from a plasmonic nanostructure. However, this chapter will demonstrate that fluorescence quenching is not a general phenomenon in plasmonics, in contrast to the previously held belief, and can be suppressed in a plasmonic nanocavity.

3.4 SUPPRESSED QUENCHING IN SPHERICAL NANOCAVITIES

Similar calculations for the NPoM nanocavity with the emitter always in the center of the nanocavity, Fig. 3.1(b), reveal that the emission rate increases by several orders of magnitude (note the log-scale). As z decreases, the gap between nanoparticle and mirror reduces, and both plasmonic surfaces approach the emitter, but $\widetilde{\gamma}_{em}$ dramatically increases. Since the emission rate is a product of the excitation and radiative rates, they are presented separately in Fig. 3.1(c) and Fig. 3.2 for both an isolated nanoparticle and the nanocavity. As the emitter is progressively confined within the nanocavity, its excitation rate is enhanced, due to the very high confinement of the plasmon modes within the gap. Additionally, although the quantum yield (η) of the nanocavity still decreases, it out-performs that of the isolated nanoparticle by more than an order of magnitude as the gap decreases below 2 nm. While nonlocal effects can affect the quantitative rates

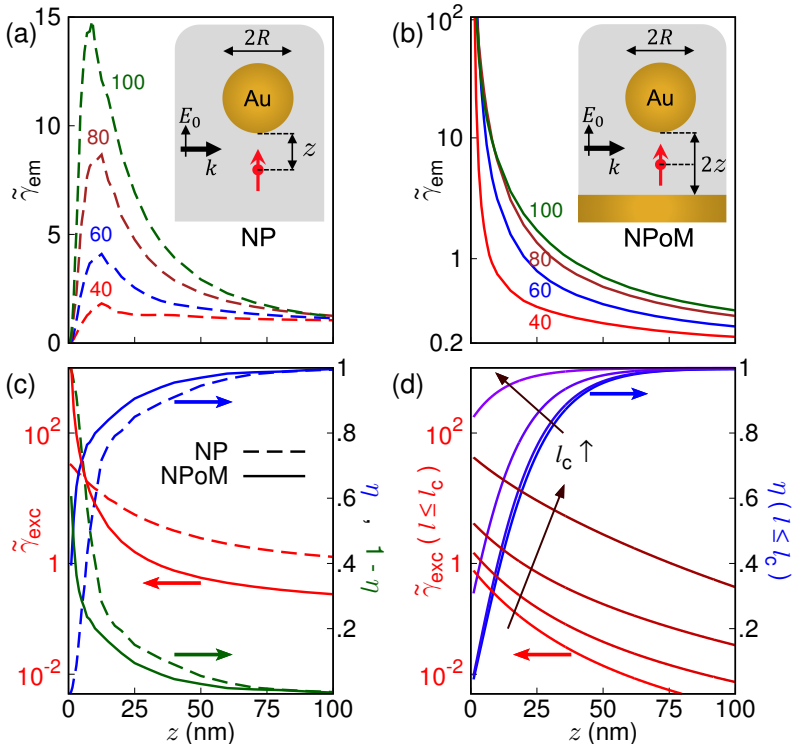

Figure 3.1: FDTD simulations for the fluorescence rate $\widetilde{\gamma}_{em}$ of an emitter with transition wavelength $\lambda_{em} = 650$ nm placed at distance z from (a) an isolated nanoparticle and (b) inside the NPoM nanocavity, for sphere diameters $2R = 40$, 60, 80 and 100 nm and with background permittivity $\epsilon_D = 1.96$. (c) The excitation rate $\widetilde{\gamma}_{exc}$ (red), quantum yield η (blue) and $1 - \eta$ (green) for an isolated nanoparticle (dashed lines) and a nanocavity (solid lines) of nanoparticle diameter 80 nm. (d) Coupling contributions to the excitation rate (red) and quantum yield (blue) when truncating the hybridization terms at $l_c = 2$, 3, 5 and 10. Reproduced with permission from Ref. [68]. Copyright (2017) American Chemical Society.

of emission, excitation, and quantum yield of both structures at sub-nm spacings, no qualitative change is expected on their behavior [122–124].

To illuminate the origin of these different behaviors, the analytical description of coupled plasmon modes [107, 108] is adapted. Isolated spherical nanoparticles are well described by Mie theory, but the problem of two coupled plasmonic nanoparticles is analytically more complex to determine. It has been solved in the quasi-static limit using several techniques, such as transformation optic [125–127] and multipole expansion [109–111, 128]. However, it is more appropriate to formulate the problem as the coupling of the bare plasmonic modes from the two structures. Adapting this description

for the NPoM (by approximating the mirror as a large sphere of radius $r_m = 1$ μm), the field enhancement in the middle of the nanocavity gap is given by [107]

$$\frac{E(r=0)}{E_0} \simeq \alpha^{NP}\left(\frac{R}{R+z}\right)^3 + \alpha^m\left[1+\sum_{l=2}^{\infty}\frac{\sqrt{\omega_1\omega_l}}{\omega_l-\omega-i\gamma/2}\left(\frac{l+1}{2}\right)^2\frac{R^{(2l+1)}}{(R+z)^{(l+2)}\,r_m^{l-1}}\right] \tag{3.7}$$

where R is the radius of the nanoparticle, 2z is the gap size assuming the emitter is in the middle of the gap, and $\omega_l = \omega_p\sqrt{l/(2l+1)}$ is the resonant frequency of mode l, with ω_p and γ the metal plasmon frequency and damping. The nanoparticle quasi-static polarizability $\alpha^{NP} = 2\frac{(\varepsilon_{Au}-1)}{(\varepsilon_{Au}+1)}$, while the mirror polarizability α^m is given by Mie scattering (beyond the quasi-static limit) in [129]. The first term provides the field enhancement contribution of the nanoparticle dipole mode, the first term in square brackets is the mirror dipole mode, and the second term in square brackets is the coupling of the mirror to the higher-order modes of the nanoparticle ($l \geqslant 2$).

Figure 3.1(d) plots this latter contribution of the coupling terms in equation (3.7) to the excitation rate (red lines) which converges at an increasing truncated number of modes (l_c). As the nanocavity gets smaller ($z \downarrow$), higher-order mode hybridization is needed to account for the dramatic increase of the NPoM excitation rate, as seen in Fig. 3.1(c). By following the method described in Ref. [108], radiative and non-radiative powers of the system can be calculated and then used to evaluate the quantum yield. Similar to the excitation rate, the quantum yield increases with increasingly higher-order hybridization between the two structures. Both of these observations demonstrate that the mode hybridization of the coupled plasmonic structures forming the nanocavity alter the fluorescence rate of an emitter in a way that suppresses quenching.

To further explore the suppression of quenching, Fig. 3.2(a) shows the excitation and quantum yield for an emitter placed $0 \leqslant z \leqslant 25$ nm from an isolated nanoparticle and the NPoM nano-cavity. Note that as z decreases, the gap of the NPoM becomes smaller and both metal surfaces approach the emitter. Fig. 3.2(a) shows more clearly than Fig. 1(c) the different behavior of the two structures for small values of z. Fig. 3.2(b) shows the excitation rate $\widetilde{\gamma}_{exc}$, and the radiative $\widetilde{\gamma}_{rad}$ and non-radiative $\widetilde{\gamma}_{nr}$ decay rates for the two structures. For the isolated nanoparticle, $\widetilde{\gamma}_{nr}$ exponentially increases as one approaches the metal surface and actually overtakes $\widetilde{\gamma}_{rad}$ at $z \sim 10$ nm. Hence, even though the

excitation continues to increase for $z < 10$ nm, most of the emitter's energy is coupled into non-radiative channels, quenching it. For the NPoM both $\widetilde{\gamma}_{rad}$ and $\widetilde{\gamma}_{nr}$ dramatically increase, and although $\widetilde{\gamma}_{nr}$ increases more rapidly, it reaches comparable values to $\widetilde{\gamma}_{rad}$ for $z < 1.5$ nm. This means that an emitter's energy and its enhanced excitation is coupled equally into both radiative and non-radiative channels. These are in fact the perfect conditions to facilitate the strong-coupling of the emitter with the plasmons.

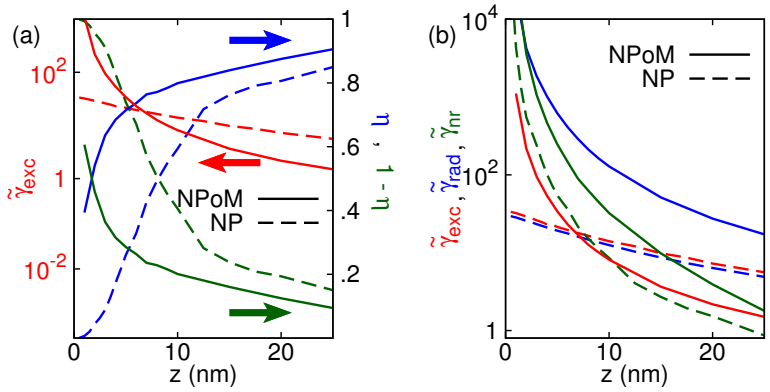

Figure 3.2: FDTD simulations for (a) the excitation rate $\widetilde{\gamma}_{exc}$ (red) and quantum yield η (blue) for an isolated nanoparticle (dotted lines) and a nanocavity (solid lines) of nanoparticle diameter 80 nm and an emitter placed at $0 \leqslant z \leqslant 25$ nm. (b) The radiative $\widetilde{\gamma}_{rad}$ and non-radiative decay rates $\widetilde{\gamma}_{nr}$, and excitation rate $\widetilde{\gamma}_{exc}$ (red) for both an isolated nanoparticle and the NPoM. Reproduced with permission from Ref. [68]. Copyright (2017) American Chemical Society.

The spectral dependence of the radiative, total, and excitation rates for both the isolated nanoparticle and the nanocavity, varying the nanoparticle diameter from 20 nm to 100 nm, show strongly contrasting behavior in Fig. 3.3. Again, the emitter is 0.5 nm from the Au surfaces or at the center of the 1 nm gap. Isolated quasi-static nanoparticles (with $2R < 100$ nm) possess diameter-independent modes as shown in Fig. 3.3(a,c,e). However, Fig. 3.3(b,d,f) shows that the resonant wavelengths of the nanocavity modes are highly dependent on the system geometry [65, 82]. The NPoM radiative decay rate $\widetilde{\gamma}_{rad} = \gamma_{rad}/\gamma_0$, normalized to the vacuum decay rate γ_0, is three orders of magnitude larger than for the isolated NP, with the NPoM dipole ($l = 1$) mode significantly red-shifting for larger nanoparticles. Additionally the quadrupole NPoM mode ($l = 2$) strongly radiates and for larger nanoparticles has comparable radiative rates to the dipole ($l = 1$) mode, in contrast with the isolated NP. These large $\widetilde{\gamma}_{rad}$ suppress quenching and allow strong-coupling dynamics to be radiated into the far-field.

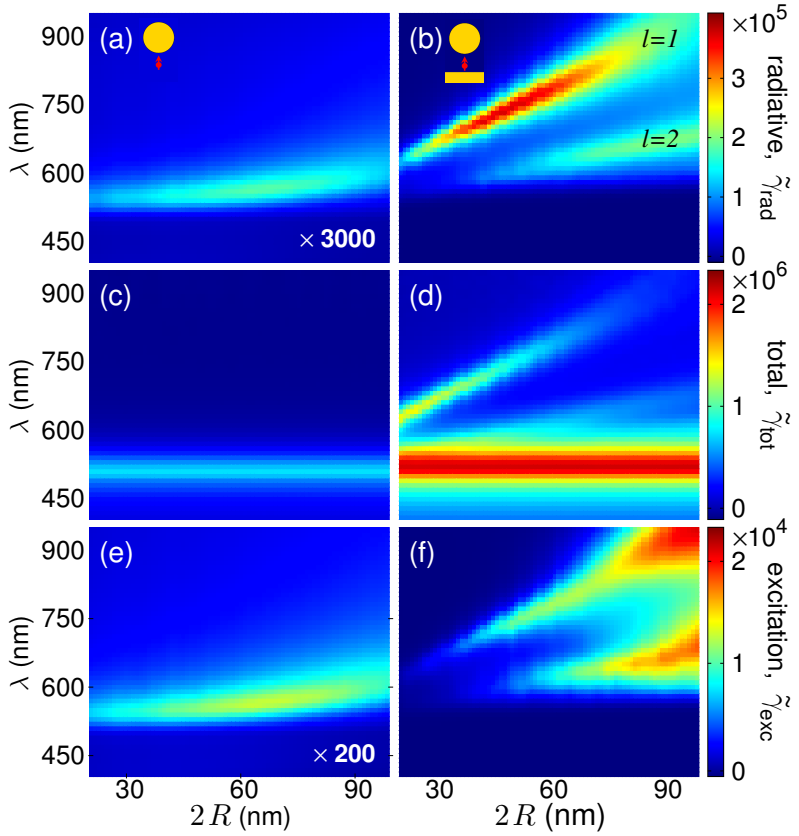

Figure 3.3: FDTD simulations for spectra of a vertically-oriented emitter placed (a,c,e) 0.5 nm below an isolated NP, and (b,d,f) inside a 1 nm-wide NPoM nanocavity. (a,b) Normalized radiative decay rate $\widetilde{\gamma}_r$, (c,d) Normalized total decay rate $\widetilde{\gamma}_{tot}$ (Purcell factor), and (e,f) Normalized excitation rate $\widetilde{\gamma}_{exc}$ (using the same incident light as Fig. 3.1). Reproduced with permission from Ref. [68]. Copyright (2017) American Chemical Society.

The Purcell factor (normalized total decay rate $\widetilde{\gamma}_{tot} = \gamma_{tot}/\gamma_0$) for both plasmonic structures shows a diameter-independent broad peak at $\lambda_{pm} \simeq 510$ nm in Fig. 3.3(c,d), which corresponds to the superposition of multiple high-order plasmonic modes, recently referred to as a 'pseudo-mode' [112, 125]. However, the negligible $\widetilde{\gamma}_{rad}$ at λ_{pm} shows the large $\widetilde{\gamma}_{tot}$ comes from emission coupled to the pseudo-mode decaying via non-radiative channels ($\widetilde{\gamma}_{tot} = \widetilde{\gamma}_{rad} + \widetilde{\gamma}_{nr}$). In contrast to recent proposals [125], this suggests the nanocavity pseudo-mode quenches emission almost entirely via non-radiative channels, as it does for isolated nanoparticles, suppressing any way to observe possible strong-coupling dynamics. At the NPoM dipole and quadrupole resonant wavelengths, $\widetilde{\gamma}_{rad} \sim \widetilde{\gamma}_{tot}/2$, and therefore information of the coherent energy exchange between the emitter and the plasmon modes are carried to the far-field and thus allows tracking of the hybrid states.

Additionally, the excitation rate $\widetilde{\gamma}_{exc}$ of an emitter next to an isolated nanoparticle is two orders of magnitude smaller than for a 1 nm nanocavity, see Fig. 3.3(e,f). Hence for an isolated nanoparticle where $\widetilde{\gamma}_{rad} \ll \widetilde{\gamma}_{tot}$, an emitter is weakly excited and heavily quenched by higher-order modes. On the other hand, the NPoM nanocavity strongly excites the emitter with the dipole/quadrupole modes, with $\widetilde{\gamma}_{exc}$ increasing for larger nanoparticles, but also significant energy is both radiated ($\widetilde{\gamma}_{rad} \sim \widetilde{\gamma}_{tot}/2$) and exchanged between the emitter and plasmons. Due to the mode hybridization and radiative behavior of higher-order modes for the NPoM, its γ_{em} is dramatically increased and hence allows the room-temperature strong-coupling of a single emitter in plasmonic nanocavities to be experimentally measured [24].

3.5 SUPPRESSED QUENCHING IN FACETED NANOCAVITIES

The previous section assumes that the nanoparticles are perfectly spherical. However, SEM images and experimental results [64, 82] show that nanoparticles are always faceted, see Chapter 2. So far, the emitters have also been placed at the NPoMs' gap centers for varying gap sizes. Although these analyses give intuitive understanding on the phenomenon of suppressed quenching, it is challenging to realize such analyses in experimental setting.

This section investigates the fluorescence emission of an emitter inside a faceted NPoM nanocavity formed by a gold nanoparticle with diameter $2R = 80$ nm and facet widths $w = 0$, 10 and 20 nm atop a dielectric spacer with thickness $d = 5$ nm and a gold mirror, see Fig. 3.4(a). Such a nanocavity can be fabricated using DNA origami (refractive index $n = 2.1$) to precisely control the positions of emitters in the nanocavity.

The bonding SPs of the NPoM nanocavity provide a large field enhancement $|\mathbf{E}|/|\mathbf{E}_0|$ in the gap region. The electric field distribution of the lowest-order bonding plasmon, the BDP, is shown in Fig. 3.4(b) for an NPoM with $w = 20$ nm. The spectral positions of the BDPs for NPoM nanocavities with $w = 0$, 10 and 20 nm are summarized in Fig. 3.4(c) in the form of scattering cross-sections σ_{scat}. The dominant peaks σ_{scat} correspond

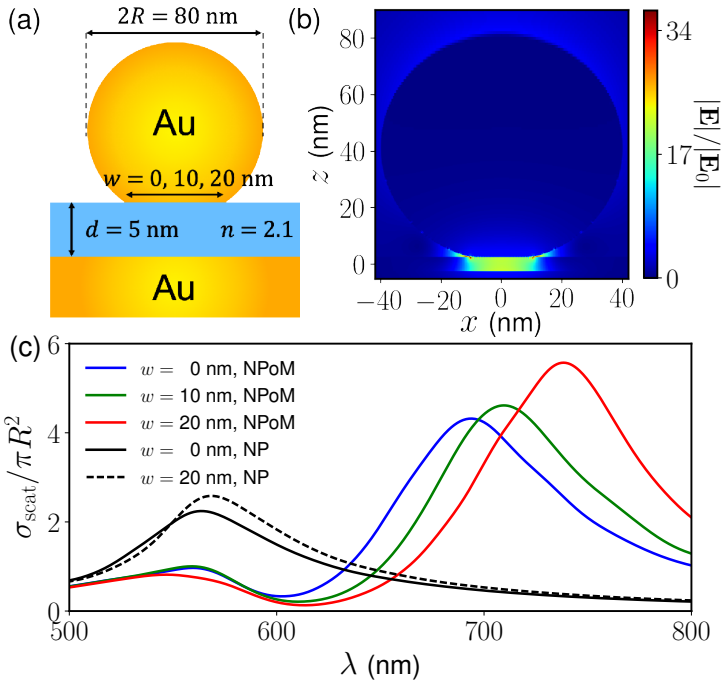

Figure 3.4: FDTD simulations fluorescence emission in faceted NPoMs. (a) Schematic diagram of a nanoparticle-on-mirror (NPoM) nanocavity with diameter 2R = 80 nm, facet width w and gap size d = 5 nm. (b) The field enhancement distribution $|\mathbf{E}|/|\mathbf{E}_0|$ of the bonding dipole plasmon (BDP) of the NPoM with $w = 20$ nm (c) Scattering cross-section σ_{scat} for the NPoM with $w = 0$, 10 and 20 nm and for nanoparticles (NPs) on plain dielectric substrates with $w = 0$ and 20 nm. Reproduced with permission from Ref. [69]. Copyright (2018) EDP Sciences.

to the BDPs, which red-shift from 690 to 730 nm as facet widths increase. The peaks around 570 nm correspond to second-order BQP, and they are spectrally less affected by the facet widths. For comparison, σ_{scat} for nanoparticles placed on plain dielectric substrates are also shown in Fig. 3.4(c) and also exhibit first-order localized surface plasmons at ~570 nm.

When a quantum emitter is placed in an NPoM nanocavity, the large field enhancement of the BDP massively enhances the excitation rate $\widetilde{\gamma}_{exc}$. Fig. 3.5 shows the rate enhancements $\widetilde{\gamma}_{rad}$, $\widetilde{\gamma}_{nr}$, $\widetilde{\gamma}_{exc}$ and $\widetilde{\gamma}_{em}$ computed by placing a classical dipole emitter at 2.5 nm below the nanoparticles for faceted NPoM nanocavities and nanoparticles on dielectric substrates. The results for each nanostructure are evaluated at the resonance frequency of the nanostructure's dominant plasmon modes, as shown in Fig. 3.4(c).

As the facet width increases, the nanoparticles experience the lightning rod effect at their sharp facet edges, and, consequently, the rate enhancements of the emitters reach maxima near the facet edges, as seen in Fig. 3.5(b-e), dashed and dash-dotted lines. By

contrast, the rate enhancements for the NPoM nanocavities are maximum at the center of the nanocavity for all facet widths. This is due to the nature of the BDPs which spatially confines the light field at the nanocavities' center. The NPoM nanocavities with larger facet widths also confine light less efficiently and possess larger effective mode volumes. Hence, the rate enhancements of the emitters spatially broaden with increasing facet width.

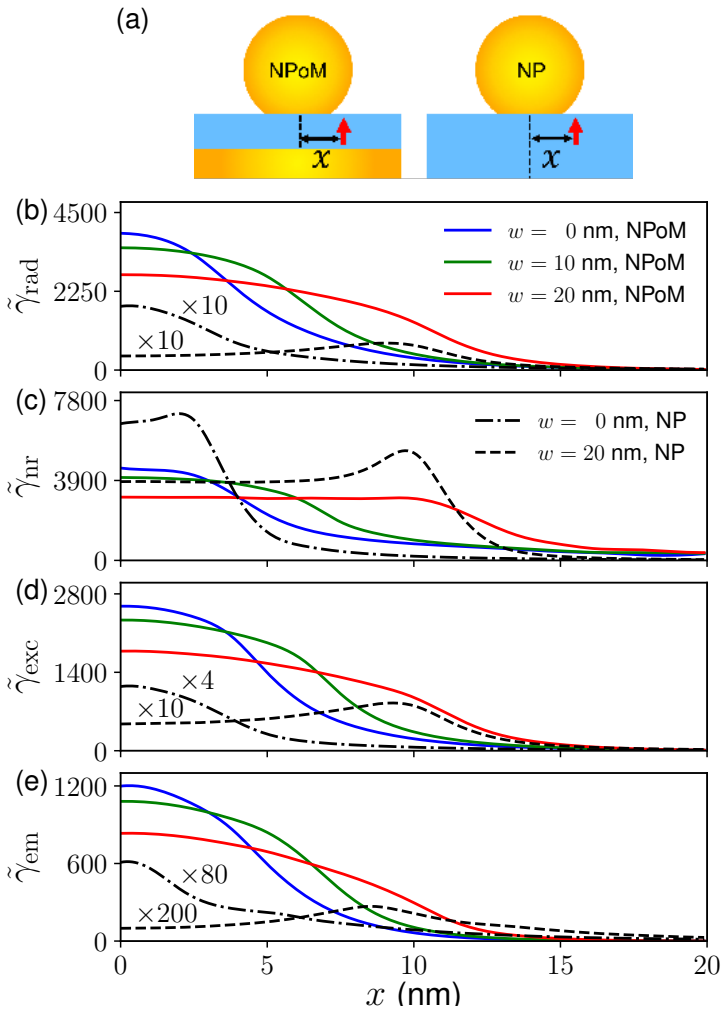

Figure 3.5: FDTD simulations for (a) the radiative decay $\tilde{\gamma}_{rad}$, (b) non-radiative decay $\tilde{\gamma}_{nr}$, (c) excitation $\tilde{\gamma}_{exc}$ and (d) fluorescence enhancements $\tilde{\gamma}_{em}$ for the NPoM nanocavities with facet width $w = 0$, 10 and 20 nm and the nanoparticles on dielectric substrates with $w = 0$ and 20 nm. For clarity, $\tilde{\gamma}_{rad}$, $\tilde{\gamma}_{exc}$ and $\tilde{\gamma}_{em}$ for the nanoparticles are multiplied by the indicated factors. Reproduced with permission from Ref. [69]. Copyright (2018) EDP Sciences.

Unlike Fig. 3.1(a), $\tilde{\gamma}_{em}$ of the emitter below a nanoparticle with $w = 0$ nm is not completely quenched due to the presence of the dielectric substrate which increases the emitter's radiation efficiency, as shown in Fig. 3.5(e). For $w = 20$ nm, $\tilde{\gamma}_{em}$ of the emitter

is quenched as $\widetilde{\gamma}_{nr}$ dominates $\widetilde{\gamma}_{rad}$ and gives a diminishing quantum yield $\eta < 0.03$. On the other hand, plasmon hybridization in the NPoM nanocavities provides sufficiently large $\widetilde{\gamma}_{rad}$ and significant reductions in $\widetilde{\gamma}_{nr}$, giving $\eta \approx 0.4 - 0.5$ at the center of the nanocavity for all facet widths. The NPoM nanocavities provide more than two orders of magnitude increase in $\widetilde{\gamma}_{em}$, drastically enhancing fluorescence of the emitter with $w = 0$ nm and suppressing fluorescence quenching of the emitters $w = 20$ nm, compared to the nanoparticles without the mirror. Hence, a NPoM nanocavity with $w \leqslant 20$ nm retains the ability to suppress quenching and drastically enhance fluorescence.

3.6 EXPERIMENTAL CONFIRMATION OF SUPPRESSED QUENCHING

In collaboration with University of Cambridge where the device was fabricated and experimentally measured, we show in this section the experimental confirmation of the above theoretical findings [68]. A single Cy5 molecule was placed within NPoM nanocavities formed by 80 nm diameter nanoparticles. DNA-origami [33, 39] is used to create a 5 nm-thick spacer and to control the emitter position at nm lateral and vertical accuracies relative to the gold-nanoparticle, see Fig. 3.6(a). A 2-layer DNA-origami plate (55×45 nm) is attached to a gold substrate via thiol-modified staple strands. This is followed by hybridizing ssDNA-functionalized gold nanoparticles with complementary overhang staple strands onto the top of the origami [33]. The position of the dye molecules with respect to the nanoparticle is varied by folding the origami with specific Cy5-modified staples at predefined positions from the center of the nanoparticle attachment groups. The nanocavity is illuminated with a high numerical aperture (NA 0.8) objective, filling the back focal plane of the aperture with 633 nm laser light. To calculate fluorescence enhancement, the emission intensities of the molecules are extracted from their luminescence at 690 nm from > 300 individual NPoM cavities. These intensities are normalized to a control dye molecule on a glass substrate. Note that the sub-ps emission timescales here preclude any direct measurement of emission rates, for any po-

sition of the dye molecule, since current state-of-the-art equipment cannot resolve such fast decays.

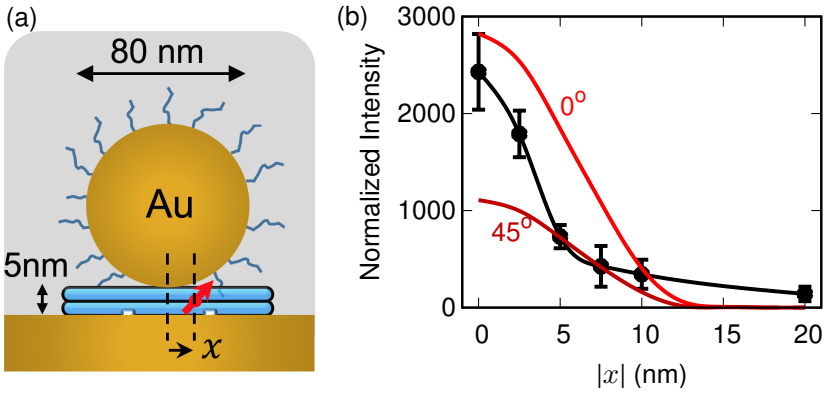

Figure 3.6: FDTD simulations and experiment results for suppressed fluorescence quenching. (a) Schematic diagram of the experimental setup where the Cy5 molecule is represented as a red arrow embedded within the DNA-origami, represented in blue. (b) Experimental (black) and numerical (red) emission intensities of a single Cy5 molecule inside a DNA-origami structure with 5 nm nanocavity gap and 80 nm diameter. The molecule, aligned at angle 0° and 45°, is laterally displaced by x from the center of nanocavity and excited by a 633 nm laser. Reproduced with permission from Ref. [68]. Copyright (2017) American Chemical Society.

In Fig. 3.6(b), the normalized intensities of the molecules at different lateral positions (black points) quantitatively match the numerically-calculated emission rates for dipoles oriented along the z-axis ($\theta = 0°$) and at $\theta = 45°$, as indicated. These results, showing $\tilde{\gamma}_{em}(|x|)$, combine both positive and negative x, which are identical, placing the x=0 particle center within an experimental error of ± 2 nm. Different DNA-origami foldings result in slightly different dipole orientations, and partial melting of the double-stranded DNA together with slight imprecision in nanoparticle placement yields the uncertainty in the emitter position. These small variations lead to different emission intensities in different NPoMs, shown as vertical error bars in the experimental data of Fig. 3.6(b). It is however evident that an emitter in a plasmonic nanocavity does not quench, even if it is placed in the vicinity (< 10 nm) of metal nanostructures, but, instead, its emission rate enhances.

In order to compare the numerical calculations with the experimental results, the fluorescence enhancement factor in Eq. (3.6) must be modified to take into account the

detector collection angle, the molecule's internal dissipation and the molecule's orientation [103]

$$\widetilde{\gamma}_{em}(\mathbf{r}_{em},\theta) = \frac{\sigma(\theta)}{\sigma^0(\theta)} \frac{\gamma_{exc}(\mathbf{r}_{em},\theta)}{\gamma^0_{exc}(\theta)} \frac{\eta(\mathbf{r}_{em},\theta)}{\eta^0(\theta)} \tag{3.8}$$

where σ is the collection efficiency, γ_{exc} is the excitation rate and η is the quantum yield of the Cy5 molecule placed at position $\mathbf{r}$ from the center of the nanocavity and is aligned at angle θ to the vertical axis. On the other hand, σ^0 , γ^0_{exc} and η^0 are the corresponding parameters for the Cy5 molecule embedded in DNA-origami deposited on the glass substrate. Using an objective lens of NA = 0.8, the collection efficiencies of the emitter in the nanocavity are estimated to be $\sigma \approx 0.45$ while the efficiencies for the emitter on glass substrate are $\sigma^0(0°) \approx 0.16$ and $\sigma^0(45°) \approx 0.19$. The quantum yield of the Cy5 molecule on a glass substrate is $\eta^0 \approx 0.25$. The excitation rate enhancement $\gamma_{exc}(\mathbf{r}_{em},\theta)/\gamma^0_{exc}(\theta)$ and the quantum yield $\eta(\mathbf{r},\theta)$ of the emitter in the NPoM nanocavity are then evaluated with FDTD calculation.

3.7 MAXWELL–BLOCH EQUATIONS

The dramatically enhanced γ_{em} for NPoM is the reason that the strong-coupling dynamics can be measured at room temperature. While the classical calculations presented so far provide useful insight into the radiative and non-radiative decay channels of these differing plasmonic systems, they cannot reveal the spatio-temporal dynamics of an emitter coupling to the plasmons. This chapter thus now uses a dynamic semi-classical Maxwell-Bloch description [59] for the emitter.

In the Maxwell-Bloch model, a quantum emitter is treated as a two-level system interacting with a classical electromagnetic field. The emitters can be either in the ground state $|1\rangle$ or excited state $|2\rangle$. Its state can be represented as a wavefunction or a density matrix

$$|\psi\rangle = c_1 |1\rangle + c_2 |2\rangle, \tag{3.9}$$

$$\hat{\varrho} = |\psi\rangle \langle\psi| = \begin{pmatrix} |c_1|^2 & c_1 c_2^* \\ c_1^* c_2 & |c_2|^2 \end{pmatrix} = \begin{pmatrix} \varrho_{11} & \varrho_{12} \\ \varrho_{21} & \varrho_{22} \end{pmatrix}. \tag{3.10}$$

The interaction between the quantum emitter and classical light can be described by the semi-classical form of Jaynes-Cummings Hamiltonian in Eq. (1.6) [59]

$$\begin{aligned}\widehat{H} &= \hbar\omega_{em}\hat{\sigma}^{\dagger}\hat{\sigma} - \hat{\boldsymbol{\mu}}\cdot\mathbf{E} \\ &= \hbar\omega_{em}\hat{\sigma}^{\dagger}\hat{\sigma} - \boldsymbol{\mu}\cdot\mathbf{E}\left(\hat{\sigma}+\hat{\sigma}^{\dagger}\right) \\ &= \begin{pmatrix} 0 & -\boldsymbol{\mu}\cdot\mathbf{E} \\ -\boldsymbol{\mu}\cdot\mathbf{E} & \hbar\omega_{em}\end{pmatrix}\end{aligned} \tag{3.11}$$

where $\boldsymbol{\mu} = \langle 2|\hat{\boldsymbol{\mu}}|1\rangle$, $\hat{\sigma} = |1\rangle\langle 2|$ and $\hat{\sigma}^{\dagger}\hat{\sigma} = |2\rangle\langle 2|$. In most systems, the quantum emitter is not only coupled with the electromagnetic field of interest but is also exposed to external reservoirs. The time dynamic of the emitters can be obtained by solving the Lindblad master equation for a open quantum system [42]

$$\frac{\partial\hat{\varrho}}{\partial t} = \frac{-i}{\hbar}\left[\widehat{H},\hat{\varrho}\right] + \frac{\gamma}{2}(2\hat{\sigma}\hat{\varrho}\hat{\sigma}^{\dagger} - \hat{\sigma}^{\dagger}\hat{\sigma}\hat{\varrho} - \hat{\varrho}\hat{\sigma}^{\dagger}\hat{\sigma}) + \frac{\gamma_p}{2}(\hat{\sigma}_z\hat{\varrho}\hat{\sigma}_z - \hat{\varrho}). \tag{3.12}$$

where $\hat{\sigma}_z = |2\rangle\langle 2| - |1\rangle\langle 1|$. The first term on the right hand side is the standard von Neumann equation which describes the Hamiltonian evolution of a closed quantum system. The second term describes incoherent relaxation of the emitter with a decay rate γ, and the third term describes pure dephasing with a rate γ_p. They can be written in the matrix form as

$$\frac{-i}{\hbar}\left[\widehat{H},\hat{\varrho}\right] = \frac{-i}{\hbar}\begin{pmatrix} -\boldsymbol{\mu}\cdot\mathbf{E}(\varrho_{21}-\varrho_{12}) & -\boldsymbol{\mu}\cdot\mathbf{E}(\varrho_{22}-\varrho_{11}) - \hbar\omega_{em}\,\varrho_{12} \\ \boldsymbol{\mu}\cdot\mathbf{E}(\varrho_{22}-\varrho_{11}) + \hbar\omega_{em}\,\varrho_{21} & \boldsymbol{\mu}\cdot\mathbf{E}(\varrho_{21}-\varrho_{12})\end{pmatrix} \tag{3.13}$$

$$\frac{\gamma}{2}(2\hat{\sigma}\hat{\varrho}\hat{\sigma}^{\dagger} - \hat{\sigma}^{\dagger}\hat{\sigma}\hat{\varrho} - \hat{\varrho}\hat{\sigma}^{\dagger}\hat{\sigma}) = \begin{pmatrix} \gamma\,\varrho_{22} & -\frac{\gamma}{2}\,\varrho_{12} \\ -\frac{\gamma}{2}\,\varrho_{21} & -\gamma\,\varrho_{22}\end{pmatrix} \tag{3.14}$$

$$\frac{\gamma_p}{2}(\hat{\sigma}_z\hat{\varrho}\hat{\sigma}_z - \hat{\varrho}) = \begin{pmatrix} 0 & -\gamma_p\,\varrho_{12} \\ -\gamma_p\,\varrho_{21} & 0\end{pmatrix}. \tag{3.15}$$

Solving Eq. (3.12) leads to the renowned Maxwell-Bloch equations

$$\frac{\partial\,\varrho_{12}}{\partial t} = \frac{\partial\,\varrho_{21}^{*}}{\partial t} = -(\Gamma - i\omega_{em})\,\varrho_{12} + \frac{i}{\hbar}\boldsymbol{\mu}\cdot\mathbf{E}(\varrho_{22}-\varrho_{11}) \tag{3.16}$$

$$\frac{\partial\, \varrho_{22}}{\partial t} = -\frac{\partial\, \varrho_{11}}{\partial t} = -\gamma\, \varrho_{22} - \frac{2}{\hbar}\boldsymbol{\mu}\cdot\mathbf{E}\, \mathrm{Im}(\varrho_{12}) \tag{3.17}$$

where $\Gamma = \gamma_p + \gamma/2$ is the total dephasing rate. The macroscopic polarization can then be calculated using the relation below

$$\begin{aligned}
\mathbf{P} &= N_d \mathrm{Tr}(\varrho\, \hat{\boldsymbol{\mu}}) \\
&= N_d \mathrm{Tr}\left[\begin{pmatrix} \varrho_{11} & \varrho_{12} \\ \varrho_{21} & \varrho_{22} \end{pmatrix}\begin{pmatrix} 0 & \boldsymbol{\mu} \\ \boldsymbol{\mu} & 0 \end{pmatrix}\right] \\
&= N_d \boldsymbol{\mu}(\varrho_{12} + \varrho_{21}) \\
&= 2N_d \boldsymbol{\mu}\, \mathrm{Re}[\varrho_{12}]
\end{aligned} \tag{3.18}$$

where N_d is the density of electrons involved in the electronic transition $|1\rangle \rightarrow |2\rangle$. Similarly, macroscopic ground and excited state populations are defined as $N_1 = N_d\, \varrho_{11}$ and $N_2 = N_d\, \varrho_{22}$, respectively. Eqs. (3.17) and (3.16) can then be rewritten as follows

$$\frac{\partial^2 \mathbf{P}}{\partial t^2} + 2\Gamma\frac{\partial \mathbf{P}}{\partial t} + (\Gamma^2 + \omega_{em}^2)\mathbf{P} = -\frac{2\omega_{em}}{\hbar}\mu^2(N_2 - N_1)\mathbf{E}(t). \tag{3.19}$$

$$\frac{\partial N_2}{\partial t} = -\frac{\partial N_1}{\partial t} = -\gamma N_2 + \frac{1}{\hbar\omega_{em}}\left(\frac{\partial \mathbf{P}}{\partial t} + \Gamma\mathbf{P}\right)\cdot\mathbf{E}(t). \tag{3.20}$$

The coherent interaction between the emitter and its surrounding optical environment is well described within the Maxwell-Bloch model. However, this model is semi-classical by nature and does not take into account spontaneous emission, which is inherently a quantum phenomenon. The relaxation decay term $-\gamma N_2$ only incoherently reduces the emitter's population inversion and does not generate any electromagnetic field to the environment. As a result, the relaxation rate is also not modified by the Purcell effect.

In the following section, the interaction dynamics between the quantum emitter and its optical environment is rigorously studied by using Eqs. (3.19) and (3.20) together with the FDTD method, as shown in Section A.4. The electric field $\mathbf{E}$ from the environment is calculated by the FDTD method and is used to calculate the polarization field $\mathbf{P}$ in the Maxwell-Bloch equations. $\mathbf{P}$, in turn, couples back to the environment in a self-consistent way through Eq. (A.18).

3.8 STRONG-COUPLING DYNAMICS IN PLASMONIC NANOCAVITIES

Here, a Maxwell-Bloch emitter is considered with realistic parameters: $\mu = 3.79$ Debyes (D), $\gamma = 0.66$ μeV and $2\Gamma = 28$ meV [24]. The emitter is represented the numerical simulations as a cube with dimension $1\times1\times1$ nm^3 and electron density $N_d = 10^{27}$ m^{-3}, assuming that there is only one electron involved in the optical transition.

By dynamically coupling the Maxwell-Bloch model with the full-wave FDTD method, Fig. 3.7 shows realistic energy-exchange dynamics between the emitter and the plasmonic structure, of which all possible plasmonic resonances are included. Fig. 3.7(a) plots the near-field $E_z(\mathbf{r}=0)$ time evolution after a broadband pulsed excitation without (E_z^{cav}, red) and with (E_z^{em}, blue) an emitter placed 0.5 nm from a nanoparticle of diameter 40 nm. The population of the excited state N_2 is also plotted on the same time-scale, which peaks at ~ 20fs. A qualitatively similar behavior is observed for the NPoM in Fig. 3.7(b) but with 4 times stronger field enhancement and 200 times larger excited state population. To clearly demonstrate the induced E-field from the emitter $E_{em}^{ind} = E_z^{em} - E_z^{cav}$, we separate the field due to emitter-plasmon coupling E_z^{em} from the field due to direct plasmon excitation E_z^{cav}. Fig. 3.7(c,d) plots E_{em}^{ind} for emitters placed at various lateral positions away from closest proximity to both the isolated nanoparticle and the NPoM. For emitters at $x < 5$ nm from the isolated NP, E_{em}^{ind} reduces, despite the stronger field enhancement. This shows that energy from the emitter is quenched due to coupling with non-radiative higher-order modes that are confined to the vicinity of the isolated NP. For the NPoM, as the emitter approaches the nanocavity E_{em}^{ind} is instead increasingly enhanced.

Similar behavior is observed from the excited state population dynamics as shown in Fig. 3.7(e,f). For $x < 2.5$ nm from the isolated NP, the population of the excited state is truncated by decay into the non-radiative channels, reducing it below that for an emitter at $x = 5$ nm, a behavior not present for the NPoM cavity. This behavior of extreme plasmonic nanocavities facilitates the strong-coupling of a single emitter at room temperature.

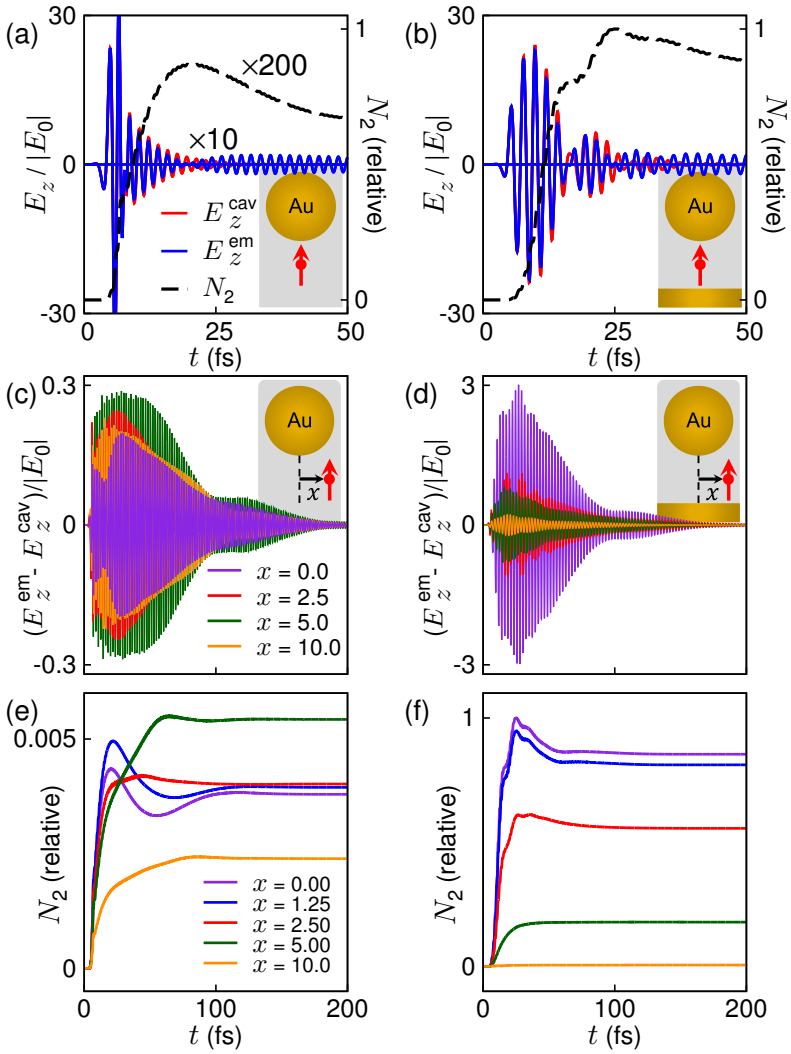

Figure 3.7: FDTD simulations using Maxwell-Bloch equations for the energy exchange dynamics. The field E_z and excited state population N_2 dynamics are shown for (a,c,e) isolated nanoparticle and (b,d,f) 1 nm-wide NPoM of diameter 40 nm for a two-level emitter placed 0.5 nm below the nanoparticle. (a,b) E_z (red, blue) and N_2 (black) dynamics for the structures without (red) and with (blue) the presence of the emitter at $x = 0$. (c,d) The corresponding induced E-fields from the emitter $E_{em}^{ind} = E_z^{em} - E_z^{cav}$ and (e,f) the excited state population N_2 of the emitter, laterally displaced at $x = 0$, 1.25, 2.5, 5 and 10 nm. The emitters' transition wavelengths are $\lambda_{em} = 550$ and 700 nm, tuned to the dipole plasmonic mode of each system. Reproduced with permission from Ref. [68]. Copyright (2017) American Chemical Society.

In fact, Rabi-oscillations can be observed long after the excitation pulse is turned off at ~100 fs for the NPoM while almost entirely absent for the isolated nanoparticle as clearly shown on the envelope dynamics of E_{em}^{ind} at $x = 0$ in Fig. 3.8. Therefore, for $t > 100$ fs, the energy exchange between the plasmon and an emitter is observed. Due to the very dissipative nature of plasmons and the absence of continuous plasmon excitation, the

Rabi oscillations are only visible on a log-scale as shown in Fig. 3.8(c) with period of ~80 fs, which corresponds to the Rabi energy of ~50 meV.

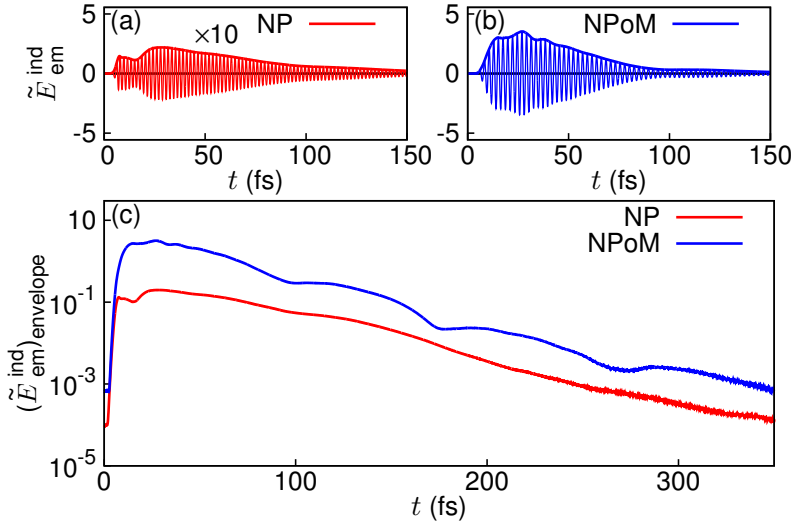

Figure 3.8: FDTD simulations using Maxwell-Bloch equations for the normalized induced field from an emitter $\widetilde{E}^{ind}_{em} = (E^{em}_z - E^{cav}_z)/|E_0|$. The results are shown for (a) an isolated nanoparticle (×10) and (b) the NPoM when the emitter is placed 0.5 nm below the nanoparticle. (c) The envelope dynamics of the induced field on log-scale, which demonstrates the Rabi oscillations. Reproduced with permission from Ref. [68]. Copyright (2017) American Chemical Society.

While Fig. 3.8 demonstrates the Rabi oscillations observed in the near-field from an emitter, to explore the far-field behavior, Fig. 3.9(a,b) plots the scattering cross-sections for an emitter placed at lateral positions $x = 0$, 2.5, and 20 nm for both the isolated nanoparticle and NPoM. Scattering spectra of an isolated nanoparticle show no dependence on the emitter's position. This indicates that the far-field remains oblivious to the emitter as it mainly couples with the dark higher-order modes, and all its energy is channeled in Ohmic losses. However, for the NPoM nanocavity, the Rabi-splitting is observed when the emitter is well within the nanocavity which carries the characteristics of the energy exchange dynamics shown in Fig. 3.8(c). The maximum splitting at $x = 0$ corresponds to the Rabi energy of 66 meV, in comparison with ~50 meV predicted by Fig. 3.8(c).

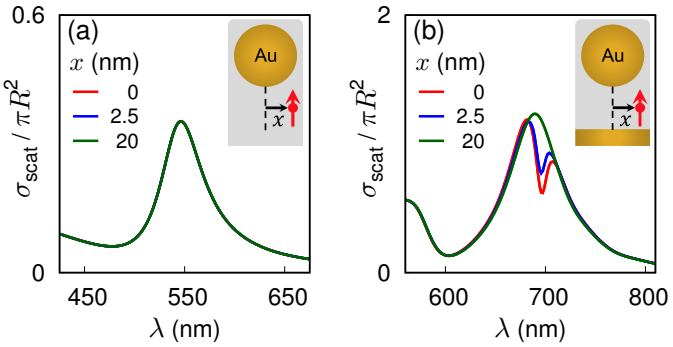

Figure 3.9: FDTD simulations using Maxwell-Bloch equations for scattering cross-sections. The results are shown for (a) an isolated nanoparticle and (b) NPoM, with the two-level quantum emitter placed placed 0.5 nm below the nanoparticle and laterally at x=0, 2.5, and 20 nm. Reproduced with permission from Ref. [68]. Copyright (2017) American Chemical Society.

3.9 CONCLUSION

In conclusion, this chapter demonstrates analytically, numerically, and experimentally that fluorescence emission from an emitter placed within a plasmonic nanocavity does not quench, despite being in very close proximity to metal. This is due to (i) the enhanced excitation which is always present near plasmonic nanostructures and (ii) the acquired radiative nature of higher-order modes for extremely small gaps. The combination of the two effects both suppresses the emitter's decay into non-radiative channels and facilitates the re-emission of its energy. This chapter also investigates how the gap morphology of an NPoM nanocavity affects its interaction with a quantum emitter, showing that faceted NPoMs retain their ability to suppress fluorescence quenching. Indeed, plasmonic nanocavities, with or without facets, do not quench emitters and instead provides the necessary conditions to achieve and observe single-molecule strong-coupling with plasmons at room temperature, and many other related light-matter interactions. Using semi-classical 3D full-wave time-domain Maxwell-Bloch simulations, this chapter uncovers the strong-coupling dynamics of single emitters in plasmonic nanocavities being fundamentally different from isolated nanoparticles and plasmonic nanoantennas with tens of nanometer gaps. We envisage numerous applications, including fast-emitting single-photon sources, nonlinear optics, quantum chemistry and quantum technologies.

4 QUANTUM PLASMONIC IMMUNOASSAY SENSING

The results presented in this chapter have been published in Ref. [130], co-authored by X. Xiong, P. Bai, J. B. You, C. E. Png, L. Wu and O. Hess. Some parts of this chapter are quoted verbatim from the published manuscript.

I ran all of the numerical simulations and contributed to all of the figures. X. Xiong performed data analysis in Fig. 4.4(b,d). All authors contributed to the discussion of the content in this chapter.

4.1 INTRODUCTION

An immunoassay is a biochemical test that measures the presence or concentration of specific molecules in a solution using antibodies [131]. A molecule detected in an immunoassay is often referred to as an "analyte". Clearly, the ultimate goal of immunoassay sensing is to detect a single analyte enabling, for example, diagnosis of early-stage cancer. However, due to the size mismatch between typical analytes (typically $<$10 nm) and the optical wavelength (400$-$700 nm), single-analyte sensing has remained elusive. Hence, most immunoassays rely on specific detectable labels that are chemically linked with antibodies.

In a plasmonic immunoassay, the sensing signal can be further enhanced as plasmonic structures can efficiently squeeze light into tiny, sub-wavelength volumes that are comparable to the size of the analyte. Various types of labels that are chemically linked to antibodies, can further enhance the sensing signals via their interactions with plasmon-polaritons. For example, a dielectric label has been used to induce changes in the refractive index, shifting the plasmonic resonance [132, 133]. In addition to the refractive index change, a metallic nanoparticle label can also induce hybridization of

plasmonic modes with the surrounding structure [134–137]. Fluorophores have also been proposed as sensing labels in surface-plasmon field-enhanced fluorescence spectroscopy [138–140] where the photoluminescence (PL) is enhanced due to the Purcell effect of the plasmonic resonance. In spite of this significant enhancement through a suitable nanoplasmonic environment, the sensing process – interactions between various types of labels and plasmon-polaritons in modern plasmonic immunoassays – have to date not yet explored the strong-coupling quantum regime.

This chapter proposes a new scheme that embeds and utilizes strong-coupling between quantum emitter label(s) and plasmon-polaritons to achieve a drastically enhanced sensitivity, down to a single-analyte quantum plasmonic immunoassay. It is from this single-analyte perspective that this chapter shall in the following starts its discussion before subsequently moving to the experimentally more common multi-analyte (ensemble) case. In each case, the ultra-sensitivity is achieved via the characteristic spectral signature of Rabi splitting which is effectively a bi-directional shift. Compared to label-free plasmonic sensing, the presence of quantum emitter labels enhance the sensitivity by a factor of 14.2, while solitary dielectric and AuNP labels enhance the sensitivity by only factors of 2.62 and 2.73, respectively.

Our statistical studies on multi-analyte detection demonstrate that the proposed protocol also works well in the weak coupling regime (just as conventional plasmonic sensors do) when the emitter labels are displaced from the plasmonic hotspot. In the case of multiple randomly positioned analytes, the optical spectrum of the composite system is not necessarily associated with a Lorentzian line-shape and, consequently, a figure of merit (FoM) is introduced as the integral of the spectral changes. The immunoassay-FoM in the weak coupling (or classical) regime decreases rapidly with decreasing number of analytes. In contrast, the immunoassay-FoM in the strong coupling (or quantum) regime remains approximately constant, independent of the concentration of emitter labels. Indeed, it retains this value also for a single emitter label.

4.2 STRONG-COUPLING IMMUNOASSAY

The principle and set-up of the proposed quantum plasmonic immunoassay sensing protocol are schematically illustrated in Fig. 4.1a. It functionally involves four main parts: (i) a plasmonic nano-dimer cavity (here formed by two gold hemispheres), (ii) an antigen as the "analyte" to be detected, (iii) a sensing label (which is used to enhance the sensitivity in either a classical or quantum regime), and (iv) two antibodies which are paired with the target antigen and chemically linked with the sensing label, respectively. For the strong-coupling immunoassay, a quantum emitter (such as a quantum dot) is used as the sensing label, and the term "strong-coupling" refers to the strong-coupling between the emitter label and the plasmonic field in the cavity. The sensing label can, however, also be a dielectric or plasmonic nanoparticle resulting in a conventional (classical) plasmonic immunoassay. The immunoassay is assumed to take place in a liquid environment, such as water or serum, with refractive index 1.33. Dielectric spacers are introduced between the plasmonic hemispheres and the substrate to provide an adjustable vertical position of the hotspot, e.g., to coincide with the sensing label. Figure 4.1b shows the side-view for a representative strong-coupling immunoassay system. The dimer gap between the two nanoplasmonic hemispheres is denoted as d. All the simulations are performed on the basis of a 3D full-wave spatio-temporal simulation method based on a FDTD scheme.

To appreciate the functionality of the various components, let us first establish the optical response of an empty hemisphere dimer. Figure 4.1c shows the normalized electric field distribution of a dimer with a gap d = 2 nm resulting in a plasmonic resonance at 1.89 eV. The characteristic plasmonic hotspot is clearly seen inside the nanogap, with a field enhancement by a factor of 195 at the gap center. It is this enhancement that generally forms the foundation for plasmonic sensing with high sensitivity in an ambient environment. Now to demonstrate the sensitivity of the strong-coupling immunoassay, Fig. 4.1d compares its extinction spectrum (solid red curve) to the spectra of label-free (dotted black curve), dielectric-labeled (dashed blue curve) and AuNP-labeled (dash-dotted green curve) immunoassays. All cases in this study use the same gold hemi-

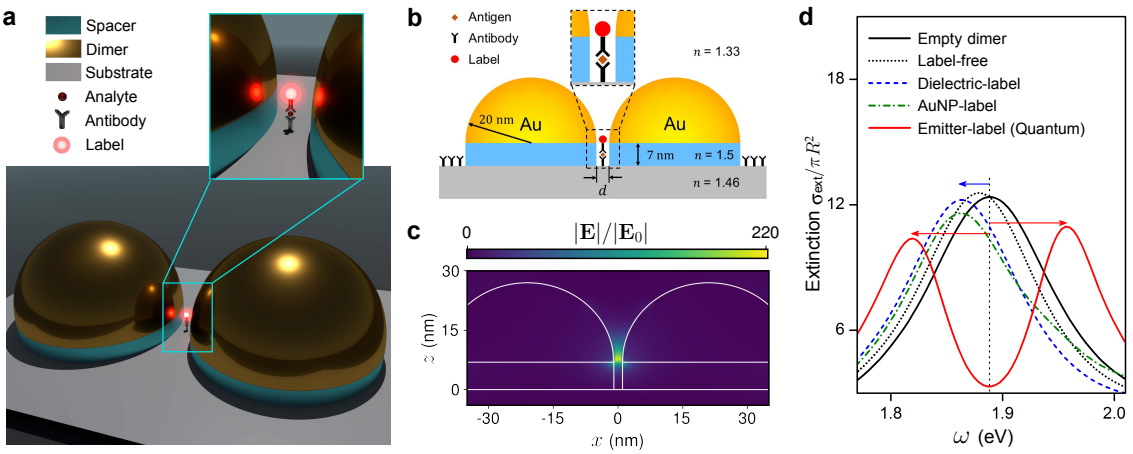

Figure 4.1: FDTD simulations for plasmonic immunoassay. (a) The schematic illustration of the strong-coupling immunoassay setup. A gold hemisphere nano-dimer cavity captures an immunoassay complex in the proximity of the plasmonic hotspot. (b) Side-view of a representative system with a 20nm-radius hemisphere placed on top of the dielectric spacer with a thickness of 7 nm, which matches the thickness of antibody-antigen-antibody complex. (c) Illustration of normalized electric field hotspot located between the distribution inside the dimer. (d) Performance comparisons of different plasmonic sensors: empty dimer (only bottom antibody), label-free (antigen and bottom antibody), dielectric-label, AuNP-label and emitter-label (a Maxwell-Bloch emitter). The extinction cross-sections are normalized by the geometric cross-section of the hemisphere πR^2. Reproduced with permission from Ref. [130]. Copyright (2019) American Chemical Society.

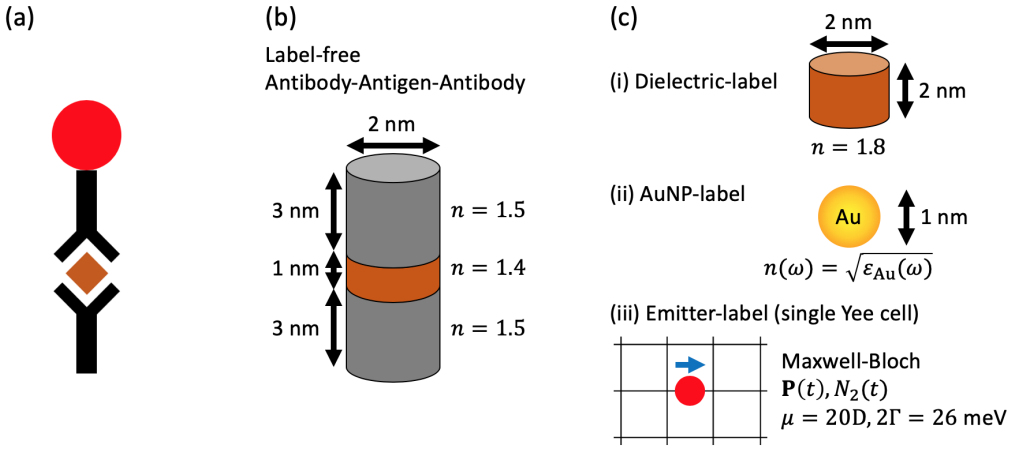

Figure 4.2: (a) The schematic illustration of an antibody-antigen-antibody-label complex. (b) The model of the antibody-antigen-antibody complex (label free). The antibodies are modeled as cylinders with height 3 nm, diameter 2 nm and refractive index 1.5 whereas the antigen is modeled as a cylinder with height 1 nm, diameter 2 nm and refractive index 1.4. (c) The models of the three different labels: (i) dielectric-label as a cylinder with radius 1 nm, height 2 nm and refractive index 1.8, (ii) AuNP-label as a gold sphere with diameter 1 nm and refractive index $n = \sqrt{\varepsilon_{Au}}$ (iii) emitter-label as a single-Yee-cell Maxwell-Bloch emitter with dipole moment 20 Debyes aligned along the x-axis and linewidth $2\Gamma = 26$ meV.

sphere dimer and dielectric spacers but vary the different sensing complexes inside the gap.

In the label-free case, only one antibody and one antigen are placed inside the gap, adjusting the height of the antibody such that the antigen is close to the plasmonic hotspot, while in the case of the labeled complexes the geometry is adjusted such that the label resides close to the plasmonic hotspot. The dielectric label itself is approximated as a simple nano-cylinder (radius of 1 nm and height of 2 nm) with a refractive index of 1.8, whereas the AuNP label is modeled as a gold nano-sphere (with the diameter of 1 nm), see Fig. 4.2(c)(i, ii). This chapter uses a full-wave spatio-temporal Maxwell-Bloch model to take into account the energy exchange dynamics between the two-level quantum emitters (dipole moment 20 Debye and linewidth of 26 meV, see Fig. 4.2(c)(iii)) and the plasmonic field, revealing the dynamics in both weak- and strong-coupling regimes. Compared to conventional sensing protocols that have a characteristic shift of the optical resonance, the strong-coupling immunoassay exhibits the characteristic signature of strong-coupling, i.e., the two Rabi peaks, as indicated in Fig. 4.1d. This is in effect a bi-directional shift with higher sensitivity than those of conventional immunoassays.

4.3 QUANTUM EMITTER MODEL AND NUMERICAL CORRECTION

In this chapter, quantum emitter labels are modeled as two-level systems under the Maxwell-Bloch description, presented in Section 3.7. Unlike the emitters with dipole moment 3.79D used in Chapter 3, the emitter labels considered in this chapter has significantly higher dipole moment of 5 - 20 Debyes (D). Such a quantum emitter with large dipole moment presents a numerical problem in a FDTD simulation.

The field generated by a point-like dipole propagates outwards and only re-excites the dipole once the field is reflected from an inhomogeneity. For a quantum emitter in a FDTD simulation, however, the field $\mathbf{P}$ is injected to the FDTD grid at the emitter's position and re-excite the emitter even without any reflection. This leads us to the second problem of a numerical self-interaction problem which causes spurious frequency shift.

This chapter follows the method presented in Ref. [141] where a quantum emitter is modeled as a point-like source in a FDTD simulation. For a simulation with mesh size Δx, the emitter occupies only a single Yee cell and is assigned density $N_d = 1/\Delta x^3$. The total electric fields $\mathbf{E}$ in Eqs. (3.20) and (3.19) are then corrected by the divergent field $\mathbf{E} \rightarrow \mathbf{E} - \mathbf{E}^{div}$

$$\mathbf{E}^{div} = -(1 + f(\Delta x))\mathbf{P}/3\varepsilon_0\varepsilon_B, \tag{4.1}$$

$$f(\Delta x) = -(3/4\pi)^{2/3}(1.15\omega_{em}\Delta x^3\sqrt{\varepsilon_B}/c)^2. \tag{4.2}$$

4.4 OPTICAL LAMB SHIFTS OF EMITTER LABELS

Before presenting the principles of the strong-coupling immunoassay, it is important to first discuss how optical properties of the quantum emitter is affected by its plasmonic environment. In close proximity to a plasmonic structure, the field generated by the emitter excites plasmonic modes which in turn generate secondary waves which re-excite the emitter. This re-excitation does not only enhance its emission rate but also shift its emission frequency, called Optical Lamb shift (see 1.2.2).

This effect is elaborated by placing a single emitter (dipole moment 20 Debyes) at different positions **1**, **2** and **3** (black, red and blue dots in Fig. 4.3a), with the coordinates $\mathbf{r}_1$ = (0, 0, 0) nm, $\mathbf{r}_2$ = (42, 0, 0) nm, and $\mathbf{r}_3$ = (21, 21, 0) nm. The emitter's polarization is set along the x-axis with transition frequency ω_{em} = 2.03 eV. The electric field distribution of the bare hemisphere dimer is plotted in Fig. 4.3b. It shows that the electric field is the strongest at position **1** and the weakest at position **3**.

Figure 4.3c shows the spectra of the emitter at each position, which are the Fourier transforms $\mathcal{F}[P] = \int P(t)exp(-i\omega t)dt$ of the emitter's polarization density $P(t)$. At positions **2** and **3** (red and blue curves), the coupling between the emitter and the plasmonic environment leads to the red-shifted emitter frequency (major peaks) compared to ω_{em} = 2.03 eV. Stronger electric field results in a larger Lamb shift. Note that, the minor peaks at 1.89 eV represent for the plasmonic resonance. At position **1** where the electric field is the strongest, the emitter resonance experiences the largest red-shift and reaches values

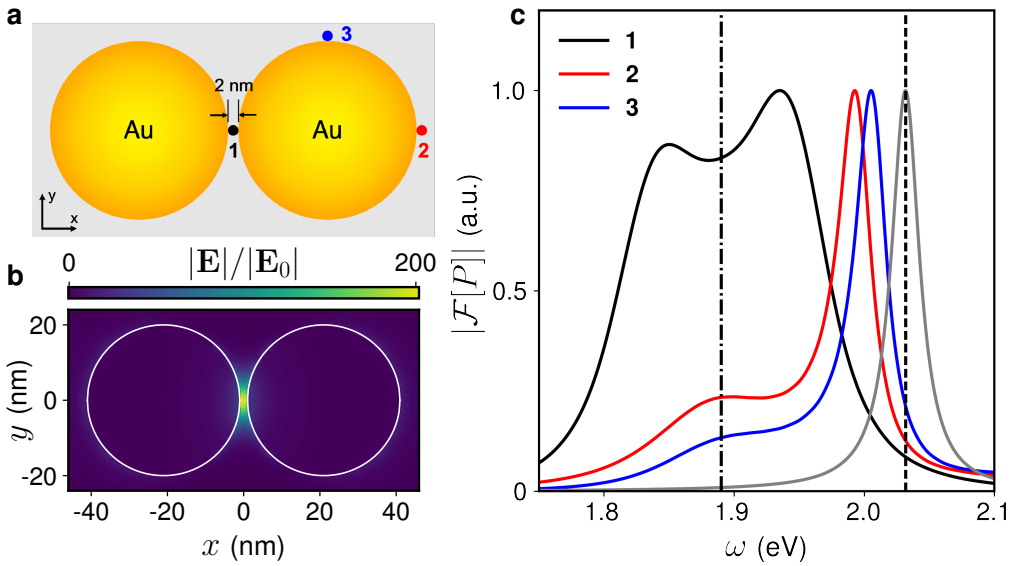

Figure 4.3: FDTD simulations using Maxwell-Bloch equations for optical Lamb shift of a single emitter with dipole moment 20 Debyes due to the interaction with gap plasmons. (a) The top-view schematic diagram of the single emitter's position near the hemisphere dimer. The black, red and blue dots indicate the position of the emitter $\mathbf{r}$ = $\mathbf{r}_1$, $\mathbf{r}_2$ and $\mathbf{r}_3$, respectively. (b) The xy-plane electric field distribution at ω = 1.89 eV for an empty hemisphere dimer, where $|\mathbf{E}(\mathbf{r}_1)|/|\mathbf{E}_0|$ = 194.8, $|\mathbf{E}(\mathbf{r}_2)|/|\mathbf{E}_0|$ = 11.9 and $|\mathbf{E}(\mathbf{r}_3)|/|\mathbf{E}_0|$ = 8.79. (c) The Fourier transforms of the emitter's polarization densities $|\mathcal{F}[\mathrm{P}]|$ at positions $\mathbf{r}_1$ (black), $\mathbf{r}_2$ (red) and $\mathbf{r}_3$ (blue). $|\mathcal{F}[\mathrm{P}]|$ of an emitter in a homogeneous background is also shown as a gray line. The dashed line at ω = 2.03 eV denotes the emitter's transition frequency ω_{em}, and the dash-dotted line at ω = 1.89 eV denotes the gap plasmonic resonance ω_{a}. Reproduced with permission from Ref. [130]. Copyright (2019) American Chemical Society.

around the plasmonic resonance ω_{a} = 1.89 eV. Meanwhile, the emitter and plasmon-polaritons enter into the strong-coupling regime, where the Rabi splitting results in two comparable peaks centered at 1.89 eV. In other words, the optical Lamb shift changes the emitter resonance from $\omega_{\mathrm{em}} = 2.03$ eV to $\omega_{\mathrm{em}}^{\mathrm{L}} = 1.89$ eV. It is important to note that a large optical Lamb shift of 0.14 eV is observed here because the emitter has a large dipole moment of 20 Debyes.

In order to obtain maximum sensing sensitivity, it is crucial to precisely tune plasmonic resonance to an emitter's Lamb-shifted resonance. In an experiment where an emitter cannot be easily changed, plasmonic resonance is often adjusted by changing the size and shape of a plasmonic structure. For simplicity, however, this chapter instead tunes the emitter's transition frequency to the plasmonic resonances of the hemisphere dimer with different gap sizes.

4.5 ANTI-CROSSING OF STRONG-COUPLING

For an emitter coupled with a plasmonic resonance, the system-Hamiltonian can be written as [142]

$$\widehat{H} = \hbar \begin{pmatrix} \omega^{L}(g)_{em} - i\gamma & g \\ g & \omega_a - i\kappa \end{pmatrix} \tag{4.3}$$

where $\omega^{L}_{em}(g)$ is the Lamb shifted resonance of the emitter (which is a function of the coupling strength g) and ω_a is the resonance of the plasmon-polaritons whereas γ and κ are their decay rates, respectively. The coupled system has two new eigenfrequencies expressed as [142]

$$\omega_{\pm}(\Delta_d) = \frac{\omega^{L}_{em} + \omega_a}{2} \pm \mathrm{Re}\left[\sqrt{\frac{1}{4}(\Delta_d - i(\gamma - \kappa))^2 + g^2}\right] \tag{4.4}$$

where $\Delta_d = \omega^{L}_{em} - \omega_a$ is the detuning which can be adjusted to control the optical responses $\omega_{\pm}$ of the coupled system. When the coupling rate is slower than the decay processes $g < |\gamma - \kappa|/2$, the coupled system is in the weak coupling regime where the emitter's emission rate is enhanced by plasmon-polaritons due to the Purcell effect. The system reaches the strong-coupling regime when the coupling exceeds the decay $g > |\gamma - \kappa|/2$, at which the emitter and the plasmon-polaritons become hybridized and coherently exchange energy. In this regime, the hybridized system frequencies ω_+ and ω_- reveal a clear anti-crossing pattern as the emitter's (original) resonance ω_{em} is swept across the plasmonic resonance ω_a. As shown in Fig. 4.4a, the numerically calculated extinction spectra of coupled system show clearly two branches, when the hemisphere dimer with ω_a = 1.89 eV is coupled to emitters with different frequencies ω_{em} = 1.8 - 2.3 eV. In the following, this type of spectral signature is used to characterize the performance of our strong-coupling immunoassay scheme.

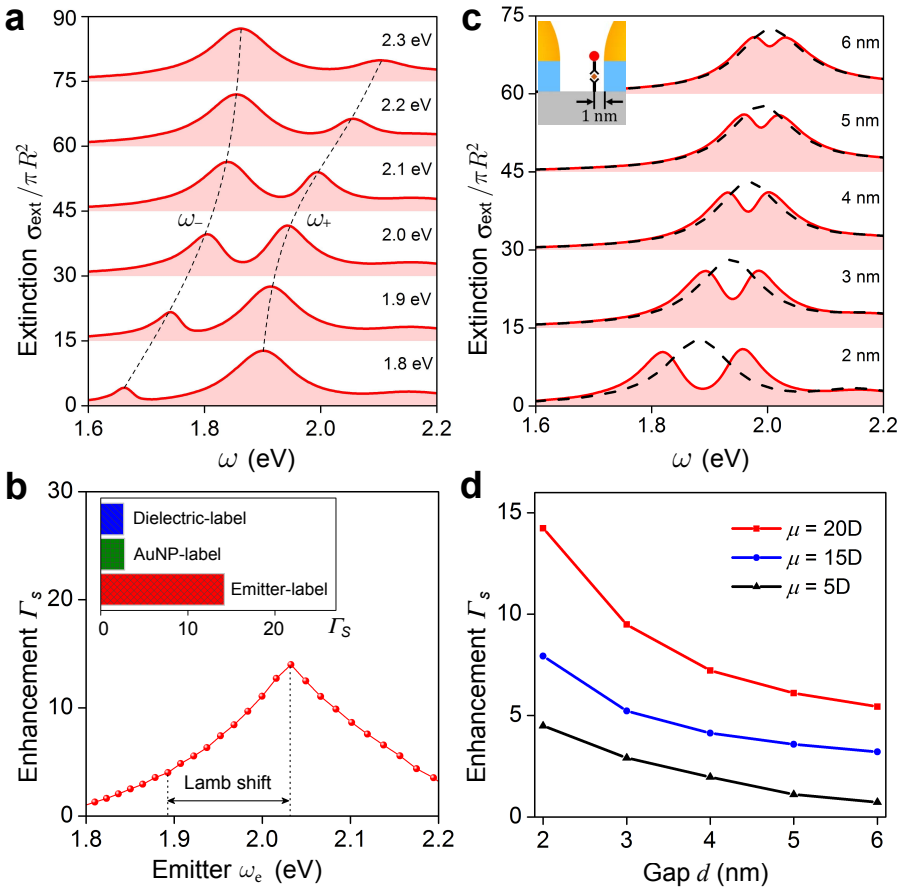

Figure 4.4: FDTD simulations using Maxwell-Bloch equations for (a) spectra of extinction cross-sections σ_{ext} with emitter resonance of ω_{em} = 1.8 - 2.3 eV, and plasmonic resonance fixed at ω_a = 1.89 eV. Two dashed curves denoted as branches ω_+ and ω_- are plotted for the guidance of Rabi splitting. (b) Sensitivity enhancement Γ_S as a function of the emitter resonance ω_{em}, with transition dipole moment μ = 20 Debyes. Inset: comparison of sensitivity enhancement Γ_S for plasmonic sensors with different types of labels. (c) Spectrum of extinction cross-sections σ_{ext} for dimers with d = 2–6 nm, with transition dipole moment μ = 20 Debyes. As the dimer gap d increases, the plasmonic resonance (black dashed lines) shifts, so the emitter resonance is also tuned accordingly. Inset: zoom-in view of the gap region, with the distance between the emitter label and the hemisphere on the right fixed at 1 nm. (d) Sensitivity enhancement Γ_S as a function of the gap size d, with transition dipole moment μ = 5, 10, 20 Debyes (D), respectively. The spectra in (a) and (c) are shifted upward in steps of 15 for clarity. Reproduced with permission from Ref. [130]. Copyright (2019) American Chemical Society.

4.6 SENSITIVITY

For conventional shifting-type plasmonic sensors (e.g., the dotted black, dashed blue, and dash-dotted green curves in Fig. 4.1d), the (sensing) sensitivity is generally defined as the ratio of the change in sensor output (e.g., resonance shift $\delta\omega$) relative to

the change in the quantity to be measured (e.g., concentration of the analyte δc) [143]. However, while δc is a good measure in the case of appreciable analyte concentrations, measuring concentrations is clearly no longer well-applicable in the context of few- or single-analyte detection. Thus, the number of analytes N is adopted (where $N = 1, 2, 3, ...$) as quantifying descriptor to define sensitivity as

$$S_N^{\text{shift}} = \frac{\delta\omega}{N}, \tag{4.5}$$

to be used here to characterize the shifting-type plasmonic sensors for few- or single-analyte detection, an example of which is indicated by the blue arrow in Fig. 4.1d. On the other hand, for the strong-coupling immunoassay (splitting-type), there are double shifts toward both directions, as illustrated by the red arrows in Fig. 4.1d. The measurable frequency splitting between the peaks $\Delta\omega = |\omega_+ - \omega_-|$ can be (analytically) expressed as

$$\Delta\omega = \text{Re}[\sqrt{(\Delta_d - i(\gamma - \kappa))^2 + 4g^2}]. \tag{4.6}$$

Compared to the original resonance detuning $|\Delta_d|$, the system response is modified by $\Delta\omega - |\Delta_d|$ due to the coupling between the emitter(s) and the plasmon-polaritons. Therefore, the sensitivity of the strong-coupling (or splitting-type) immunoassay is defined as

$$S_N^{\text{split}} = \frac{\Delta\omega - |\Delta_d|}{N}. \tag{4.7}$$

Note that in principle, when the emitter and plasmons are on resonance ($\Delta_d = 0$), the frequency difference $\Delta\omega = \sqrt{4g^2 - (\gamma - \kappa)^2}$ corresponds to the Rabi splitting, and the sensitivity S_N^{split} should thus reach its maximum. For the off-resonance cases ($|\Delta_d| > 0$), the sensitivity S_N^{split} is expected to drop. In the context of single-analyte detection ($N = 1$), the sensitivity is purely relevant to the resonance shift for shifting-type sensors ($S_{N=1}^{\text{shift}} = \delta\omega$) or to the resonance splitting for strong-coupling sensors ($S_{N=1}^{\text{split}} = \Delta\omega - |\Delta_d|$).

To directly compare various different types of sensors, the sensitivities are normalized to that of the label-free sensor, denoting the normalized sensitivity as $\Gamma_S = S_N^{\text{label}}/S_N^{\text{label-free}}$, which characterizes the sensitivity enhancement induced by the sensing labels. The inset

of Fig. 4.4b shows the sensitivity enhancement (extracted from the spectra in Fig. 4.1d) for different labels. A clear enhancement of ~15-fold ($\Gamma_S = 14.2$) is observed in strong-coupling immunoassay sensing, making it a competitive candidate for next-generation sensors. The sensitivity enhancement is also extracted for the strong-coupling immunoassay from Fig. 4.4a, which is dependent on the emitter resonance ω_{em} as shown in Fig. 4.4b. Clearly, there exists an optimal Γ_S as the emitter resonance is swept. However, due to the optical Lamb shift experienced by the emitter label, this optimal Γ_S does not occur at ω_a = 1.89 eV when the emitter and the plasmon-polaritons are on resonance. This suggests that the ideal emitter label should be slightly detuned from the plasmonic cavity resonance in order to maximize the sensitivity. In practice, however, it might be more convenient to design a suitably detuned plasmonic cavity for any pre-selected emitter label in a plasmonic immunoassay system.

When seeking to optimize the sensitivity of the immunoassay system, geometrical parameters can be varied such as the gap width d, or a particular emitter label can be chosen with a characteristic transition dipole moment μ. Determining the dependence of the sensitivity enhancement Γ_S on the dimer gap d, we first focus on the spectral response of empty hemisphere dimers of variable gap width d = 2–6 nm as shown in Fig. 4.4c (black dashed lines). As the dimer gap d decreases, the plasmonic resonance is red-shifted, thus the emitter resonance must be tuned for each gap d according to the similar optimization procedure illustrated in Fig. 4.4b. The corresponding extinction spectra with optimized ω_{em} and maximized Γ_S are obtained for various dimer gaps as shown in Fig. 4.4c (red solid lines). For smaller dimer gap d, the Rabi splitting of the coupled system becomes more prominent, indicating stronger coupling strength between the emitter and the plasmon-polaritons. Similarly, the sensitivity enhancement Γ_S is extracted from these extinction spectra. As shown in Fig. 4.4d, Γ_S increases drastically as the dimer gap d decreases. Note that, for this gap size study, the emitter is displaced from the gap center and stays 1 nm away from one of the hemisphere's surface, as illustrated in the inset of Fig. 4.4c. This position is optimized to provide the highest sensitivity enhancement. If the transition dipole moment μ is varied, Fig. 4.4d shows that, as expected, Γ_S increases for larger μ. Typical emitters that are used for strong-coupling include methylene blue ($\omega_{em} \sim 1.878$ eV, $\mu \sim 4$D) [24, 144], J-aggregates ($\omega_{em} \sim 2.145$ eV,

$\mu \sim 30$D) [21, 145], and rhodamine ($\omega_{em} \sim 1.741$ eV, $\mu \sim 5$D) [146, 147]. Moreover, some III-V quantum dots (e.g., InAs and GaAs) [148] and defects in two-dimensional materials (e.g., WS_2 and graphene) [149] have also been used, with their μ ranging from 10 to 10 Debyes. Note that the previously mentioned 15-fold sensitivity enhancement is achieved using a conservative value of $\mu = 20$D. Of course, even higher sensitivity enhancement Γ_S may be anticipated with a larger dipole moment μ. Besides, this study also clearly confirms the preferred choice of dimers with small gaps for improved sensitivity.

4.7 CQED FOR PHOTOLUMINESCENCE SPECTRA

Although the semi-classical model based on the Maxwell-Bloch approach in the previous sections is robust for studying an emitter in a plasmonic environment. The model is not suitable for predicting the spontaneous decay emission of the emitter which is inherently quantum mechanical. In order to study emission from the emitter and its PL spectra, the interaction between an emitter and its optical cavity is treated within the cQED framework. We assume that the 1st-order gap plasmonic mode can be well approximated as a single cavity mode with a bosonic operator a and frequency ω_a. The emitter label is treated as a two-level system with a Pauli-1/2 operator σ and (Lamb shifted) frequency ω_{em}^L. To consider the emitter's frequency as the detuning from the cavity frequency $\omega_{em}^L - \omega_a$, the Jaynes-Cummings Hamiltonian in Eq. (1.6) can be transformed with the unitary operator $U = \exp(-i\omega_a \hat{a}^\dagger \hat{a} t)$ into

$$\widehat{H} = \hbar(\omega_{em}^L - \omega_a)\hat{\sigma}^\dagger\hat{\sigma} + \hbar g(\hat{a}\hat{\sigma}^\dagger + \hat{a}^\dagger\hat{\sigma}) \tag{4.8}$$

where $g = \sqrt{F_{i=1}(\mathbf{r}_{em};\omega_a)\gamma_0\kappa/2}$ is the coupling strength [45], and $F_{i=1}(\mathbf{r}_{em};\omega_a)$ is the local Purcell factor of the 1st-oder ($m = 1$) gap plasmon mode at the emitter's location $\mathbf{r}_{em}$.

The PL spectra can be calculated from the steady-state number of photons $\langle \hat{a}^\dagger \hat{a} \rangle$ in the system, subject to the decoherence from an external reservoir. The steady-state solution

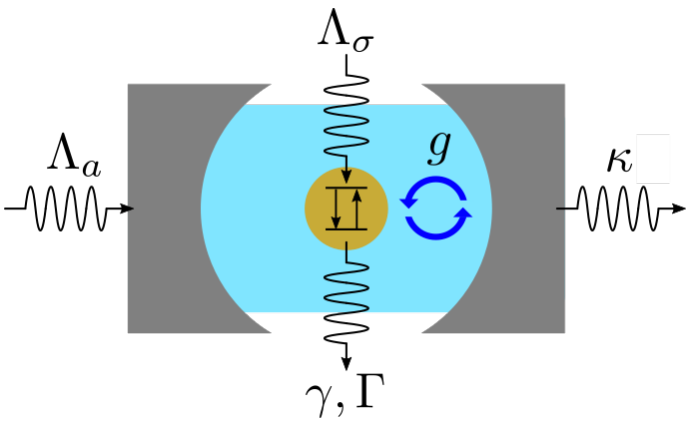

Figure 4.5: A schematic of a cQED representation for plasmon-exciton polaritons. The Plasmonic mode is treated as leaky cavity modes with a pumping rate Λ_a and a decay rate κ. The excitonic mode is treated as a two-level system with a pumping rate Λ_σ, a decay rate γ and a dephasing rate Γ. The excitonic and plasmonic modes couple with a coupling strength g.

can be found by solving the Lindblad master equation $\partial\hat{\varrho}/\partial t = \mathcal{L}\hat{\varrho} = 0$. The Lindblad operator is defined as [150]

$$\begin{aligned}\mathcal{L}\hat{\varrho} = &-\frac{i}{\hbar}[\widehat{H},\hat{\varrho}] + \frac{\kappa}{2}(2\hat{a}\hat{\varrho}\hat{a}^\dagger - \hat{a}^\dagger\hat{a}\hat{\varrho} - \hat{\varrho}\hat{a}^\dagger\hat{a}) \\ &+ \frac{\gamma_{nr}}{2}(2\hat{\sigma}\hat{\varrho}\hat{\sigma}^\dagger - \hat{\sigma}^\dagger\hat{\sigma}\hat{\varrho} - \hat{\varrho}\hat{\sigma}^\dagger\hat{\sigma}) \\ &+ \frac{\Lambda}{2}(2\hat{\sigma}^\dagger\hat{\varrho}\hat{\sigma} - \hat{\sigma}\hat{\sigma}^\dagger\hat{\varrho} - \hat{\varrho}\hat{\sigma}\hat{\sigma}^\dagger) + \frac{\Gamma}{2}(\hat{\sigma}_z\hat{\varrho}\hat{\sigma}_z - \hat{\varrho})\end{aligned} \tag{4.9}$$

where $\kappa = -\mathrm{Im}[\widetilde{\omega}_1]$ is the cavity decay rate, Γ = 13 meV is the dephasing rate, and Λ = 1 meV is the incoherent pumping rate, which is sufficiently weak so that $\langle\hat{a}^\dagger\hat{a}\rangle \ll 1$. The relaxation rate γ_{nr} is defined as the decay rate enhanced by higher-order non-radiative plasmonic modes, which behave collectively as a single pseudomode [39, 112]

$$\gamma_{nr}(\mathbf{r}_{em};\omega) = F_{i>1}(\mathbf{r}_{em};\omega)\gamma_0(\omega) \tag{4.10}$$

where $F_{i>1}(\mathbf{r}_{em};\omega_{em}^L)$ is the Purcell factor of the higher-order modes, which is estimated as $F_{i>1} = F_{tot} - F_{i=1}$ where F_{tot} is the total Purcell factor. Figure 4.6 shows $F_{i=1}$, $F_{i>1}$ and F_{tot} for the hemisphere dimer with gap size d = 2–6 nm, where the dipole source and emitter are placed at position $\mathbf{r}_{em}$.

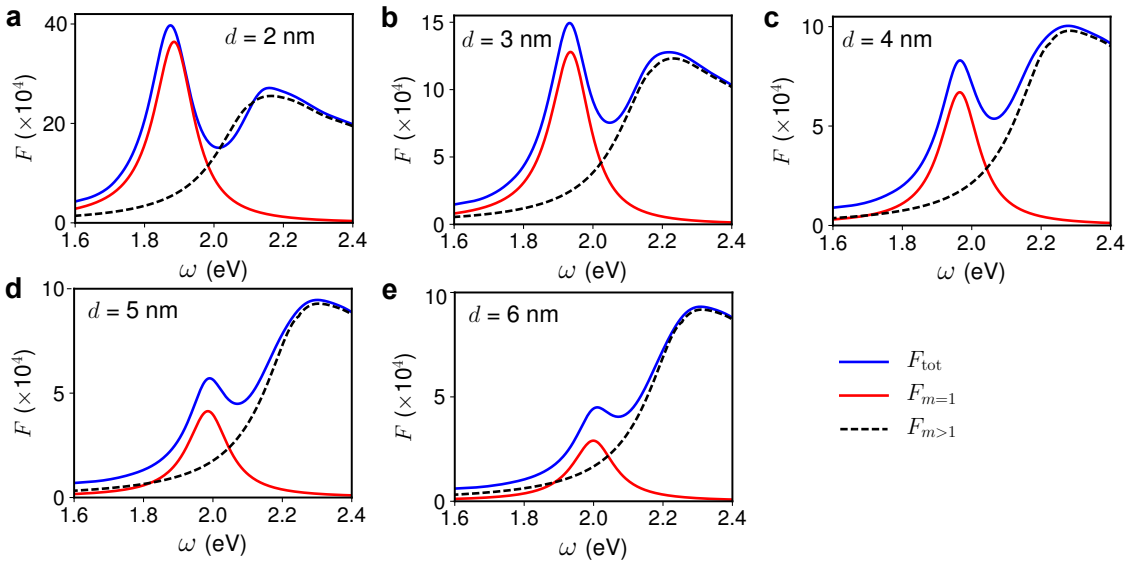

Figure 4.6: FDTD simulations for multi-mode Purcell factors of the hemisphere dimer. (a)-(e) The total Purcell factor F_{tot} calculated by using a dipole source (blue lines), the Purcell factor of the 1st-order QNM $F_{i=1}$ (red lines) and higher-order QNMs $F_{i>1}$ (black dashed lines) for an emitter placed at position $\mathbf{r}_e$ in the dimer with gap size d = 2–6 nm. Reproduced with permission from Ref. [130]. Copyright (2019) American Chemical Society.

Finally, the PL spectra are calculated from the Wiener-Khintchine theorem and the quantum regression theorem [151]

$$\sigma_{PL}(\omega) \propto -\mathrm{Re}\{\mathrm{Tr}[\hat{a}^\dagger(\mathcal{L} - i(\omega - \omega_a)\mathcal{I})^{-1}\hat{a}\hat{\varrho}_0]\} \tag{4.11}$$

where $\hat{\varrho}_0$ is the steady-state solution to Eq. (4.9) and $\mathcal{I}$ is the identity matrix.

4.8 STRONG-COUPLING PHOTOLUMINESCENCE SPECTRA

In typical strong-coupling experiments, the extinction spectrum is usually obtained by measuring the amount of radiation transmitted through the coupled system as a function of the wavelength of the incident light. However, the "splitting" feature manifested in the extinction spectrum is not a sufficient condition to determine the occurrence of strong-coupling between one or more emitters and plasmon-polaritons. In fact, such splitting may also originate from absorption or interference [152]. To rigorously confirm that strong-coupling is achieved, the PL spectrum of the emitter is calculated in the

strong-coupling immunoassay system. Experimentally, this PL spectrum can be measured by exciting the emitter with a pump laser and collecting the luminescence from the coupled system [26, 153]. Fundamentally, both extinction and PL spectra describe the dynamic interactions of the coupled system. However, they originate from different processes: extinction spectra reflect stimulated absorption and emission processes of the coupled system (whose signal interferes with the background excitation light), whereas the PL reveals the spontaneous emission of the coupled system without the background excitation light.

Figure 4.7a shows in direct comparison both the PL and extinction spectra for strong-coupling immunoassay systems with d = 2–6 nm. It is for a (large) gap size of d = 6 nm, where the discrepancy between the PL and extinction spectra becomes most noticeable. Although the extinction spectrum has two splitting resonance peaks, the single peak in the PL spectrum indicates that the emitter and plasmon-polaritons are, in fact, in the weak coupling regime. The splitting peaks in the extinction spectrum emerge simply due to the interference between the emitter and plasmon-polaritons [152]. As the gap size decreases ($d \leqslant 4$ nm), both the PL and extinction spectra have two split peaks, unambiguously indicating the strong-coupling between the emitter and plasmon-polaritons. The occurrence of strong-coupling is perhaps most strongly manifested in the dynamics of the polarization $P(t)$ of the quantum emitter and its dependence on different gap sizes. Figures 4.7b and 4.7c show $P(t)$ normalized by the incident field amplitude $\varepsilon_0|\mathbf{E}_0|$ in linear and logarithmic presentations, respectively. Fig. 4.7b shows a second wave packet for a small gap d = 2 nm as direct evidence of the revival of the emitter [154] which occurs thanks to its interaction with the plasmon-polaritons in the strong-coupling regime. Such dynamics then emerge in the logarithmic presentation as ripples for small dimer gaps ($d < 5$ nm).

The PL spectrum and time-dependent analysis reveal more underlying physics than just the extinction spectrum. However, due to complex energy transfer and recombination processes of the vibrational and defect states [153] involved, it is also experimentally more challenging to observe Rabi splitting in the PL spectrum than in the extinction spectrum.

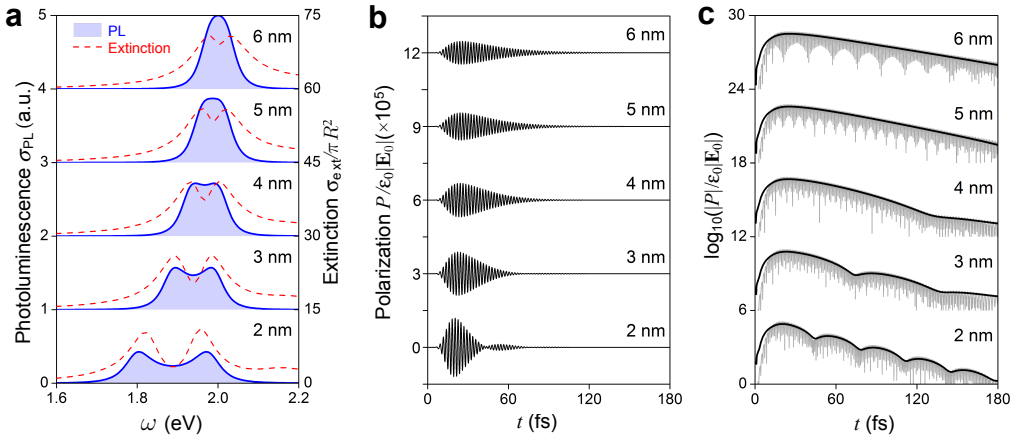

Figure 4.7: (a) Spectrum of PL σ_{PL} calculated from the Lindblad master equation for dimers with d = 2–6 nm and transition dipole moment μ = 20 Debyes. Red dashed lines are the corresponding spectra of extinction cross-sections σ_{ext} calculated from FDTD simulations using Maxwell-Bloch equations. (b) The temporal dynamics of the emitter polarization P(t) for dimers with d = 2–6 nm and transition dipole moment μ = 20 Debyes. (c) The temporal dynamics of polarization |P(t)| (gray curves) and the corresponding envelopes (black curves) in the logarithmic presentation. The curves are shifted upward in steps of (a) 1 for PL and 15 for extinction, (b) 3×10^5, or (c) 6 for clarity. Reproduced with permission from Ref. [130]. Copyright (2019) American Chemical Society.

It is not less challenging to calculate within a cQED framework the combined PL spectrum of an ensemble of analyte-emitter complexes. As the emitters at different locations experience e.g., different amounts of optical Lamb shifts and Purcell enhancements, the emitters cannot be considered indistinguishable. Indeed, even if they are of the same type the retardations and interactions between different emitters must also be considered. Hence, the computation within the cQED framework would increase exponentially with the emitter number. To analyze the sensing properties of a randomly-distributed analyte ensemble, this chapter models the spatio-temporal strong-coupling dynamics in terms of a full-wave Maxwell-Bloch approach [68] adapted to the immunoassay configuration. Adopting an experimentally relevant set-up, this chapter focuses on the extinction spectrum which is of course accurate enough in terms of spectroscopically characterizing the sensing performance through comparisons before and after the adsorption of analyte-emitter complexes.

4.9 STATISTICS AND FIGURE OF MERIT (FOM)

In a typical immunoassay set-up, there are a number of analytes dissolved in a liquid. To realistically model experiments with this set-up in our *in silico* experiment, we now focus on an ensemble of analyte-complexes (each including a quantum emitter), which are randomly distributed in the vicinity of the nano-dimer and subject to an average surface density. This random distribution reflects the consequence of many complex physical and chemical processes such as transport and molecular inter-interaction which indeed merit consideration in future studies. As illustrated in Fig. 4.8a, most of the analyte-complexes will in a typical situation be randomly distributed around the two nano-dimer hemispheres, but there is also the chance to find one or more of the complexes in the gap between the hemispheres. Indeed, with increasing surface density of analyte-emitter complexes the probability to find an analyte-emitter in the center of the dimer gap increases. This reflects the fact that, just like in an *in vitro* experiment, every emitter experiences a different nano-plasmonic environment. Hence, even if all the quantum emitters have resonant frequencies at ω_{em} = 2.03 eV, they exhibits different degrees of the optical Lamb shifts.

The random analyte-emitter complexes are obtained by assigning them on a 2D hexagonal lattice with the center-to-center distance between adjacent hexagons being a = 2 nm, which ensures non-overlapping distribution of the analyte-emitter complexes and corresponds to a surface density of lattice sites $(2/\sqrt{3})a^{-2}$ = 0.289 nm^{-2}. A random number generator was used to determine whether a given lattice site is occupied by an analyte-emitter complex subject to occurrence probabilities of 0.1, 0.2, 0.3, 0.4, 0.5 and 0.6, which correspond to the average surface densities of emitters S = 0.029, 0.058, 0.087, 0.115, 0.144, and 0.173 nm^{-2}, respectively. In order to find the average numbers of analyte-emitter complexes surrounding the plasmonic nanocavity, the cavity mode area is defined as the region where the electric field intensity $|\mathbf{E}|^2$ exceeds 10% of its maximum as $|\mathbf{E}(x,y,0)|^2 > 0.1|\mathbf{E}(x,y,0)|^2_{max}$. This definition gives a cavity mode area of 35.75 nm^2 when d = 2 nm (Fig. 1c), which contains 10.3 lattice sites for analyte-emitter complexes. In this case, the average surface density of emitters and the number of emitters

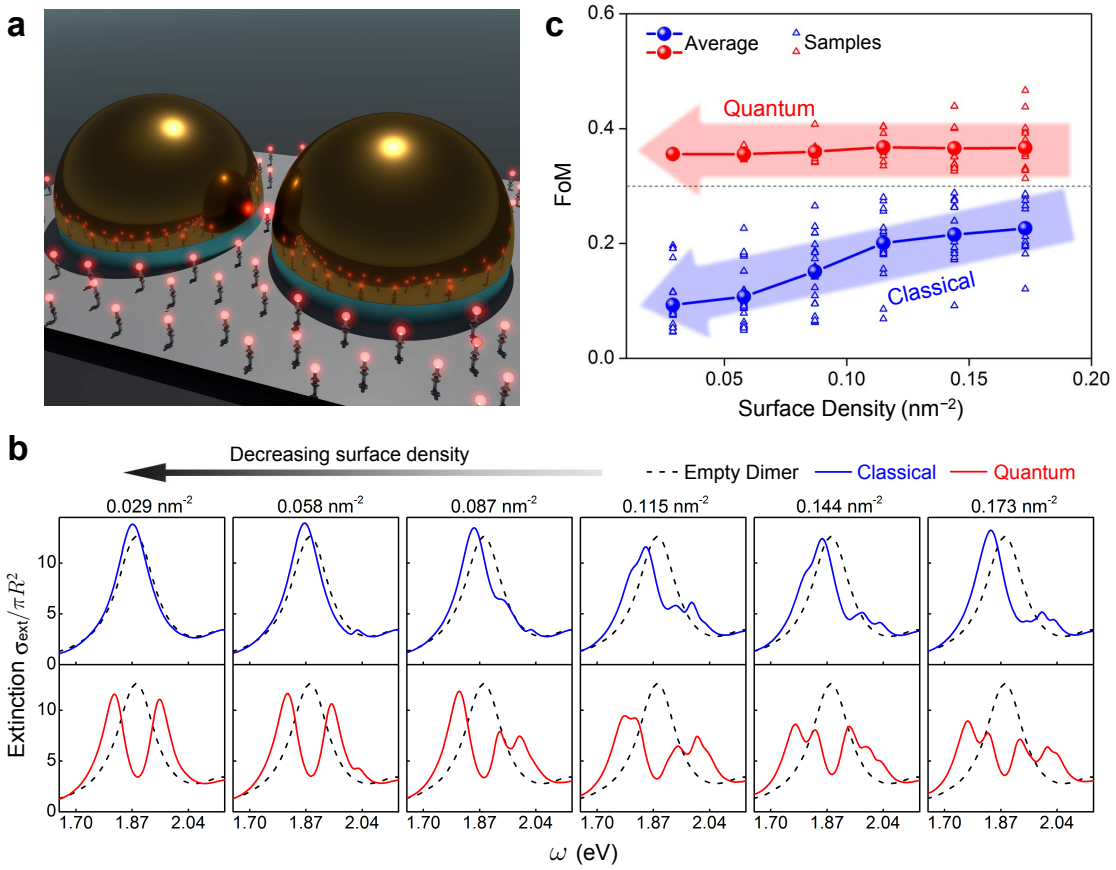

Figure 4.8: (a) Sketch of FDTD simulations using Maxwell-Bloch equations for the multiple analyte-emitter complexes randomly distributed surrounding the hemisphere dimer. The emitter label inside the gap center shall be strongly coupled with plasmonic resonance, while the others remain weakly coupled. (b) Representative spectra of extinction cross-sections σ_{ext} in classical and quantum regimes, with different surface densities of analyte-emitter complexes. (c) The figure of merit (FoM) as a function of the surface density of analyte-emitter complexes. The hollow triangles represent the FoMs of each simulation sample, and the sphere symbols are the mean values at each surface density. The arrows indicate the change of FoM as the surface density of analyte-emitter complexes decreases. Reproduced with permission from Ref. [130]. Copyright (2019) American Chemical Society.

at each occurrence probability are summarized in Table 4.1. Note that, the number of emitters that practically participate in the coupling with plasmon-polaritons varies for each simulation sample. The number of emitters summarized here is only an average value.

A statistical study is performed in the case of multiple analyte-emitter complexes, and obtain the extinction spectra of 30 samples for each surface density. From the large simulation sample space, several representative spectra are selected and classified into two groups, as shown in Fig. 4.8b. For the first group (top row of Fig. 4.8b), the spectra

Occurrence probability	Average surface density (nm^{-2})	Average emitter number
0.1	0.029	1.03
0.2	0.058	2.06
0.3	0.087	3.10
0.4	0.115	4.13
0.5	0.144	5.16
0.6	0.173	6.19

Table 4.1: Average surface densities and average numbers of analyte-emitter complexes. The analyte-emitter complexes are randomly distributed with occurrence probabilities from 0.1 to 0.6 on a 2D hexagonal lattice with lattice constant $a = 2$ nm. The average emitter numbers are determined from the numbers of lattice sites within the area where $|\mathbf{E}(x,y,0)|^2 > 0.1|\mathbf{E}(x,y,0)|^2_{max}$.

(solid blue curves) exhibit a major peak shifted from the original plasmonic resonance (dashed black curves), accompanied by some minor peaks, especially when the surface density increases. For these spectra with one major peak, the interaction between the emitter label and plasmon-polaritons is still in the weak coupling regime, i.e., none of the emitters is in the center of the dimer gap. In contrast, for the second group (bottom row of Fig. 4.8b), the spectra (solid red curves) have two major peaks, each of which may possess their own splitting sub-peaks. This "splitting" indicates that the strong-coupling occurs because of a "random" emitter located in the center of the dimer gap. Accordingly, the first group (or the shifting-type) and the second group (or the splitting-type) are defined as the classical and quantum sensors, respectively.

It is worth noting that, as the surface density of analyte-emitter complexes increases, the spectrum in the quantum regime no longer consists of well-defined (or Lorentz-shape) peaks at distinct frequencies. Therefore, a figure of merit (FoM) is defined to characterize the performance of multi-analyte detection as

$$\mathrm{FoM} = \frac{\int |\sigma_{ext} - \sigma^0_{ext}| d\omega}{\int \sigma^0_{ext} d\omega} \tag{4.12}$$

in which the change of extinction cross-section is integrated over the whole spectral range and normalize it to the extinction cross-section σ^0_{ext} of the empty dimer. This FoM effectively quantifies the optical change before and after the adsorption of the analyte-emitter complexes. The statistics on FoM for different surface densities of analyte-emitter complexes are summarized in Fig. 4.8c, where the hollow triangles represent the samples (30 samples for each surface density). The solid lines show the average

FoMs of classical and quantum sensors at each surface density, and the dotted line at FoM = 0.3 is used to differentiate classical and quantum regimes.

Fig. 4.8c shows that for a large surface density of analyte-emitter complexes, there is no clear boundary between the FoMs of classical and quantum regimes. As the surface density decreases, FoM in the classical regime drops drastically from 0.226 to 0.093. However, the FoM in quantum regime remains almost constant (~ 0.360), because it dominantly results from the single emitter located at the plasmonic hotspot. The frequency histogram of the FoMs is also shown in Fig. 4.9. The two sensing regimes are clearly observed, where the samples have either FoM $<$ 0.3 or FoM $>$ 0.3 depending on whether an analyte-emitter complex is located near the plasmonic hotspot. However, the boundary between the two regimes gradually vanishes at higher surface density, as the analytes tend to occupy all the vacancies on the substrate.

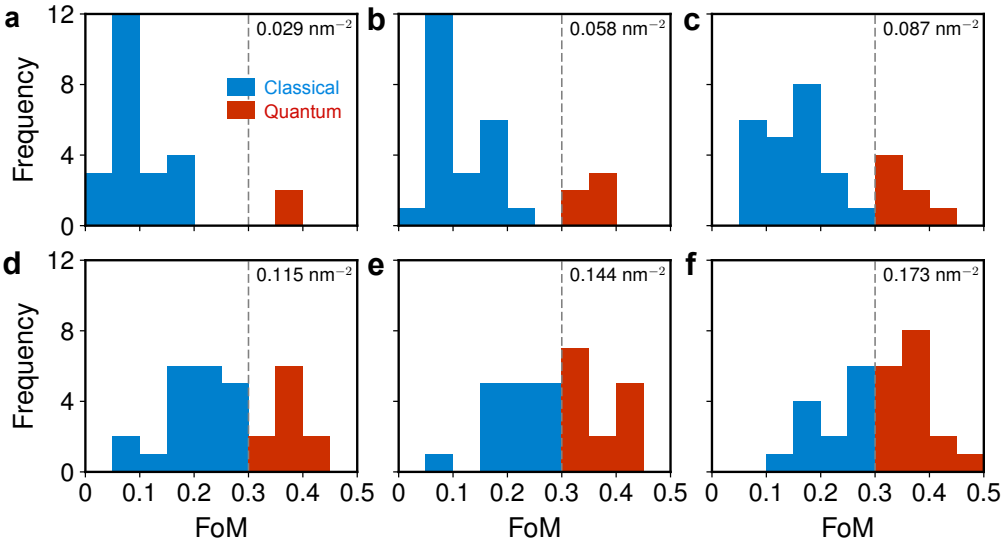

Figure 4.9: Statistics on the figure of merit with different surface densities of analyte-emitter complexes. Histogram of FoM in Fig. 4c with surface density S = 0.029, 0.058, 0.087, 0.115, 0.144 and 0.173 nm^{-2}. The histogram is classified into two colors for the classical regime (blue, FoM $<$ 0.3) and quantum regime (red, FoM $>$ 0.3), with dashed lines denoting the boundary. Reproduced with permission from Ref. [130]. Copyright (2019) American Chemical Society.

The results prove that, toward single-analyte detection, the strong-coupling immunoassay protocol unambiguously outperforms the shifting-type sensors. Note an increased fluctuation in FoM for quantum sensors with increasing surface density. A larger number of quantum emitters randomly scattered near the plasmonic hotspot introduces un-

certainty in the coupling strength due to complex many-body interactions between the emitters and plasmon-polaritons.

So far, this chapter has presented a simple nanostructure with a few-nm gap to demonstrate splitting-type sensing. Such a small size of this gap is clearly not without practical challenges. For example, fabrication of a nanogap must be sufficiently pristine in order to accommodate an antibody, and the steric effect could be significant in such a small gap and prevent a complex from binding at the narrowest (optimal) location. However, our analysis with many different random distributions shows that an analyte does not necessarily have to be at this most narrow point to achieve quantum plasmonic immunoassay sensing. In fact, strong-coupling could be achieved at a larger gap size using a quantum emitter with a larger dipole moment. Alternatively, an open cavity using a plasmonic nanocube [145] could also provide sufficient field confinement at its corners and is certainly more accessible for biomolecules. Another alternative could be detecting a small antigen without a much larger antibody by using artificial proteins to capture the antigen between a plasmonic dimer [155–157].

4.10 CONCLUSION

In summary, this chapter proposes and demonstrates the effectiveness of an innovative immunoassay sensing protocol by employing quantum emitters as sensing labels of antibody-antigen-antibody complexes which in (hemispherical) nanoplasmonic open cavities facilitate room-temperature strong coupling. The proposed splitting-type sensing approach demonstrates a nearly 15-fold sensitivity enhancement over conventional shifting-type label-free plasmonic sensors. The underlying mechanism of the gigantic sensitivity enhancement is attributed to the splitting of the original resonance, which is equivalent to a bi-directional resonance shifting. Using quantum emitter labels with realistically strong transition dipole moments μ, extensive numerical experiments with varying nanogap widths allow us to suggest that nanogaps below 5 nm would be ideal systems for strong coupling conditions and also suggest slight detuning from the plasmonic resonance. Moreover, using randomly distributed multi-analyte systems with

variable random analyte distributions as realistic model systems for biological experiments reveals that our proposed immunoassay protocol is able to perform both classical and quantum sensing. A new figure of merit (FoM) is defined to quantify the spectral difference before and after the adsorption of the analyte-emitter complexes in this multi-analyte study. This chapter shows that with decreasing concentration of analytes, the FoM of classical sensors degrades rapidly from 0.226 to 0.093, yet quantum sensors are able to maintain a stable (around 0.360), concentration-independent FoM. This demonstrates a genuine potential for experiments based on our quantum plasmonic immunoassay sensing protocol to finally reach the single-analyte detection limit. While the current proposal engages a quantum phenomenon (i.e., strong coupling with a quantum emitter) to detect a classical object (i.e., antigen) the approach can conceivably be extended to detect a quantum object such as an electronic spin in nanodiamonds [158–160]. This opens up a new pathway toward plasmonics-enabled room-temperature quantum sensing [161, 162].

5 CONCLUSION AND OUTLOOK

Recent experiments in nanoplasmonics have demonstrated strong-coupling at room temperature by placing single quantum emitters at the gaps between metal nanostructures, [24–26]. At such nanogaps, plasmonic resonances of each nanostructure hybridize, forming plasmonic nanocavities with extreme electromagnetic field confinement far below the diffraction limit. The achievements of these gap plasmonic nanocavities have attracted significant interest due to their potentials to facilitate quantum technologies at room temperature. This thesis employs a variety of theoretical and numerical techniques to investigate the optical properties of gap plasmonic nanocavities and study their interaction with quantum emitters in the weak- and strong-coupling regimes.

To date, most studies on gap plasmonic nanocavities, such as the NPoM geometry, are based on the simple, but ineffective, scattering method. Chapter 2 fills this gap in the literature by employing modal analyses based on the complex-frequency QNM approach. This thesis investigates the optical properties of NPoM nanocavities with different facet widths and their couplings to single dipole sources. Near-field and far-field optical studies of the NPoMs reveal rich interaction involving multiple resonances which reconcile previous experimental inconsistencies [70].

Chapter 3 undermines the previously held belief that fluorescence emission is always quenched when the emitter is placed too close to a plasmonic structure. This chapter demonstrates analytically, numerically, and experimentally that fluorescence quenching is indeed suppressed inside an NPoM nanocavity due to enhanced in- and out-coupling efficiencies of the emitter. This phenomenon implies that a plasmonic nanocavity provides an ideal environment to accommodate and observe light-matter strong-coupling. This is supported by the full-wave FDTD simulations based on the semi-classical Maxwell-Bloch approach.

Finally, the concept of single-emitter strong-coupling in a plasmonic nanocavity is applied in Chapter 4. This chapter proposes an innovative scheme of immunoassay sensing where a quantum emitter label, chemically linked to an antibody-antigen-antibody complex, couples strongly with a hemisphere-dimer plasmonic nanocavity. In contrast to conventional shifting-type plasmonic sensing, the proposed protocol exhibits a bi-directional resonance shifting, based on the Rabi energy splitting, which massively enhances the sensitivity. In order to generalize the proposed protocol, this chapter also conducts statistical studies of strong-coupling plasmonic immunoassay with multiple analyte complexes where classical and quantum sensing regimes are observed. While the classical sensing degraded dramatically with decreasing analyte concentration, the quantum sensing remains stable down to the single-analyte limit.

These results provide comprehensive analyses on singe-emitter coupling in plasmonic nanocavities. However, the work presented here is still imperfect, and it is important to note its limitations. Firstly, the emitters in this thesis are treated as simple two-level systems, neglecting their chemical properties such as vibrational substructures [163] and dark optical transitions [26]. Secondly, metal nanoparticles are approximated as truncated spheres although they have been shown to be faceted spheroids [71]. A more realistic model such as an icosahedron could be used to represent a nanoparticle to take into account plasmonic hot spots at the facet edges and tips. Thirdly, this thesis neglects the non-local responses of conduction electrons [164] since the non-locality has been shown not to qualitatively affect optical properties of plasmonic nanocavities with gap size larger than 1 nm [122–124]. Employing non-local methods, such as the hydrodynamical Drude model [165, 166] or the generalized non-local optical response theory [167], in the analyses in this thesis would yield more accurate quantitative results. Most importantly, future work should explore plasmonic nanocavities as potential realizations of room-temperature quantum technologies [168–172], such as quantum sensors [161], and various functional devices operating at the single-photon level [171, 173, 174].

References

[1] E. Purcell, "Spontaneous emission probabilities at radio frequencies", *Phys. Rev.*, vol. 69, p. 681, 1946.

[2] K. Drexhage, "Iv interaction of light with monomolecular dye layers", *Prog. Opt.*, vol. 12, pp. 163–192, 1974.

[3] M. G. Raizen, R. J. Thompson, R. J. Brecha, H. J. Kimble, and H. J. Carmichael, "Normal-mode splitting and linewidth averaging for two-state atoms in an optical cavity", *Phys. Rev. Lett.*, vol. 63, no. 3, p. 240, 1989.

[4] R. Thompson, G. Rempe, and H. J. Kimble, "Observation of normal-mode splitting for an atom in an optical cavity", *Phys. Rev. Lett.*, vol. 68, no. 8, p. 1132, 1992.

[5] P. Torma and W. L. Barnes, "Strong coupling between surface plasmon polaritons and emitters: A review", *Rep. Prog. Phys.*, vol. 78, no. 1, p. 013 901, 2015.

[6] R. H. Ritchie, "Plasma losses by fast electrons in thin films", *Phys. Rev.*, vol. 106, no. 5, p. 874, 1957.

[7] C. J. Powell and J. B. Swan, "Effect of oxidation on the characteristic loss spectra of aluminum and magnesium", *Phys. Rev.*, vol. 118, no. 3, p. 640, 1960.

[8] V. E. Ferry, J. N. Munday, and H. A. Atwater, "Design considerations for plasmonic photovoltaics", *Adv. Mater.*, vol. 22, no. 43, pp. 4794–4808, 2010.

[9] D. Conklin, S. Nanayakkara, T.-H. Park, M. F. Lagadec, J. T. Stecher, X. Chen, M. J. Therien, and D. A. Bonnell, "Exploiting plasmon-induced hot electrons in molecular electronic devices", *ACS Nano*, vol. 7, no. 5, pp. 4479–4486, 2013.

[10] J. Wang, S. V. Boriskina, H. Wang, and B. M. Reinhard, "Illuminating epidermal growth factor receptor densities on filopodia through plasmon coupling", *ACS Nano*, vol. 5, no. 8, pp. 6619–6628, 2011.

[11] C. S. Rejiya, J. Kumar, V. Raji, M. Vibin, and A. Abraham, "Laser immunotherapy with gold nanorods causes selective killing of tumour cells", *Pharmacol. Res.*, vol. 65, no. 2, pp. 261–269, 2012.

[12] C.-K. Chu, Y.-C. Tu, Y.-W. Chang, C.-K. Chu, S.-Y. Chen, T.-T. Chi, Y.-W. Kiang, and C.-C. Yang, "Cancer cell uptake behavior of au nanoring and its localized surface plasmon resonance induced cell inactivation", *Nanotechnology*, vol. 26, no. 7, p. 075 102, 2015.

[13] S. A. Maier, *Plasmonics: Fundamentals and applications*. Springer Science & Business Media, 2007.

[14] P. Anger, P. Bharadwaj, and L. Novotny, "Enhancement and quenching of single-molecule fluorescence", *Phys. Rev. Lett.*, vol. 96, p. 113 002, 2006.

[15] K. J. Savage, M. M. Hawkeye, R. Esteban, A. G. Borisov, J. Aizpurua, and J. J. Baumberg, "Revealing the quantum regime in tunnelling plasmonics", *Nature*, vol. 491, no. 7425, pp. 574–577, 2012.

[16] E. Prodan, C. Radloff, N. J. Halas, and P. Nordlander, "A hybridization model for the plasmon response of complex nanostructures", *Science*, vol. 302, no. 5644, pp. 419–422, 2003.

[17] W. Zhu, R. Esteban, A. G. Borisov, J. J. Baumberg, P. Nordlander, H. J. Lezec, J. Aizpurua, and K. B. Crozier, "Quantum mechanical effects in plasmonic structures with subnanometre gaps", *Nat. Commun.*, vol. 7, p. 11 495, 2016.

[18] J. Bellessa, C. Symonds, K. Vynck, A. Lemaitre, A. Brioude, L. Beaur, J. C. Plenet, P. Viste, D. Felbacq, E. Cambril, and P. Valvin, "Giant rabi splitting between localized mixed plasmon-exciton states in a two-dimensional array of nanosize metallic disks in an organic semiconductor", *Phys. Rev. B*, vol. 80, no. 3, p. 033 303, 2009.

[19] A. I. Vakevainen, R. J. Moerland, H. T. Rekola, A.-P. Eskelinen, J.-P. Martikainen, D.-H. Kim, and P. Torma, "Plasmonic surface lattice resonances at the strong coupling regime", *Nano Lett.*, vol. 14, no. 4, pp. 1721–1727, 2013.

[20] T. J. Antosiewicz, S. P. Apell, and T. Shegai, "Plasmon–exciton interactions in a core–shell geometry: From enhanced absorption to strong coupling", *ACS Photonics*, vol. 1, no. 5, pp. 454–463, 2014.

[21] G. Zengin, M. Wersall, S. Nilsson, T. J. Antosiewicz, M. Kall, and T. Shegai, "Realizing strong light-matter interactions between single-nanoparticle plasmons and molecular excitons at ambient conditions", *Phys. Rev. Lett.*, vol. 114, no. 15, p. 157 401, 2015.

[22] P. Nordlander, C. Oubre, E. Prodan, K. Li, and M. Stockman, "Plasmon hybridization in nanoparticle dimers", *Nano Lett.*, vol. 4, no. 5, pp. 899–903, 2004.

[23] P. Nordlander and E. Prodan, "Plasmon hybridization in nanoparticles near metallic surfaces", *Nano Lett.*, vol. 4, no. 11, pp. 2209–2213, 2004.

[24] R. Chikkaraddy, B. de Nijs, F. Benz, S. J. Barrow, O. A. Scherman, E. Rosta, A. Demetriadou, P. Fox, O. Hess, and J. J. Baumberg, "Single-molecule strong coupling at room temperature in plasmonic nanocavities", *Nature*, vol. 535, p. 127, 2016.

[25] K. Santhosh, O. Bitton, L. Chuntonov, and G. Haran, "Vacuum rabi splitting in a plasmonic cavity at the single quantum emitter limit", *Nat. Commun.*, vol. 7, p. 11 823, 2016.

[26] H. Grob, J. M. Hamm, T. Tufarelli, O. Hess, and B. Hecht, "Near-field strong coupling of single quantum dots", *Sci. Adv.*, vol. 4, no. 3, 2018.

[27] G. Shvets and I. Tsukerman, *Plasmonics and plasmonic metamaterials analysis and applications*. World Scientific, 2011.

[28] G. Sun and J. B. Khurgin, "Plasmonic enhancement of optical properties by isolated and coupled metal nanoparticles", in *Plasmonics and Plasmonic Metamaterials: Analysis and Applications*, World Scientific, 2012, pp. 1–44.

[29] A. Gonzalez-Tudela, P. A. Huidobro, L. Martin-Moreno, C. Tejedor, and F. J. Garcia-Vidal, "Theory of strong coupling between quantum emitters and propagating surface plasmons", *Phys. Rev. Lett.*, vol. 110, p. 126 801, 12 Mar. 2013.

[30] C. F. Bohren and D. R. Huffman, *Absorption and Scattering of Light by Small Particles*. John Wiley & Sons, Inc, 1998.

[31] L. Yang, H. Wang, Y. Fang, and Z. Li, "Polarization state of light scattered from quantum plasmonic dimer antennas", *ACS Nano*, 2016.

[32] W. Zhu and K. B. Crozier, "Quantum mechanical limit to plasmonic enhancement as observed by surface-enhanced raman scattering", *Nat. Commun.*, vol. 5, p. 5228, 2014.

[33] V. V. Thacker, L. O. Herrmann, D. O. Sigle, T. Zhang, T. Liedl, J. J. Baumberg, and U. F. Keyser, "Dna origami based assembly of gold nanoparticle dimers for surface-enhanced raman scattering", *Nat. Commun.*, vol. 5, p. 3448, 2014.

[34] Z. Fang, L. Fan, C. Lin, D. Zhang, A. J. Meixner, and X. Zhu, "Plasmonic coupling of bow tie antennas with ag nanowire", *Nano Lett.*, vol. 11, no. 4, pp. 1676–1680, 2011.

[35] D. Punj, M. Mivelle, S. B. Moparthi, T. S. Van Zanten, H. Rigneault, N. F. Van Hulst, M. F. Garcia-Parajo, and J. Wenger, "A plasmonic 'antenna-in-box'platform for enhanced single-molecule analysis at micromolar concentrations", *Nat. Nanotechnol.*, vol. 8, no. 7, p. 512, 2013.

[36] L. Li, T. Hutter, U. Steiner, and S. Mahajan, "Single molecule sers and detection of biomolecules with a single gold nanoparticle on a mirror junction", *Analyst*, vol. 138, no. 16, pp. 4574–4578, 2013.

[37] R. W. Taylor, F. Benz, D. O. Sigle, R. W. Bowman, P. Bao, J. S. Roth, G. R. Heath, S. D. Evans, and J. J. Baumberg, "Watching individual molecules flex within lipid membranes using sers", *Sci. Rep.*, vol. 4, p. 5940, 2014.

[38] J. Mertens, A. L. Eiden, D. O. Sigle, F. Huang, A. Lombardo, Z. Sun, R. S. Sundaram, A. Colli, C. Tserkezis, J. Aizpurua, S. Milana, A. C. Ferrari, and J. J. Baumberg, "Controlling subnanometer gaps in plasmonic dimers using graphene", *Nano Lett.*, vol. 13, no. 11, pp. 5033–5038, 2013.

[39] R. Chikkaraddy, V. A. Turek, N. Kongsuwan, F. Benz, C. Carnegie, T. van de Goor, B. de Nijs, A. Demetriadou, O. Hess, U. F. Keyser, and J. J. Baumberg, "Mapping nanoscale hotspots with single-molecule emitters assembled into plasmonic nanocavities using dna origami", *Nano Lett.*, vol. 18, no. 1, pp. 405–411, 2018.

[40] A. Demetriadou, J. M. Hamm, Y. Luo, J. B. Pendry, J. J. Baumberg, and O. Hess, "Spatiotemporal dynamics and control of strong coupling in plasmonic nanocavities", *ACS Photonics*, vol. 4, no. 10, pp. 2410–2418, 2017.

[41] P. T. Kristensen, C. Van Vlack, and S. Hughes, "Generalized effective mode volume for leaky optical cavities", *Opt. Lett.*, vol. 37, no. 10, pp. 1649–1651, 2012.

[42] H.-P. Breuer and F. Petruccione, *The theory of open quantum systems*. Oxford university press, 2006.

[43] A. F. Kockum, A. Miranowicz, S. De Liberato, S. Savasta, and F. Nori, "Ultrastrong coupling between light and matter", *Nat. Rev. Phys.*, vol. 1, no. 1, p. 19, 2019.

[44] L. Novotny and B. Hecht, *Principles of nano-optics*. Cambridge university press, 2012.

[45] F. Marquier, C. Sauvan, and J.-J. Greffet, "Revisiting quantum optics with surface plasmons and plasmonic resonators", *ACS Photonics*, vol. 4, no. 9, pp. 2091–2101, 2017.

[46] N. Zabala, O. Perez-Gonzalez, P. Nordlander, and J. Aizpurua, "Coupling of nanoparticle plasmons with molecular linkers", in *Plasmonics: Metallic Nanostructures and Their Optical Properties IX*, International Society for Optics and Photonics, vol. 8096, 2011, p. 80961L.

[47] O. Perez-Gonzalez, N. Zabala, and J. Aizpurua, "Optical properties and sensing in plexcitonic nanocavities: From simple molecular linkers to molecular aggregate layers", *Nanotechnology*, vol. 25, no. 3, p. 035 201, 2013.

[48] K. Lopata and D. Neuhauser, "Multiscale maxwell–schrodinger modeling: A split field finite-difference time-domain approach to molecular nanopolaritonics", *J. Chem. Phys.*, vol. 130, p. 104 707, 2009.

[49] R. D. Artuso and G. W. Bryant, "Strongly coupled quantum dot-metal nanoparticle systems: Exciton-induced transparency, discontinuous response, and suppression as driven quantum oscillator effects", *Phys. Rev. B*, vol. 82, no. 19, p. 195 419, 2010.

[50] E. Waks and D. Sridharan, "Cavity QED treatment of interactions between a metal nanoparticle and a dipole emitter", *Phys. Rev. A*, vol. 82, no. 4, p. 043 845, 2010.

[51] M. Barbry, P. Koval, F. Marchesin, R. Esteban, A. Borisov, J. Aizpurua, and D. Sanchez-Portal, "Atomistic near-field nanoplasmonics: Reaching atomic-scale resolution in nanooptics", *Nano Lett.*, vol. 15, no. 5, pp. 3410–3419, 2015.

[52] R. Esteban, A. G. Borisov, P. Nordlander, and J. Aizpurua, "Bridging quantum and classical plasmonics with a quantum-corrected model", *Nat. Commun.*, vol. 3, p. 825, 2012.

[53] G. Meunier, *The finite element method for electromagnetic modeling*. John Wiley & Sons, 2010, vol. 33.

[54] A. Taflove and S. C. Hagness, *Computational electrodynamics: The finite-difference time-domain method*. Artech house, 2005.

[55] W. Yan, R. Faggiani, and P. Lalanne, "Rigorous modal analysis of plasmonic nanoresonators", *Phys. Rev. B*, vol. 97, no. 20, p. 205 422, 2018.

[56] J. Yang, J.-P. Hugonin, and P. Lalanne, "Near-to-far field transformations for radiative and guided waves", *ACS Photonics*, vol. 3, pp. 395–402, 2016.

[57] R. C. Ge and S. Hughes, "Design of an efficient single photon source from a metallic nanorod dimer: A quasi-normal mode finite-difference time-domain approach", *Opt. Lett.*, vol. 39, no. 14, pp. 4235–4238, 2014.

[58] P. Bharadwaj and L. Novotny, "Spectral dependence of single molecule fluorescence enhancement", *Opt. Express*, vol. 15, no. 21, pp. 14 266–14 274, 2007.

[59] R. W. Boyd, *Nonlinear optics*. Elsevier, 2008.

[60] A. Deinega and T. Seideman, "Self-interaction-free approaches for self-consistent solution of the maxwell-liouville equations", *Phys. Rev. A*, vol. 89, no. 2, p. 022 501, 2014.

[61] N. Kongsuwan, A. Demetriadou, M. Horton, R. Chikkaraddy, J. J. Baumberg, and O. Hess, "Plasmonic nanocavity modes: From near-field to far-field radiation", *ArXiv preprint arXiv:1910.02273*, 2019.

[62] S. Mubeen, S. Zhang, N. Kim, S. Lee, S. Krämer, H. Xu, and M. Moskovits, "Plasmonic properties of gold nanoparticles separated from a gold mirror by an ultrathin oxide", *Nano Lett.*, vol. 12, no. 4, pp. 2088–2094, 2012.

[63] J. J. Baumberg, J. Aizpurua, M. H. Mikkelsen, and D. R. Smith, "Extreme nanophotonics from ultrathin metallic gaps", *Nat. Mater.*, p. 1, 2019.

[64] D. O. Sigle, J. Mertens, L. O. Herrmann, R. W. Bowman, S. Ithurria, B. Dubertret, Y. Shi, H. Y. Yang, C. Tserkezis, J. Aizpurua, and J. J. Baumberg, "Monitoring morphological changes in 2d monolayer semiconductors using atom-thick plasmonic nanocavities", *ACS Nano*, vol. 9, no. 1, pp. 825–830, 2015.

[65] C. Tserkezis, R. Esteban, D. O. Sigle, J. Mertens, L. O. Herrmann, J. J. Baumberg, and J. Aizpurua, "Hybridization of plasmonic antenna and cavity modes: Extreme optics of nanoparticle-on-mirror nanogaps", *Phys. Rev. A*, vol. 92, p. 053 811, 2015.

[66] J.-H. Huh, J. Lee, and S. Lee, "Comparative study of plasmonic resonances between the roundest and randomly faceted au nanoparticles-on-mirror cavities", *ACS Photonics*, vol. 5, no. 2, pp. 413–421, 2018.

[67] V. Devaraj, H. Jeong, J.-M. Lee, and J.-W. Oh, "Modifying plasmonic-field enhancement and resonance characteristics of spherical nanoparticles on metallic film: Effects of faceting spherical nanoparticle morphology", *Coatings*, vol. 9, no. 6, p. 387, 2019.

[68] N. Kongsuwan, A. Demetriadou, R. Chikkaraddy, F. Benz, V. A. Turek, U. F. Keyser, J. J. Baumberg, and O. Hess, "Suppressed quenching and strong-coupling of purcell-enhanced single-molecule emission in plasmonic nanocavities", *ACS Photonics*, vol. 5, no. 1, pp. 186–191, 2018.

[69] N. Kongsuwan, A. Demetriadou, R. Chikkaraddy, J. J. Baumberg, and O. Hess, "Fluorescence enhancement and strong-coupling in faceted plasmonic nanocavities", *EPJ Appl. Metamat.*, vol. 5, p. 6, 2018.

[70] A. Lombardi, A. Demetriadou, L. Weller, P. Andrae, F. Benz, R. Chikkaraddy, J. Aizpurua, and J. J. Baumberg, "Anomalous spectral shift of near-and far-field plasmonic resonances in nanogaps", *ACS photonics*, vol. 3, no. 3, pp. 471–477, 2016.

[71] F. Benz, R. Chikkaraddy, A. Salmon, H. Ohadi, B. De Nijs, J. Mertens, C. Carnegie, R. W. Bowman, and J. J. Baumberg, "Sers of individual nanoparticles on a mirror: Size does matter, but so does shape", *J. Phys. Chem. Lett.*, vol. 7, no. 12, pp. 2264–2269, 2016.

[72] P. Lalanne, W. Yan, K. Vynck, C. Sauvan, and J.-P. Hugonin, "Light interaction with photonic and plasmonic resonances", *Laser Photonics Rev.*, vol. 12, no. 5, p. 1 700 113, 2018.

[73] E. Ching, P. Leung, A. M. van den Brink, W. Suen, S. Tong, and K. Young, "Quasinormal-mode expansion for waves in open systems", *Rev. Mod. Phys.*, vol. 70, no. 4, p. 1545, 1998.

[74] K. D. Kokkotas and B. G. Schmidt, "Quasi-normal modes of stars and black holes", *Living Rev. Relativ.*, vol. 2, no. 1, p. 2, 1999.

[75] P. T. Kristensen and S. Hughes, "Modes and mode volumes of leaky optical cavities and plasmonic nanoresonators", *ACS Photonics*, vol. 1, no. 1, pp. 2–10, 2014.

[76] Q. Bai, M. Perrin, C. Sauvan, J.-P. Hugonin, and P. Lalanne, "Efficient and intuitive method for the analysis of light scattering by a resonant nanostructure", *Opt. Express*, vol. 21, no. 22, pp. 27 371–27 382, 2013.

[77] D. A. Powell, "Resonant dynamics of arbitrarily shaped meta-atoms", *Phys. Rev. B*, vol. 90, no. 7, p. 075 108, 2014.

[78] X. Zheng, V. K. Valev, N. Verellen, V. Volskiy, L. O. Herrmann, P. Van Dorpe, J. J. Baumberg, G. A. Vandenbosch, and V. Moschchalkov, "Implementation of the natural mode analysis for nanotopologies using a volumetric method of moments (v-mom) algorithm", *IEEE Photonics J.*, vol. 6, no. 4, pp. 1–13, 2014.

[79] C. Sauvan, J. P. Hugonin, I. S. Maksymov, and P. Lalanne, "Theory of the spontaneous optical emission of nanosize photonic and plasmon resonators", *Phys. Rev. Lett.*, vol. 110, p. 237 401, 23 Jun. 2013.

[80] C. A. Balanis, *Antenna theory analysis and design*. Wiley, 2016.

[81] M. Mansuripur, M. Kolesik, and P. Jakobsen, "Leaky modes of solid dielectric spheres", *Phys. Rev. A*, vol. 96, no. 1, p. 013 846, 2017.

[82] J. Mertens, A. Demetriadou, R. W. Bowman, F. Benz, M. E. Kleemann, C. Tserkezis, Y. Shi, H. Y. Yang, O. Hess, J. Aizpurua, and J. J. Baumberg, "Tracking optical welding through groove modes in plasmonic nanocavities", *Nano Lett.*, vol. 16, pp. 5605–5611, 2016.

[83] R. Chikkaraddy, X. Zheng, F. Benz, L. J. Brooks, B. De Nijs, C. Carnegie, M.-E. Kleemann, J. Mertens, R. W. Bowman, G. A. Vandenbosch, V. V. Moshchalkov, and J. J. Baumberg, "How ultranarrow gap symmetries control plasmonic nanocavity modes: From cubes to spheres in the nanoparticle-on-mirror", *ACS Photonics*, vol. 4, no. 3, pp. 469–475, 2017.

[84] P. Goy, J. M. Haimond, M. Gross, and S. Haroche, "Observation of cavity-enhanced single-atom spontaneous emission", *Phys. Rev. Lett.*, vol. 50, no. 24, pp. 1903–1906, 1983.

[85] R. Chance, A. Prock, and R. Silbey, "Lifetime of an excited molecule near a metal mirror: Energy transfer in the eu3+/silver system", *J. Chem. Phys.*, vol. 60, no. 5, pp. 2184–2185, 1974.

[86] D. Kleppner, "Inhibited spontaneous emission", *Phys. Rev. Lett.*, vol. 47, p. 233, 1981.

[87] P. Lodahl, A. F. van Driel, I. S. Nikolaeva, A. Irman, K. Overgaag, D. Vanmaekelbergh, and W. L. Vos, "Controlling the dynamics of spontaneous emission from quantum dots by photonic crystals", *Nature*, vol. 430, p. 654, 2004.

[88] R. Chance, A. Miller, A. Prock, and R. Silbey, "Fluorescence and energy transfer near interfaces: The complete and quantitative description of the eu+ 3/mirror systems", *J. Chem. Phys.*, vol. 63, no. 4, pp. 1589–1595, 1975.

[89] H. Kurczewska and H. Bässler, "Energy transfer across an anthracene-gold interface", *J. Lumin.*, vol. 15, no. 3, pp. 261–266, 1977.

[90] D. Waldeck, A. Alivisatos, and C. Harris, "Nonradiative damping of molecular electronic excited states by metal surfaces", *Surf. Sci.*, vol. 158, no. 1-3, pp. 103–125, 1985.

[91] E. Dulkeith, A. C. Morteani, T. Niedereichholz, T. A. Klar, J. Feldmann, S. A. Levi, F. C. J. M. van Veggel, D. N. Reinhoudt, M. Möller, and D. I. Gittins, "Fluorescence quenching of dye molecules near gold nanoparticles: Radiative and nonradiative effects", *Phys. Rev. Lett.*, vol. 89, p. 203 002, 2002.

[92] J. R. Lakowicz, "Radiative decay engineering 5: Metal-enhanced fluorescence and plasmon emission", *Anal. Biochem.*, vol. 337, no. 2, pp. 171–194, 2005.

[93] D. Markov and P. Blom, "Migration-assisted energy transfer at conjugated polymer/metal interfaces", *Phys. Rev. B*, vol. 72, no. 16, p. 161 401, 2005.

[94] S. Kuhn, U. Hakanson, L. Rogobete, and V. Sandoghdar, "Enhancement of single-molecule fluorescence using a gold nanoparticle as an optical nanoantenna", *Phys. Rev. Lett.*, vol. 97, p. 017 402, 2006.

[95] C. M. Galloway, P. G. Etchegoin, and E. C. L. Ru, "Ultrafast nonradiative decay rates on metallic surfaces by comparing surface-enhanced raman and fluorescence signals of single molecules", *Phys. Rev. Lett.*, vol. 103, p. 063 003, 2009.

[96] J. N. Farahani, D. W. Pohl, H.-J. Eisler, and B. Hecht, "Single quantum dot coupled to a scanning optical antenna: A tunable superemitter", *Phys. Rev. Lett.*, vol. 95, p. 017 402, 2005.

[97] O. L. Muskens, V. Giannini, J. A. Sanchez-Gil, and J. G. Rivas, "Strong enhancement of the radiative decay rate of emitters by single plasmonic nanoantennas", *Nano Lett.*, vol. 7, no. 9, pp. 2871–2875, 2007.

[98] A. Mohammadi, V. Sandoghdar, and M. Agio, "Gold nanorods and nanospheroids for enhancing spontaneous emission", *New J. Phys.*, vol. 10, p. 105 015, 2008.

[99] A. Kinkhabwala, Z. Yu, S. Fan, Y. Avlasevich, K. Mullen, and W. E. Moerner, "Large single-molecule fluorescence enhancements produced by a bowtie nanoantenna", *Nat. Photonics*, vol. 3, pp. 654–657, 2009.

[100] L. Novotny and N. van Hulst, "Antennas for light", *Nat. Photonics*, vol. 5, pp. 83–90, 2011.

[101] P. Biagioni, J.-S. Huang, and B. Hecht, "Nanoantennas for visible and infrared radiation", *Rep. Prog. Phys.*, vol. 75, p. 024 402, 2012.

[102] A. Pors and S. I. Bozhevolnyi, "Quantum emitters near layered plasmonic nanostructures: Decay rate contributions", *ACS Photonics*, vol. 2, no. 2, pp. 228–236, 2015.

[103] T. B. Hoang, G. M. Akselrod, and M. H. Mikkelsen, "Ultrafast room-temperature single photon emission from quantum dots coupled to plasmonic nanocavities", *Nano Lett.*, vol. 16, no. 1, pp. 270–275, 2016.

[104] Y. C. Jun, R. D. Kekatpure, J. S. White, and M. L. Brongersma, "Nonresonant enhancement of spontaneous emission in metal-dielectric-metal plasmon waveguide structures", *Phys. Rev. B*, vol. 78, p. 153 111, 2008.

[105] R. Faggiani, J. Yang, and P. Lalanne, "Quenching, plasmonic, and radiative decays in nanogap emitting devices", *ACS Photonics*, vol. 2, pp. 1739–1744, 2015.

[106] J. Yang, R. Faggiani, and P. Lalanne, "Light emission in nanogaps: Overcoming quenching", *Nanoscale Horiz.*, vol. 1, pp. 11–13, 2016.

[107] G. Sun and J. B. Khurgin, "Comparative study of field enhancement between isolated and coupled metal nanoparticle: An analytical approach", *Appl. Phys. Lett.*, vol. 97, p. 263 110, 2010.

[108] G. Sun and J. B. Khurgin, "Theory of optical emission enhancement by coupled metal nanoparticles: An analytical approach", *Appl. Phys. Lett.*, vol. 98, no. 11, p. 113 116, 2011.

[109] S. J. Norton and T. Vo-Dinh, "Optical response of linear chains of metal nanospheroids and nanospheroids", *J. Opt. Soc. Am. A*, vol. 25, pp. 2767–2775, 2008.

[110] A. Dhawan, S. J. Norton, M. D. Gerhold, and T. Vo-Dinh, "Comparison of fdtd numerical computations and analytical multipole expansion method for plasmonics-active nanosphere dimers", *Opt. Express*, vol. 17, pp. 9688–9703, 2009.

[111] T. Vo-Dinh, A. Dhawan, S. J. Norton, C. G. Khoury, H.-N. Wang, V. Misra, and M. D. Gerhold, "Plasmonic nanoparticles and nanowires: Design, fabrication and application in sensing", *J. Phys. Chem. C*, vol. 114, pp. 7480–7488, 2010.

[112] A. Delga, J. Feist, J. Bravo-Abad, and F. J. Garcia-Vidal, "Quantum emitters near a metal nanoparticle: Strong coupling and quenching", *Phys. Rev. Lett.*, vol. 112, p. 253 601, 25 Jun. 2014.

[113] J. Gersten and A. Nitzan, "Spectroscopic properties of molecules interacting with small dielectric particles", *J. Chem. Phys*, vol. 75, no. 3, pp. 1139–1152, 1981.

[114] A. M. Kern, A. J. Meixner, and O. J. Martin, "Molecule-dependent plasmonic enhancement of fluorescence and raman scattering near realistic nanostructures", *ACS Nano*, vol. 6, no. 11, pp. 9828–9836, 2012.

[115] T. Hummer, F. Garcia-Vidal, L. Martin-Moreno, and D. Zueco, "Weak and strong coupling regimes in plasmonic qed", *Phys. Rev. B*, vol. 87, no. 11, p. 115 419, 2013.

[116] H. Kautsky, "Quenching of luminescence by oxygen", *Trans. Faraday Soc.*, vol. 35, pp. 216–219, 1939.

[117] H. Knibbe, D. Rehm, and A. Weller, "Intermediates and kinetics of fluorescence quenching by electron transfer", *Ber. Bunsenges. Phys. Chem.*, vol. 72, no. 2, pp. 257–263, 1968.

[118] C. A. Seidel, A. Schulz, and M. H. Sauer, "Nucleobase-specific quenching of fluorescent dyes. 1. nucleobase one-electron redox potentials and their correlation with static and dynamic quenching efficiencies", *J. Phys. Chem.*, vol. 100, no. 13, pp. 5541–5553, 1996.

[119] A. Baker, "Thermal fluorescence quenching properties of dissolved organic matter", *Water Res.*, vol. 39, no. 18, pp. 4405–4412, 2005.

[120] H. Yang, G. Luo, P. Karnchanaphanurach, T.-M. Louie, I. Rech, S. Cova, L. Xun, and X. S. Xie, "Protein conformational dynamics probed by single-molecule electron transfer", *Science*, vol. 302, no. 5643, pp. 262–266, 2003.

[121] D. Gao, Z. Wang, B. Liu, L. Ni, M. Wu, and Z. Zhang, "Resonance energy transfer-amplifying fluorescence quenching at the surface of silica nanoparticles toward ultrasensitive detection of tnt", *Anal. Chem.*, vol. 80, no. 22, pp. 8545–8553, 2008.

[122] C. Tserkezis, N. A. Mortensen, and M. Wubs, "How nonlocal damping reduces plasmon-enhanced fluorescence in ultranarrow gaps", *Phys. Rev. B*, vol. 96, p. 085 413, 2017.

[123] C. Tserkezis, N. Stefanou, M. Wubs, and N. A. Mortensen, "Molecular fluorescence enhancement in plasmonic environments: Exploring the role of nonlocal effects", *Nanoscale*, vol. 8, pp. 17 532–17 541, 2016.

[124] C. Tserkezis, M. Wubs, and N. A. Mortensen, "Robustness of the rabi splitting under nonlocal corrections in plexcitonics", *ACS Photonics*, 2017.

[125] R.-Q. Li, D. Hernangomez-Perez, F. J. Garcia-Vidal, and A. I. Fernandez-Dominguez, "Transformation optics approach to plasmon-exciton strong coupling in nanocavities", *Phys. Rev. Lett.*, vol. 117, p. 107 401, 2016.

[126] R. Zhao, Y. Luo, A. I. Fernandez-Dominguez, and J. B. Pendry, "Description of van der waals interactions using transformation optics", *Phys. Rev. Lett.*, vol. 111, p. 033 602, 2013.

[127] Y. Luo, R. Zhao, and J. B. Pendry, "Van der waals interactions at the nanoscale: The effects of nonlocality", *Proc. Natl. Acad. Sci. U. S. A.*, vol. 111, pp. 18 422–18 427, 2014.

[128] F. J. G. de Abajo, "Multiple scattering of radiation in clusters of dielectrics", *Phys. Rev. B*, vol. 60, p. 6086, 1999.

[129] H. Kuwata, H. Tamaru, K. Esumi, and K. Miyano, "Resonant light scattering from metal nanoparticles: Practical analysis beyond rayleigh approximation", *Appl. Phys. Lett.*, vol. 83, no. 22, pp. 4625–4627, 2003.

[130] N. Kongsuwan, X. Xiong, P. Bai, J.-B. You, C. E. Png, L. Wu, and O. Hess, "Quantum plasmonic immunoassay sensing", *Nano Lett.*, vol. 19, no. 9, pp. 5853–5861, 2019.

[131] D. Wild, *The immunoassay handbook*. Elsevier, 2005.

[132] Y. Wang, J. Dostalek, and W. Knoll, "Magnetic nanoparticle-enhanced biosensor based on grating-coupled surface plasmon resonance", *Anal. Chem.*, vol. 83, no. 16, pp. 6202–6207, 2011.

[133] S. Krishnan, V. Mani, D. Wasalathanthri, C. V. Kumar, and J. F. Rusling, "Attomolar detection of a cancer biomarker protein in serum by surface plasmon resonance using superparamagnetic particle labels", *Angew. Chem., Int. Ed.*, vol. 50, no. 5, pp. 1175–1178, 2011.

[134] L. A. Lyon, M. D. Musick, and M. J. Natan, "Colloidal au-enhanced surface plasmon resonance immunosensing", *Anal. Chem.*, vol. 70, no. 24, pp. 5177–5183, 1998.

[135] X. Hong and E. A. H. Hall, "Contribution of gold nanoparticles to the signal amplification in surface plasmon resonance", *Analyst*, vol. 137, no. 20, pp. 4712–4719, 2012.

[136] S. Szunerits, J. Spadavecchia, and R. Boukherroub, "Surface plasmon resonance: Signal amplification using colloidal gold nanoparticles for enhanced sensitivity", *Rev. Anal. Chem.*, vol. 33, no. 3, pp. 153–164, 2014.

[137] C.-T. Yang, L. Wu, X. Liu, N. T. Tran, P. Bai, B. Liedberg, Y. Wang, and B. Thierry, "Exploiting surface-plasmon-enhanced light scattering for the design of ultrasensitive biosensing modality", *Anal. Chem.*, vol. 88, no. 23, pp. 11 924–11 930, 2016.

[138] T. Liebermann and W. Knoll, "Surface-plasmon field-enhanced fluorescence spectroscopy", *Colloids Surf., A*, vol. 171, no. 1-3, pp. 115–130, 2000.

[139] Y. Wang, A. Brunsen, U. Jonas, J. Dostalek, and W. Knoll, "Prostate specific antigen biosensor based on long range surface plasmon-enhanced fluorescence spectroscopy and dextran hydrogel binding matrix", *Anal. Chem.*, vol. 81, no. 23, pp. 9625–9632, 2009.

[140] Y. Wang, L. Wu, T. I. Wong, M. Bauch, Q. Zhang, J. Zhang, X. Liu, X. Zhou, P. Bai, J. Dostalek, and B. Liedberg, "Directional fluorescence emission co-enhanced by localized and propagating surface plasmons for biosensing", *Nanoscale*, vol. 8, no. 15, pp. 8008–8016, 2016.

[141] E. Schelew, R. C. Ge, S. Hughes, J. Pond, and J. F. Young, "Self–consistent numerical modeling of radiatively damped lorentz oscillators", *Phys. Rev. A*, vol. 95, p. 063 853, 6 Jun. 2017.

[142] D. G. Baranov, M. Wersall, J. Cuadra, T. J. Antosiewicz, and T. Shegai, "Novel nanostructures and materials for strong light–matter interactions", *ACS Photonics*, vol. 5, no. 1, pp. 24–42, 2017.

[143] J. Homola, "Surface plasmon resonance sensors for detection of chemical and biological species", *Chem. Rev.*, vol. 108, no. 2, pp. 462–493, 2008.

[144] K. Patil, R. Pawar, and P. Talap, "Self-aggregation of methylene blue in aqueous medium and aqueous solutions of bu 4 nbr and urea", *Phys. Chem. Chem. Phys.*, vol. 2, no. 19, pp. 4313–4317, 2000.

[145] R. Liu, Z.-K. Zhou, Y.-C. Yu, T. Zhang, H. Wang, G. Liu, Y. Wei, H. Chen, and X.-H. Wang, "Strong light-matter interactions in single open plasmonic nanocavities at the quantum optics limit", *Phys. Rev. Lett.*, vol. 118, no. 23, p. 237 401, 2017.

[146] S. Delysse, J.-M. Nunzi, and C. Scala-Valero, "Picosecond optical kerr ellipsometry determination of s1-sn absorption spectra of xanthene dyes", *Appl. Phys. B: Lasers Opt.*, vol. 66, no. 4, pp. 439–444, 1998.

[147] S. Wuestner, A. Pusch, K. L. Tsakmakidis, J. M. Hamm, and O. Hess, "Overcoming losses with gain in a negative refractive index metamaterial", *Phys. Rev. Lett.*, vol. 105, no. 12, p. 127 401, 2010.

[148] G. Khitrova, H. Gibbs, M. Kira, S. W. Koch, and A. Scherer, "Vacuum rabi splitting in semiconductors", *Nat. Phys.*, vol. 2, no. 2, p. 81, 2006.

[149] E. J. Sie, "Valley-selective optical stark effect in monolayer ws 2", in *Coherent Light-Matter Interactions in Monolayer Transition-Metal Dichalcogenides*, Springer, 2018, pp. 37–57.

[150] H.-P. Breuer and F. Petruccione, *The theory of open quantum systems*. Oxford University Press, 2002.

[151] E. del Valle, F. P. Laussy, and C. Tejedor, "Luminescence spectra of quantum dots in microcavities. ii. fermions", *Phys. Rev. B*, vol. 79, p. 235 326, 23 Jun. 2009.

[152] F. P. Laussy, E. del Valle, and C. Tejedor, "Luminescence spectra of quantum dots in microcavities. i. bosons", *Phys. Rev. B*, vol. 79, p. 235 325, 23 Jun. 2009.

[153] D. Melnikau, R. Esteban, D. Savateeva, A. Sánchez-Iglesias, M. Grzelczak, M. K. Schmidt, L. M. Liz-Marzán, J. Aizpurua, and Y. P. Rakovich, "Rabi splitting in photoluminescence spectra of hybrid systems of gold nanorods and j-aggregates", *J. Phys. Chem. Lett.*, vol. 7, no. 2, pp. 354–362, 2016.

[154] G. Rempe, H. Walther, and N. Klein, "Observation of quantum collapse and revival in a one-atom maser", *Phys. Rev. Lett.*, vol. 58, no. 4, p. 353, 1987.

[155] A. Chevrel, A. Urvoas, I. L. De La Sierra-gallay, M. Aumont-Nicaise, S. Moutel, M. Desmadril, F. Perez, A. Gautreau, H. van Tilbeurgh, P. Minard, and M. Valerio-Lepiniec, "Specific gfp-binding artificial proteins (αrep): A new tool for in vitro to live cell applications", *Biosci. Rep.*, vol. 35, no. 4, e00223, 2015.

[156] T.-J. Yim, Y. Wang, and X. Zhang, "Synthesis of a gold nanoparticle dimer plasmonic resonator through two-phase-mediated functionalization", *Nanotechnology*, vol. 19, no. 43, p. 435 605, 2008.

[157] K. L. Gurunatha, A. C. Fournier, A. Urvoas, M. Valerio-Lepiniec, V. Marchi, P. Minard, and E. Dujardin, "Nanoparticles self-assembly driven by high affinity repeat protein pairing", *ACS Nano*, vol. 10, no. 3, pp. 3176–3185, 2016.

[158] J. R. Maze, P. L. Stanwix, J. S. Hodges, S. Hong, J. M. Taylor, P. Cappellaro, L. Jiang, M. V. G. Dutt, E. Togan, A. S. Zibrov, A. Yacoby, R. L. Walsworth, and M. D. Lukin, "Nanoscale magnetic sensing with an individual electronic spin in diamond", *Nature*, vol. 455, no. 7213, p. 644, 2008.

[159] J. M. Taylor, P. Cappellaro, L. Childress, L. Jiang, D. Budker, P. R. Hemmer, A. Yacoby, R. Walsworth, and M. D. Lukin, "High-sensitivity diamond magnetometer with nanoscale resolution", *Nat. Phys.*, vol. 4, no. 10, p. 810, 2008.

[160] M. W. Doherty, N. B. Manson, P. Delaney, F. Jelezko, J. Wrachtrup, and L. C. Hollenberg, "The nitrogen-vacancy colour centre in diamond", *Phys. Rep.*, vol. 528, no. 1, pp. 1–45, 2013.

[161] W. Fan, B. J. Lawrie, and R. C. Pooser, "Quantum plasmonic sensing", *Phys. Rev. A*, vol. 92, no. 5, p. 053 812, 2015.

[162] C. Lee, F. Dieleman, J. Lee, C. Rockstuhl, S. A. Maier, and M. Tame, "Quantum plasmonic sensing: Beyond the shot-noise and diffraction limit", *ACS Photonics*, vol. 3, no. 6, pp. 992–999, 2016.

[163] M. K. Schmidt, R. Esteban, A. González-Tudela, G. Giedke, and J. Aizpurua, "Quantum mechanical description of raman scattering from molecules in plasmonic cavities", *ACS Nano*, vol. 10, no. 6, pp. 6291–6298, 2016.

[164] C. Ciraci, R. Hill, J. J. Mock, Y. Urzhumov, A. I. Fernandez-Dominguez, S. A. Maier, J. B. Pendry, A. Chilkoti, and D. R. Smith, "Probing the ultimate limits of plasmonic enhancement", *Science*, vol. 337, no. 6098, pp. 1072–1074, 2012.

[165] G. Toscano, S. Raza, A.-P. Jauho, N. A. Mortensen, and M. Wubs, "Modified field enhancement and extinction by plasmonic nanowire dimers due to nonlocal response", *Opt. Express*, vol. 20, no. 4, pp. 4176–4188, 2012.

[166] A. I. Fernandez-Dominguez, A. Wiener, F. J. Garcia-Vidal, S. A. Maier, and J. B. Pendry, "Transformation-optics description of nonlocal effects in plasmonic nanostructures", *Phys. Rev. Lett.*, vol. 108, no. 10, p. 106 802, 2012.

[167] N. A. Mortensen, S. Raza, M. Wubs, T. Sondergaard, and S. I. Bozhevolnyi, "A generalized non-local optical response theory for plasmonic nanostructures", *Nat. Commun.*, vol. 5, p. 3809, 2014.

[168] K. M. Birnbaum, A. Boca, R. Miller, A. D. Boozer, T. E. Northup, and H. J. Kimble, "Photon blockade in an optical cavity with one trapped atom", *Nature*, vol. 436, no. 7047, p. 87, 2005.

[169] J. Kasprzak, S. Reitzenstein, E. A. Muljarov, C. Kistner, C. Schneider, M. Strauss, S. Hofling, A. Forchel, and W. Langbein, "Up on the jaynes–cummings ladder of a quantum-dot/microcavity system", *Nat. Mater.*, vol. 9, no. 4, p. 304, 2010.

[170] P. Vasa and C. Lienau, "Strong light–matter interaction in quantum emitter/metal hybrid nanostructures", *ACS Photonics*, vol. 5, no. 1, pp. 2–23, 2017.

[171] M. Hensen, T. Heilpern, S. K. Gray, and W. Pfeiffer, "Strong coupling and entanglement of quantum emitters embedded in a nanoantenna-enhanced plasmonic cavity", *ACS Photonics*, vol. 5, no. 1, pp. 240–248, 2017.

[172] O. S. Ojambati, R. Chikkaraddy, W. D. Deacon, M. Horton, D. Kos, V. A. Turek, U. F. Keyser, and J. J. Baumberg, "Quantum electrodynamics at room temperature coupling a single vibrating molecule with a plasmonic nanocavity", *Nat. Commun.*, vol. 10, no. 1, p. 1049, 2019.

[173] D. E. Chang, A. S. Sorensen, E. A. Demler, and M. D. Lukin, "A single-photon transistor using nanoscale surface plasmons", *Nat. Phys.*, vol. 3, no. 11, p. 807, 2007.

[174] T. Tiecke, J. D. Thompson, N. P. de Leon, L. R. Liu, V. Vuletic, and M. D. Lukin, "Nanophotonic quantum phase switch with a single atom", *Nature*, vol. 508, no. 7495, p. 241, 2014.

[175] P. B. Johnson and R. W. Christy, "Optical constants of the noble metals", *Phys. Rev. B*, vol. 6, pp. 4370–4379, 12 Dec. 1972.

[176] K. Yee, "Numerical solution of initial boundary value problems involving maxwell's equations in isotropic media", *IEEE Trans. Antennas Propag.*, vol. 14, no. 3, pp. 302–307, 1966.

[177] A. Taflove, "Application of the finite-difference time-domain method to sinusoidal steady-state electromagnetic-penetration problems", *IEEE Trans. Electromagn. Compat.*, no. 3, pp. 191–202, 1980.

[178] S. Wuestner, A. Pusch, K. L. Tsakmakidis, J. M. Hamm, and O. Hess, "Gain and plasmon dynamics in active negative-index metamaterials", *Philos. Trans. R. Soc., A*, vol. 369, no. 1950, pp. 3525–3550, 2011.

A APPENDICES

A.1 ELECTROMAGNETICS OF METALS

Macroscopic electromagnetic waves inside any material can be described by the standard Maxwell's equations in the following form [13]

$$\nabla \cdot \mathbf{D} = \rho_{ext} \tag{A.1}$$

$$\nabla \cdot \mathbf{B} = 0 \tag{A.2}$$

$$\nabla \times \mathbf{E} = -\frac{\partial \mathbf{B}}{\partial t} \tag{A.3}$$

$$\nabla \times \mathbf{H} = \mathbf{J}_{ext} + \frac{\partial \mathbf{D}}{\partial t}. \tag{A.4}$$

These equations describe the dynamics of the electric displacement field $\mathbf{D}$, electric field $\mathbf{E}$, magnetic flux density $\mathbf{B}$ and magnetic field $\mathbf{H}$ with external charge density ρ_{ext} and external current density $\mathbf{J}_{ext}$. This thesis follows the convention in Ref. [13] which distinguishes between internal $(\rho, \mathbf{J})$ and external $(\rho_{ext}, \mathbf{J}_{ext})$ charge and current densities such that the total $\rho_{tot} = \rho + \rho_{ext}$ and $\mathbf{J}_{tot} = \mathbf{J} + \mathbf{J}_{ext}$. This separation is made in order to link internal electromagnetic responses of materials to the macroscopic polarization field $\mathbf{P}$ (electric dipole moment $\mathbf{p}$ per unit volume) and magnetization field $\mathbf{M}$ (magnetic dipole moment $\mathbf{m}$ per unit volume). $\mathbf{P}$ is directly related to ρ via

$$\rho = -\nabla \cdot \mathbf{P}. \tag{A.5}$$

Following the charge conversation $\nabla \cdot \mathbf{J} = -\partial\rho/\partial t$, the relationship between $\mathbf{J}$ and $\mathbf{P}$ can be derived as

$$\mathbf{J} = \frac{\partial \mathbf{P}}{\partial t}. \tag{A.6}$$

P, in turns, is related to Maxwell's equations via the constitutive equations

$$\mathbf{D} = \varepsilon_0 \mathbf{E} + \mathbf{P} \tag{A.7}$$

$$\mathbf{B} = \mu_0 (\mathbf{H} + \mathbf{M}) \tag{A.8}$$

where ε_0 and μ_0 are vacuum permittivity and vacuum permeability, respectively. This thesis only considers non-magnetic materials and neglect the magnetization field $\mathbf{M} = \mathbf{0}$.

A.2 PERMITTIVITY MODELS FOR METALS

The previous subsection discusses the theory of electromagnetics in general macroscopic materials. This section proceeds with the optical properties of metals. The optical response of metal is attributed to its conduction and valence electrons. Here, conduction electrons are treated as nearly free electron gas using Drude theory, while valence electrons are treated as damped harmonic oscillators using Lorentz-Drude theory. These theories are then applied to gold since it is the only metal considered in this thesis.

A.2.1 Drude Model for Conduction Electrons

Macroscopically, conduction electrons behave as plasma where electrons move and bounce off immobile positive ions. The motion of conduction electrons is damped via collisions with positive ions at characteristic collision frequency γ which is in the order of 100 THz at room temperature [13]. In this treatment, the electron-electron interaction is not directly taken into account but implicitly included in electron effective mass m. When the conduction electrons are driven by an external electric field $\mathbf{E}$, their equation of motion is

$$m\frac{d^2}{dt^2}\mathbf{r}(t) + m\gamma\frac{d}{dt}\mathbf{r}(t) = -e\mathbf{E}(t) \tag{A.9}$$

where e is the elementary charge constant. $\mathbf{E}$ drives electrons from their equilibrium positions which causes macroscopic polarization $\mathbf{P} = -N_d e\mathbf{E}$. The equation of motion can be rewritten as

$$\frac{d^2}{dt^2}\mathbf{P}(t) + \gamma\frac{d}{dt}\mathbf{P}(t) = N_d\frac{e^2}{m}\mathbf{E}. \tag{A.10}$$

By considering the Fourier transforms $\mathbf{P}(\omega) = \int \mathbf{P}(t)\exp(-i\omega t)dt$ and $\mathbf{E}(\omega) = \int \mathbf{E}(t)\exp(-i\omega t)dt$, the above expression can be simplified to

$$\mathbf{P}(\omega) = -\varepsilon_0\frac{\omega_p^2}{\omega^2 + i\gamma\omega}\mathbf{E}(\omega) \tag{A.11}$$

where $\omega_p^2 = N_d e^2/\varepsilon_0 m$ is the plasma frequency of the electron gas. Inserting this expression into Eq. (A.7) yields

$$\varepsilon(\omega) = \varepsilon_0 \left(1 - \frac{\omega_p^2}{\omega^2 + i\gamma\omega}\right). \tag{A.12}$$

A.2.2 Lorentz-Drude Model for Valence Electrons

Unlike conduction electrons, valence electrons are bound to positive ions. These electrons can be excited by electromagnetic waves with a frequency close to their electronic transition frequency ω_0. They can be treated as damped harmonic oscillators, and the equation of motion in Eq. (A.9) needs an extra term to describe a restoring force $-m\omega_0^2\mathbf{r}(t)$

$$m\frac{d^2}{dt^2}\mathbf{r}(t) + m\gamma\frac{d}{dt}\mathbf{r}(t) + m\omega_0^2\mathbf{r}(t) = -e\mathbf{E}(t). \tag{A.13}$$

By following the same procedure for deriving Drude permittivity, the Lorentz-Drude permittivity can be rewritten as

$$\varepsilon(\omega) = \varepsilon_0 \left(1 - \frac{\omega_p^2}{\omega^2 - \omega_0^2 + i\gamma\omega}\right). \tag{A.14}$$

This expression can be easily reduced to the Drude permittivity, Eq. (A.12), by setting $\omega_0 = 0$.

Real metals, especially noble metals such as gold and silver, contain electrons in several orbitals with different transition frequencies and different effective masses. The optical properties of real metals cannot be accurately described by either a single Drude or Lorent-Drude permittivity. Hence, an accurate macroscopic description of a real metal requires a combination of the two models, called the N-pole Lorentz-Drude permittivity

$$\varepsilon(\omega) = \varepsilon_\infty \left(1 - \sum_{i=1}^{N} \frac{\omega_{p,i}^2}{\omega^2 - \omega_{0,i}^2 + i\gamma_i\omega}\right) \tag{A.15}$$

where ε_∞ is the asymptotic permittivity at infinite frequency. The second term in the bracket describes the sum of N Lorentz-Drude permittivities for conduction and valence electrons.

A.2.3 Permittivity Model for Gold

For gold, its permittivity in the visible range of electromagnetic waves can be accurately described by two-pole Lorentz-Drude model [55]

$$\varepsilon_{Au}(\omega) = \varepsilon_\infty \left(1 - \frac{\omega_{p,1}^2}{\omega^2 + i\gamma_1\omega} - \frac{\omega_{p,2}^2}{\omega^2 - \omega_{0,2}^2 + i\gamma_2\omega}\right) \tag{A.16}$$

with $\varepsilon_\infty = 6\varepsilon_0$, $\omega_{p,1} = 5.37 \times 10^{15}$ rad/s, $\gamma_1 = 6.216 \times 10^{13}$ rad/s, $\omega_{p,2} = 2.2636 \times 10^{15}$ rad/s, $\omega_{0,2} = 4.572 \times 10^{15}$ rad/s and $\gamma_2 = 1.332 \times 10^{15}$ rad/s. Figure A.1 compares this model with the experimental measurement of gold permittivity [175].

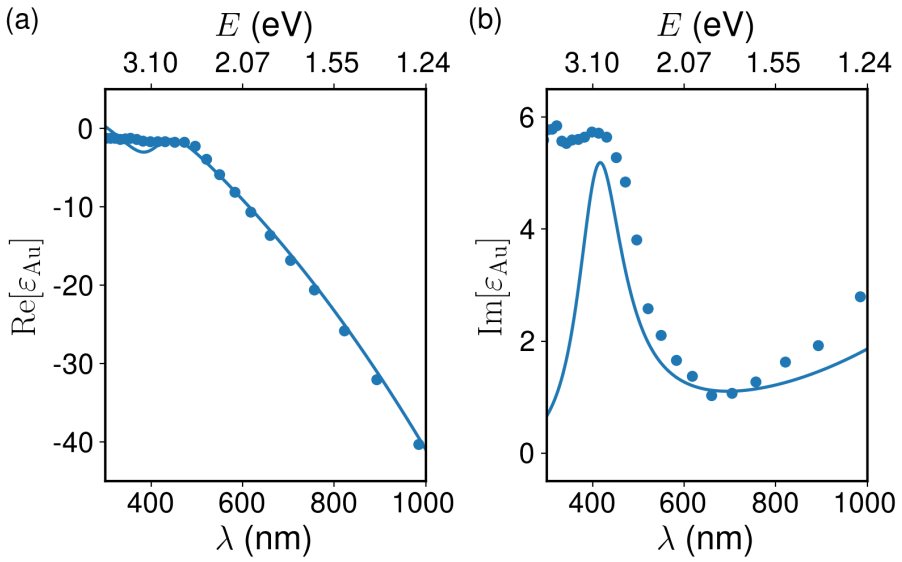

Figure A.1: (a) Real and (b) imaginary parts of two-pole Lorentz-Drude permittivity for gold ε_{Au} are given as solid lines. Data points correspond to experimental results for gold permittivity [175].

A.3 FINITE-DIFFERENCE TIME-DOMAIN METHOD

The FDTD method is a numerical method for solving full wave Maxwell Equations in space and time. It was first invented by Kane S. Yee 1966 [176] and was popularized by Allen Taflove in 1980 [177]. The FDTD method has since been widely used in photonics and plasmonics communities because of its ability to simulate both temporal and spatial electromagnetic responses in arbitrary media. Hence, the method can naturally be used to study active and non-linear devices.

First, the Maxwell equations in Eqs. (A.3) and (A.4) are rewritten as

$$\frac{\partial}{\partial t}\mathbf{H} = -\frac{1}{\mu_0}\nabla \times \mathbf{E} \tag{A.17}$$

$$\frac{\partial}{\partial t}\mathbf{E} = \frac{1}{\epsilon_0}\nabla \times \mathbf{H} - \frac{1}{\epsilon_0}\frac{\partial}{\partial t}\mathbf{P} \tag{A.18}$$

where the system is assumed to be non-magnetic $\mathbf{B} = \mu_0\mathbf{H}$. Yee's seminal paper [176] proposed a method to discretize a simulation space into grid cells, called Yee cell. On a given cell, the components of **E** and **H** are stored in different locations such that each component of **E** is located midway between components of **H**, and vice versa, as shown in Figure A.2. Yee also proposed a leapfrog method to calculate **E** and **H** at different times where **H** is calculated midway between two time steps that calculate **E**.

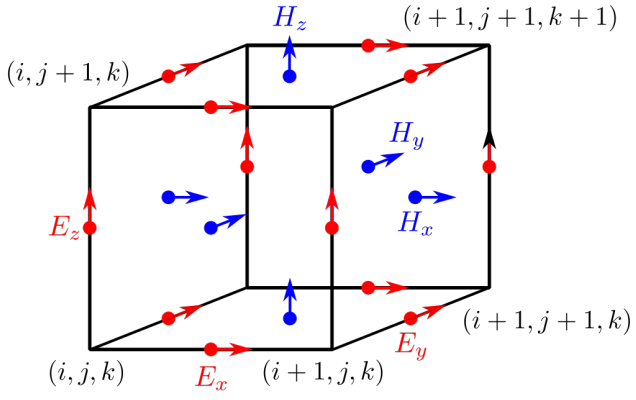

Figure A.2: A schmeatic of a Yee cell used for discretizing the time-dependent Maxwell's equations in the FDTD method. For a Yell cell at position (i,j,k), electric field components E_x, E_y and E_z are stored at positions $(i+1/2,j,k)$, $(i,j+1/2,k)$ and $(i,j,k+1/2)$, respectively. Similarly, magetic field compenents H_x, H_y and H_z are stored at $(i,j+1/2,k+1/2)$, $(i+1/2,j,k+1/2)$ and $(i+1/2,j+1/2,k)$, respectively.

For example, a Yee cell at position $\mathbf{r} = (i\Delta x, j\Delta y, k\Delta z)$ and at time step $t = n\Delta t$ has the x-component of the electric field E_x at position $(i + 1/2, j, k)$ is denoted by $E_x|^n_{i+1/2,j,k}$. Similarly, this Yee cell also contains other field components: $E_y|^n_{i,j+1/2,k}$, $E_z|^n_{i,j,k+1/2}$, $H_x|^{n+1/2}_{i,j+1/2,k+1/2}$, $H_y|^{n+1/2}_{i+1/2,j,k+1/2}$ and $H_z|^{n+1/2}_{i+1/2,j+1/2,k}$. The fields at a given time step can be calculated from those at the previous time step. To demonstrate how the fields are calculated, here, the update equations for E_x and H_z at time steps $t = (n + 1)\Delta t$ and $t = (n + 1/2)\Delta t$, respectively, are given as

$$\begin{aligned} E_x|^{n+1}_{i+\frac{1}{2},j,k} = E_x|^n_{i+\frac{1}{2},j,k} &- \frac{1}{\epsilon_0}\left(P_x|^{n+1}_{i+\frac{1}{2},j,k} - P_x|^n_{i+\frac{1}{2},j,k}\right) \\ &+ \frac{\Delta t}{\epsilon_0 \Delta y}\left(H_z|^{n+\frac{1}{2}}_{i+\frac{1}{2},j+\frac{1}{2},k} - H_z|^{n+\frac{1}{2}}_{i+\frac{1}{2},j-\frac{1}{2},k}\right) \\ &- \frac{\Delta t}{\epsilon_0 \Delta z}\left(H_y|^{n+\frac{1}{2}}_{i+\frac{1}{2},j,k+\frac{1}{2}} - H_y|^{n+\frac{1}{2}}_{i+\frac{1}{2},j,k-\frac{1}{2}}\right) \end{aligned} \tag{A.19}$$

$$\begin{aligned} H_z|^{n+\frac{1}{2}}_{i+\frac{1}{2},j+\frac{1}{2},k} = H_z|^{n-\frac{1}{2}}_{i+\frac{1}{2},j+\frac{1}{2},k} &\\ &+ \frac{\Delta t}{\mu_0 \Delta y}\left(E_x|^n_{i+\frac{1}{2},j+1,k} - E_x|^n_{i+\frac{1}{2},j,k}\right) \\ &- \frac{\Delta t}{\mu_0 \Delta x}\left(E_y|^n_{i+1,j+\frac{1}{2},k} - E_y|^n_{i,j+\frac{1}{2},k}\right) \end{aligned} \tag{A.20}$$

where the update equations for other field components can be obtained in the same manner. It is important to note here that the calculation for $\mathbf{P}$ in the above equation is not included within the FDTD framework alone. Hence, the FDTD must be used in combination with a specific material model to obtain $\mathbf{P}$. For example, $\mathbf{P}$ of a semi-classical emitter can be given by the Maxwell-Bloch equations.

A.4 DISCRETIZATION OF MAXWELL–BLOCH EQUATIONS

In order to simulate a quantum emitter in FDTD simulations, the Maxwell-Bloch equations must be converted into their discretized forms which directly couple with Eq. (A.19). Similar to the update equations in the FDTD method, the Maxwell-Bloch equations are updated in the leapfrog manner where $\mathbf{P}$ is updated at the same time step $t = n\Delta t$ as $\mathbf{E}$ while N_2 is updated at the same time step $t = (n+1/2)\Delta t$ as $\mathbf{H}$. Here, a time-dependent variable $A(t)$ is discretized as follows

	$t = n\Delta t$	$t = (n+1/2)\Delta t$
$A(t)$	A^n	$(A^{n+1} + A^n)/2$
$\partial A(t)/\partial t$	$(A^{n+1} - A^{n-1})/2\Delta t$	$(A^{n+1} - A^n)/\Delta t$
$\partial^2 A(t)/\partial t^2$	$(A^{n+1} - 2A^n + A^{n-1})/\Delta t^2$	-

Consequently, Eqs. (3.19) and (3.20) can be expressed as [178]

$$\frac{\mathbf{P}^{n+1} - 2\mathbf{P}^n + \mathbf{P}^{n-1}}{\Delta t^2} + 2\Gamma\frac{\mathbf{P}^{n+1} - \mathbf{P}^{n-1}}{2\Delta t} + (\Gamma^2 + \omega_{em}^2)\mathbf{P}^n = -\frac{2\omega_{em}}{\hbar}(N_2^n - N_1^n)\mathbf{E}^n \quad \text{(A.21)}$$

$$\begin{aligned}\frac{N_2^{n+1} - N_2^n}{\Delta t} = &-\gamma\frac{N_2^{n+1} + N_2^n}{2} \\ &+ \frac{1}{\hbar\omega_{em}}\left(\frac{\mathbf{P}^{n+1} - \mathbf{P}^n}{\Delta t} + \Gamma\frac{\mathbf{P}^{n+1} + \mathbf{P}^n}{2}\right)\cdot\frac{\mathbf{E}^{n+1} + \mathbf{E}^n}{2}\end{aligned} \quad \text{(A.22)}$$

N_2^{n+1} and $\mathbf{P}^{n+1}$ can then be obtained by the following update equations

$$\begin{aligned}\mathbf{P}^{n+1} = &\left[\frac{2 - (\omega_{em}^2 + \Gamma^2)\Delta t^2}{\Gamma\Delta t + 1}\right]\mathbf{P}^n + \left[\frac{\Gamma\Delta t - 1}{\Gamma\Delta t + 1}\right]\mathbf{P}^{n-1} \\ &+ \left[\frac{-2\omega_{em}N_d\Delta t^2/\hbar}{\Gamma\Delta t + 1}\right](2\frac{N_2^n}{N_d} - 1)\mathbf{E}^n\end{aligned} \quad \text{(A.23)}$$

$$N_2^{n+1} = \left[\frac{2 - \gamma\Delta t}{2 + \gamma\Delta t}\right]N_2^n + \frac{(2 + \Gamma\Delta t)\mathbf{P}^{n+1} + (-2 + \Gamma\Delta t)\mathbf{P}^n}{(2 + \gamma\Delta t)\hbar\omega_{em}}\cdot\frac{\mathbf{E}^{n+1} + \mathbf{E}^n}{2} \quad \text{(A.24)}$$

where $N_1^n + N_2^n = N_d$.